

Microfluidic cryofixation for time-correlated live-
imaging, cryo-fluorescence microscopy and electron
microscopy of *Caenorhabditis elegans*

Dissertation

for the award of the degree

“Doctor rerum naturalium”

of the Georg-August-Universität Göttingen

within the doctoral program

International Max Planck Research School

“Physics of Biological and Complex Systems”

of the Georg-August University School of Science (GAUSS)

submitted by

Giovanni Marco Nocera

from Naples, Italy

Göttingen, 2018

Thesis Committee

Thomas Burg, PhD
Max Planck Institute for Biophysical Chemistry, Göttingen
Biological Micro- and Nanotechnology

Prof. Dr. Sarah Köster
Georg-August-University, Göttingen
Institute for X-Ray Physics, Research Group Cellular Biophysics

Prof. Dr. Stefan Hell
Max Planck Institute for Biophysical Chemistry, Göttingen
Dept. of NanoBiophotonics

Members of the Examination Board

Referee: Thomas Burg, PhD
Max Planck Institute for Biophysical Chemistry, Göttingen
Group of Biological Micro- and Nanotechnology

2nd Referee: Prof. Dr. Sarah Köster
Georg-August-University, Göttingen
Institute for X-Ray Physics, Group of Cellular Biophysics

3rd referee: Prof. Dr. Stefan Hell
Max Planck Institute for Biophysical Chemistry, Göttingen
Department of NanoBiophotonics

Further members of the Examination Board

Dr. Henrik Bringmann
Max Planck Institute for Biophysical Chemistry, Göttingen
Group of Sleep and Waking

Prof. Dr. Silvio Rizzoli
University Medical Center, Göttingen
Department of Neuro- and Sensory Physiology

Prof. Dr. Jörg Enderlein
Georg-August-University, Göttingen
Group of Single Molecule Spectroscopy and Imaging for Biophysics and Complex Systems

Date of oral examination: October 15th, 2018

To Carmela, Giovanni and Maria

Table of Content

Abstract.....	1
Chapter 1 Introduction	2
1. Motivation.....	3
2. Light microscopy.....	3
2.1. Fluorescence microscopy at room temperature.....	3
2.2. Fluorescence microscopy at cryogenic temperature.....	4
3. Electron microscopy.....	7
4. Correlative microscopy.....	8
4.1. Chemical fixation of biological samples.....	9
4.2. Low temperature for the fixation of biological samples.....	9
4.3. Current technological limitations of cryofixation technology.....	15
5. Microfluidics for cryofixation.....	15
6. Structure of the thesis.....	18
Chapter 2 System design & Methods.....	20
1. Microfluidic device for cryofixation.....	21
2. Microfluidic chip fabrication procedure.....	27
3. Main heater fabrication procedure.....	30
3.1. Main heater with temperature sensors fabrication procedure.....	33
4. Heat transfer maximization.....	34
5. Assembly setup procedure.....	37
6. Electronic controls of the setup for <i>in situ</i> cryofixation.....	38
7. Rhodamine B temperature dependence.....	39
8. Rhodamine B bead measurements.....	39
9. Main heater calibration procedure.....	39
10. <i>C. elegans</i> sample preparation.....	40
11. Post-cryofixation sample transfer.....	40
12. Sample preparation and imaging for CLEM.....	41
13. Cryoimmersion light microscopy of cryofixed <i>C. elegans</i>	41

Chapter 3 Cryofixation of <i>Caenorhabditis elegans</i> within the field of view of a light microscope.....	46
1. <i>C. elegans</i> confinement in microfluidic channel	47
2. Temperature control of the microfluidic channel enables cryofixation of living samples	49
3. Integration of cryofixation with live imaging.....	51
4. Extent of ice formation analyzed by brightfield and DIC microscopy.....	52
Chapter 4 Cryofluorescence microscopy of <i>Caenorhabditis elegans</i> prepared by microfluidic cryofixation	57
1. Cryofixation preserves GCaMP fluorescence	59
2. Immersion microscopy at cryogenic temperature	64
2.1. <i>C. elegans</i> shape is preserved after sample transfer	64
2.2. Image quality in confocal cryoimmersion microscopy.....	67
3. STED effects on cryofixed GCaMP and gut granules	69
Chapter 5 Electron microscopy of microfluidic cryofixed samples.....	74
1. Cryofixed samples are not thawed during chip recovery	75
2. Time-resolved light-electron microscopy workflow	77
3. Quality of the cryopreservation.....	79
4. Preserving spatial orientation of <i>in situ</i> cryofixed samples	83
Chapter 6 Temperature measurement at the microscale	88
1. Design of resistive heater with built-in electronic temperature sensors	89
2. Visualization of temperature gradients within microfluidic channel volume.....	93
2.1. Effect of the solid matrix on the temperature coefficient of fluorescence of RhB-loaded melamine beads.....	96
Chapter 7 Conclusions and Outlook	97
1. Limitations of cryofixation in microfluidic systems.....	98
2. Limitations of cryoimmersion setup.....	101
Acknowledgements	105
Recurring Abbreviations.....	108
Bibliography	109
Appendix.....	114

Appendix I: Brief summary of experimental parameters	115
--	-----

Abstract

Light and electron microscopy are complementary methods to study biological systems at the cellular and sub-cellular scale. Light microscopy is compatible with live cells, allowing features of interest to be selectively marked with fluorescent molecules and followed in real time. Electron microscopy, in contrast, requires cells to be fixed. Cryofixation is a preferred method of fixation, since rapid freezing can preserve hydrated samples in a near-native state. However, state-of-the-art cryofixation systems require a transfer step that imposes a time lapse between the images acquired in light microscopy and the images acquired in electron microscopy. This transfer step prevents the correlation of light and electron cryo-microscopy of sub-second phenomena.

Microfluidics can eliminate the need of the transfer step. The cryofixation event is imaged without interruption from the top of a microfluidic channel that is heated while placed on top of a cryostage. When the heater is turned off, the small thermal mass of the microfluidic channel allows rapid cooling of the channel content.

In this thesis, microfluidic technology for cryofixation was shown for the first time to enable millisecond time-correlation between live imaging, cryofluorescence microscopy with immersion optics, and electron microscopy. An important benefit of fluorescence microscopy at cryogenic temperature resides in the arrest of photobleaching at very low temperature. However, the stability of fluorescent molecules at cryogenic temperature is still a field vastly unexplored. The microfluidic cryofixation system was used here to investigate the stability of the fluorescent calcium indicator GCaMP in live imaged roundworms (*Caenorhabditis elegans*). In another part of the thesis, the transfer of cryofixed samples was achieved for the first time with the intent to demonstrate the compatibility of the cryofixation system with correlative microscopy workflows. To acquire higher resolution images, the samples were transferred to a new immersion cryo-confocal microscopy setup developed by Faoro *et al.* [Faoro *et al.*, 2018]. Compared to the imaging on the cryofixation system, a 20-fold contrast gain was achieved. In the second workflow, the preservation quality of cryofixed samples was investigated via electron microscopy. Electron microscopy revealed an overall good preservation of the samples with minor ice damage within the nuclei. The results of this work constitute a foundation to enable new experimental paradigms for studying relationships between structure and function during rapid cellular processes such as cell signaling and membrane trafficking.

Chapter 1

Introduction

1. Motivation

The focus of this work was to correlate live-cell imaging, cryofluorescence, and electron microscopy of the same object with millisecond time resolution. Enabling the study of biological systems across length scales with high time resolution can contribute to understanding mechanisms that could not be seen otherwise. This is of fundamental importance, for instance, to connect behavioral phenomena to molecular mechanisms occurring within the cell environment. From a biophysical point of view, a cell is a self-replicating unit relentlessly using chemical energy to build up or break down molecules according to the continuous feedback from the outside environment and the inner milieu [Alberts *et al.*, 2002]. In a cell, events happen simultaneously. Each individual process might have repercussions at distances orders of magnitude larger and smaller than the cell itself. The complexity and variation in the relevant length scale of cellular processes often demands a phenomenon to be studied combining multiple techniques. Microscopy has the unique ability to extend the acquisition of data to the three spatial dimensions. The gathering of spatial information enables the possibility to follow events at different scales of observation. For instance, behavioral studies of *C. elegans* at the millimeter scale can be coupled with live imaging of neuron firing at the micrometer and sub-micrometer scale [Venkatachalam *et al.*, 2016].

2. Light microscopy

Depending on the experimental requirements and sample characteristics, the imaging modality can be tailored accordingly. Being a non-disruptive technique, light microscopy is usually the preferred choice for imaging the dynamics of living systems [Cole, 2014]. Live-cell imaging is a very versatile technique that allows biologists to conduct experiments, for instance, on the behavior of small organisms when exposed to different stimuli (e.g. temperature, chemicals, light). When coupled with fluorescence, live-cell imaging allows following in real time the dynamics of fluorescently marked molecules to better understand processes such as cell signaling and cell division [Ettinger and Wittmann, 2014].

2.1. Fluorescence microscopy at room temperature

Different strategies can be used to fluorescently label sites of interest in the cell environment. Immunocytochemistry consists of using antibodies to first selectively bind specific target molecules of the cell and later to tag a fluorescent marker to the site. Alternatively, it is possible

to genetically encode fluorescent proteins to be expressed in specific locations. Using these approaches, it is possible in principle to visualize every sub-cellular feature with nanometric resolution [Giepmans *et al.*, 2006]. The biggest limitation in reaching this level of resolution is the diffraction limit of visible light.

The smallest measurable distance between two point sources is referred as the Abbe's limit (Λ) (Eq. (1))

$$\Lambda = \frac{\lambda}{2n \sin(\alpha)} = \frac{\lambda}{2NA} \quad (1)$$

Where λ is the wavelength of light, n is the refractive index of the medium and α is the half opening angle of the microscope objective. The numerical aperture (NA) of the objective is given by $n \sin(\alpha)$.

In practice, this means that a conventional light microscope is not able to resolve smaller objects than half of the wavelength used by the microscope (~ 250 nm). To completely overcome this limitation, advanced light microscopy techniques were developed in the past 25 years [Schermelleh, Heintzmann and Leonhardt, 2010].

Different super-resolution microscopies exploit different mechanisms to break the diffraction limit. For instance, the image can be reconstructed exploiting the random alternation of bright and dark states (photoswitching) of the fluorescent molecules in the sample (photoactivated localization microscopy, PALM; stochastic optical reconstruction microscopy, STORM) [Betzig *et al.*, 2006]. A second common approach is to scan the sample with a laser to selectively excite only a few molecules at a time (stimulated emission depletion microscopy, STED) [Hell and Wichmann, 1994]. Another approach is to excite the sample using structured illumination. The images are then reconstructed using mathematical methods to extract the sub-diffraction information that the collected images contained [Gustafsson, 2000].

2.2. Fluorescence microscopy at cryogenic temperature

At room temperature, every time a fluorescent sample is excited, a portion of the fluorophores is irreversibly degraded by a photocatalytic reaction with singlet oxygen (photobleaching). Over

time, photobleaching gradually diminishes the amount of signal collected by the camera, eventually turning the sample completely dark [Ettinger and Wittmann, 2014]. Imaging fluorescent samples at cryogenic temperature can overcome this drawback. In a frozen matrix, oxygen cannot diffuse and fluorophores are protected from photobleaching [Kaufmann, Hagen and Grünewald, 2014]. An additional advantage of fluorescence cryo-microscopy is the possible increase in fluorescence intensity of the samples. Low temperature decreases the accessible vibrational states of the molecules. When non-radiative energy dissipation pathways become less accessible, fluorescent molecules tend to emit more photons, ultimately increasing their quantum yield [Berezin and Achilefu, 2010].

Several undesired photophysical characteristics of the fluorophores (e.g. absorption at undesired wavelengths, low turnover number, low quantum yield) limit the choice of the fluorescent dyes suitable for super-resolution microscopy [Schermelleh, Heintzmann and Leonhardt, 2010]. The dark states of fluorophores (T_1) are stabilized by low temperature, increasing the time constants of the decay to the ground state ($\tau_T = k_T^{-1}$) (**Figure 1**).

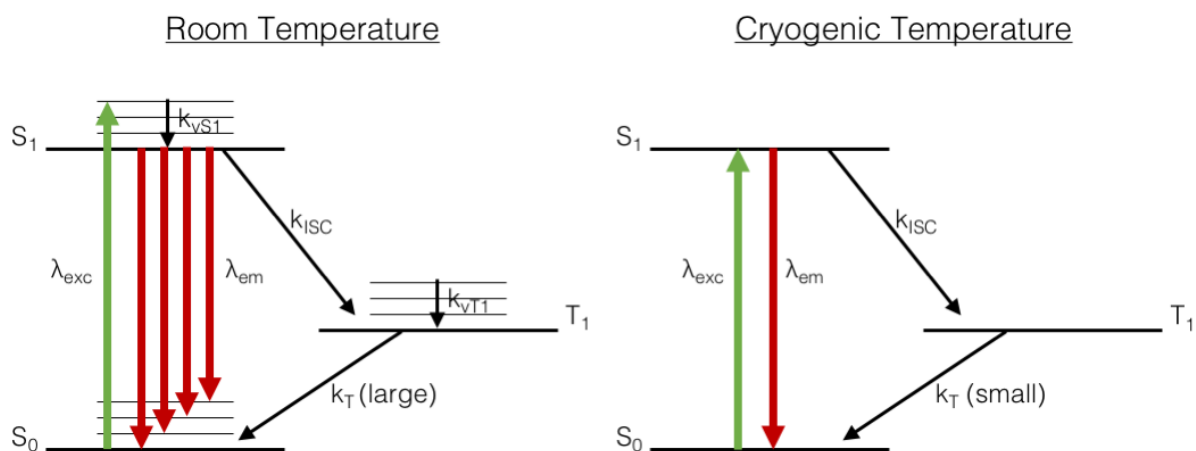


Figure 1 Schematic of the possible energy transitions across electronic states (S_0 , S_1 , T_1) and corresponding vibrational states (k_v) (Jablonski diagram). Radiative transitions are represented by red arrows, non-radiative transitions are represented by black arrows. The green arrows represent the excitation radiation. At cryogenic temperatures, vibrational levels are virtually absent and radiative transitions are the preferred way to dissipate energy. The sole non-radiative process still available at cryogenic temperatures involves the intersystem crossing to the triplet electronic state (k_{ISC}), also known as the dark state (T_1). The triplet state is usually more stable at cryogenic temperature than at room temperature (k_T larger at room temperature than at cryogenic temperature). Schematic modified from [Moerner and Orrit, 1999].

The effect of the decrease in temperature on the overall emission rate of the fluorophore, however, depends on the intersystem crossing rate (k_{ISC}) and the decay to the ground state (τ_T), where this dependence is modeled as in Eq. (2) [Moerner and Orrit, 1999]

$$\mathbf{Max\ emission} = \frac{\tau_f^{-1}}{2 + k_{ISC}\tau_T} \quad (2)$$

Here τ_f is the fluorescence lifetime of the fluorophore. Therefore, the effective gain in brightness is dye-specific and needs to be addressed case by case.

In epi-fluorescence microscopy, the amount of light collected by the camera sensor is proportional to the fourth power of the numerical aperture and inversely proportional to the square of the objective magnification (M) (Eq. (3)), that is,

$$\mathbf{Image\ brightness} \propto \frac{NA^4}{M^2} \quad (3)$$

High resolution microscopy is only achievable using high NA objectives. This is the reason to use immersion objective ($NA > 1$) instead of air objective ($NA < 1$).

The major challenge for immersion microscopy at cryogenic temperature consisted in where to distribute the temperature gradient from the cold sample to the room temperature microscope. In the past, different solutions were attempted. One approach was to remove the gradient from the sample-objective interface keeping the objective at cryogenic temperature with the sample [Le Gros *et al.*, 2009; Metzger *et al.*, 2016]. Another approach consisted in distributing the thermal gradient across the immersion oil [Nahmani *et al.*, 2017]. A third approach consisted in modifying an existing immersion objective to distribute the thermal gradient in the front lens mount [Faoro *et al.*, 2018]. In this third approach, the challenge was to find an immersion fluid that, once at cryogenic temperature, would match the refractive index of the room temperature immersion fluid. Faoro *et al.* used a partially fluorinated ether (HFE-7200) that at -140°C matched the refractive index of water. Using a modified water objective (63x, 1.15 NA), they were able to image plunge-frozen specimens (i.e. yeast, *E. coli*, human epithelial cells) below devitrification temperature at high resolution [Faoro *et al.*, 2018].

Previous studies, although limited by objectives with NA below unity, showed the applicability of super-resolution microscopy at cryogenic temperature [Chang *et al.*, 2014; Kaufmann *et al.*, 2014] and, in some case, also demonstrated a gain in resolution compared to

room temperature [Giske, 2007]. With the possibility to use immersion objectives in cryo-microscopy ($NA > 1$), the attainable resolution of fluorescence microscopy at cryogenic temperature is significantly increased [Kaufmann, Hagen and Grünewald, 2014]. The characterization in cryogenic microscopy (e.g. absorption-emission spectra at cryogenic temperature, decay rate to the ground state, quantum yield) of fluorescent dyes that at room temperature were found too dim or too prone to photodegradation, could lead to a substantial increase in the number of super-resolution-compatible fluorescent dyes. In contrast to photobleaching, dark states of fluorescent dyes are reversible. In fact, the ground state is repopulated over time when the excitation radiation is interrupted (recovery time). With a continuous exposure, the emission rate would be eventually limited by the decay rate from the dark state. With the implementation of recovery time cycles, a larger portion of molecules would be excited at each exposure, resulting in a stronger fluorescence signal. It is possible to imagine development of image acquisition routines, alternating exposure times with dark state recovery times to consistently collect the maximum fluorescence signal with an optimized trade off of acquisition time.

3. Electron microscopy

While light microscopy exploits photons to generate an image, electron microscopy (EM) uses electrons. A beam of accelerated electrons (~ 200 kV) is focused on the sample via electromagnetic lenses. With much shorter wavelengths for accelerated electrons than visible light, electron microscopes can achieve significantly higher resolutions than traditional light microscopes ($\sim 0.1 - 10$ nm). In order for the electrons to have a sufficiently high mean free path, the sample needs to be under high vacuum (10^{-4} Pa or higher). Various information can be collected depending on the different ways in which electrons interact with matter (**Figure 2**).

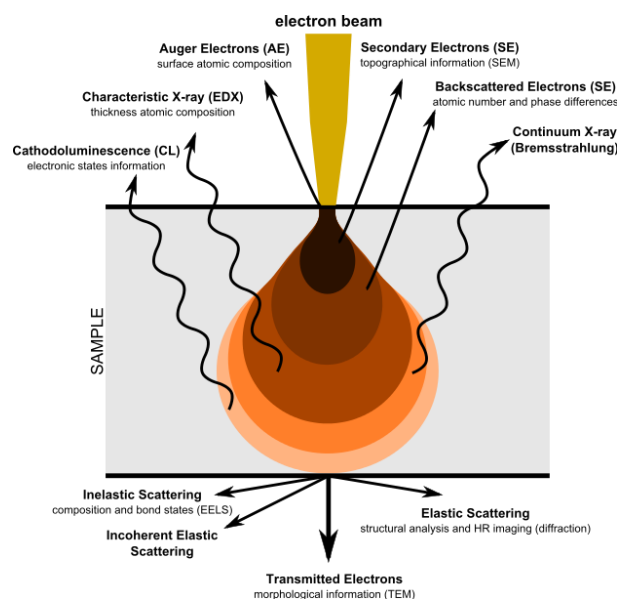


Figure 2 Schematic of the different ways electrons interact with matter and their exploitation for imaging and element composition detection. Figure distributed by Wikimedia Commons [Wikimedia Commons, 2013].

Typically, secondary electrons or transmitted electrons are used to generate images. The former provides topographical information, while the latter provides morphological information. Topographical information is mostly used to generate images in scanning electron microscopes (SEMs), whereas the morphological information is used in transmission electron microscopes (TEMs). TEM requires the sample to be thin because above ~ 80 nm of thickness, electrons in a biological sample are scattered and resolution is lost. Using secondary electrons, the sensitivity of SEM towards the sample thickness is less critical but resolution is inferior compared to TEM. To increase electron conduction on the samples in SEM, a metal coating (e.g. sputtered Pt) is usually required to avoid artefacts generated by charging of the sample surface [Ray F. Egerton, 2005].

4. Correlative microscopy

When at least two different microscopy techniques are combined for the same sample, the term correlative microscopy is used. Correlative light and electron microscopy (CLEM) exploits the qualities of both light and electron microscopy. This specific approach is implemented when the experiment requires the combination of dynamic information from the living system with the enhanced resolution power of EM [de Boer, Hoogenboom and Giepmans, 2015]. For instance, the conformational changes of endosomes were studied in TEM after the internalization of quantum dots into the cell environment was observed in live-cell imaging [Brown *et al.*, 2009]. The high vacuum necessary for electron microscopy, however, prevents the use of biological

samples in the form used in live-cell microscopy. Prior to electron microscopy imaging, elaborate sample preparation procedures are required [McDonald, 2009; Möbius, 2009].

Procedures for the preparation of biological samples for electron microscopy are sample specific. However, all of them have an initial fixation step. In general terms, fixation prevents the sample from changing over time. Throughout the history of the preservation of biological samples, different methods were developed. The next sections are an overview on the different fixation methods and their limitations.

4.1. Chemical fixation of biological samples

To fix the sample means to stabilize it in the desired state for imaging. Chemical fixation is the most established method to fix a sample. Chemical fixation is the preferred tool for histological studies because it allows the stabilization of large samples such as tissues or organs. Chemical fixation consists in using a solvent (e.g. methanol, ethanol, acetone) to carry a fixing agent into the sample that cross-links the proteins (e.g. formaldehyde, OsO₄). Staining agents such as heavy salts are usually added to a fixation mixture to highlight specific parts of the sample. Buffers are also added to a fixation mixture to maintain the sample at constant pH during the fixation process. To prevent shrinking or swelling of the sample, it is important to control the solute concentration of the mixture so that the biological membranes maintain the right osmotic pressure. A fixation protocol, with a particular composition of the fixation mixture, is specific to the kind of sample and to the parts of the sample that are of interest. For instance, ethanol would not be suitable in a protocol for the fixation of cell membranes because lipids would be dissolved rather than preserved. [Yeung and Huang, 2015]. In addition to requiring fine tailoring of the protocols, chemical fixation also tends to alter the sample in its innermost features (ultrastructure) creating artefacts [Kellenberger *et al.*, 1992]. The generation of artefacts by the fixation protocols has become more relevant with the use of electron microscopes on biological samples. Due to their higher resolution power, the resolution limit is set by the fixation procedures.

4.2. Low temperature for the fixation of biological samples

With decreasing temperature, water molecules tend to align their dipoles to form ordered clusters that eventually nucleate to form a growing crystal. From a thermodynamic point of view, ice formation can be modelled by the classical nucleation theory (CNT) [Debenedetti, 1996]. The

Gibbs free energy (ΔG) describes whether a thermodynamic process is spontaneous ($\Delta G < 0$) or it is not spontaneous ($\Delta G > 0$). According to the CNT, the ΔG of the system is the sum of two terms: the bulk free energy and the interface free energy. The bulk free energy represents the water molecules that are already ordered. They are in a low energy configuration and their contribution goes towards the formation of the ice crystal (negative term of the free energy). The interface free energy represents the water molecules at the border with the bulk. Forming a new interface always requires energy, this is why their contribution goes towards avoiding the formation of the ice crystal (positive term of the free energy). Because the bulk free energy scales with the volume of the forming ice crystal (r^3) and the interface free energy scales with the surface of the forming ice particle (r^2), the nucleation free energy has the shape depicted by the green line in **Figure 3** ($r^2 - r^3$) [Dubochet, 2007]. Before a thermodynamically favorable growth, the particle has to overcome an energy barrier (ΔG^*) and reach a critical size (r^*).

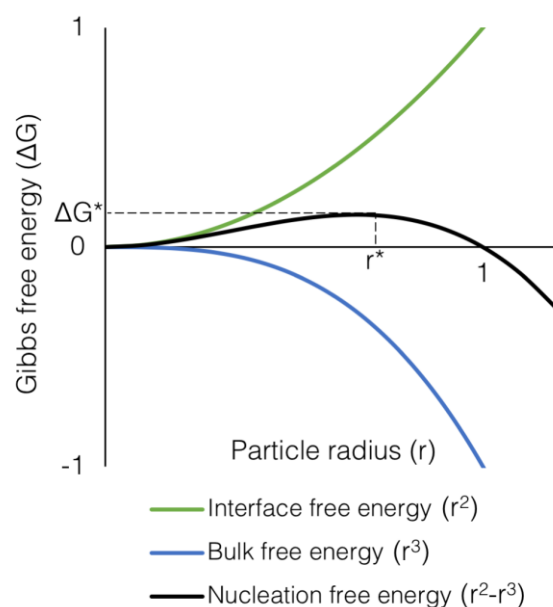


Figure 3 Classical nucleation theory. The Gibbs free energy (ΔG) as a function of the particle radius. The nucleation free energy (black curve) is the sum of two terms: the interface free energy (green curve), always positive and scales up with the surface of the particle, and the bulk free energy (blue curve), always negative and scales up with the volume of the particle. Before the particle growth becomes thermodynamically favorable ($\Delta G < 0$), the particle has to overcome an energy barrier (ΔG^*) and reach a critical size (r^*) [Debenedetti, 1996].

The necessity to overcome an energy barrier before freezing makes it possible to find liquid water far below its freezing temperature (supercooled water). In fact, liquid water has been observed down to -40°C [Mishima and Stanley, 1998]. When nucleation is exclusively promoted by molecules in the liquid state the process is referred as homogeneous nucleation. The presence of external nucleation points (e.g. particles, impurities) can lower the freezing energy barrier and

make ice nucleation much easier. This is named heterogeneous nucleation. The cell environment appears to be very scarce of nucleation points. However, ice nucleation is often observed in the surrounding medium. Once nucleation starts, water molecules are subtracted from the cell environment, causing both dehydration of the cell and agglomeration of the biological material (e.g. macromolecules, solutes) [Dubochet, 2007; Hall, Hartwig and Nguyen, 2012]. This process in most cases causes the death of the cell because biomolecules often denature upon aggregation. However, in nature there are species that have found ways to survive temperatures below freezing. For instance, nematodes from the Pleistocene were found in viable condition once thawed from the permafrost [Shatilovich *et al.*, 2018], or tardigrades were observed surviving at -80°C for 24h. In the case of the tardigrade, a micro-animal that at full size reaches 500 µm in length, it was demonstrated that the tolerance to dehydration was due to the ability to express large quantities of so called intrinsically disordered proteins (IDP) that reach a glassy state at low temperature. By replacing all the water from the organism, IDP are believed to embed and protect cells and macromolecules, allowing the animal to survive dehydration for long periods of time [Boothby *et al.*, 2017].

The use of chemicals to lower the risk of ice damage is an established strategy to preserve biological samples. These molecules are called cryoprotectants and they usually consist of sugars, alcohols or salts. They work by lowering the freezing point of water and, if used in high concentrations, they can eventually replace most of the water present in the sample [Steinbrecht and Zierold, 1987]. Cryoprotectants can be divided in two major classes: permeant and non-permeant. Permeant cryoprotectants (e.g. DMSO, glycerol) are able to diffuse through cell membranes, ensuring a more uniform preservation in all parts of the sample. Non-permeant cryoprotectants (e.g. trehalose, NaCl) are usually less toxic to the samples, but also less effective [Fuller, 2004]. Cryoprotectants are associated to a certain level of toxicity proportional to their concentration. This is why their use tends to be minimized when possible [Best, 2015].

A separate category of cryoprotectants that in the past years appeared to have promising applications are anti-freeze proteins (AFPs) and their synthetic alternatives (e.g. derivatives of the polyvinyl alcohols, cyclohexanediols) [Fuller, 2004]. AFPs work by a different mechanism than classical cryoprotectants. In fact, they do not change the freezing point of water. Instead, they arrest the growth of newly formed ice crystals by binding to their surface with high affinity [Yeh and Feeney, 1996; Celik *et al.*, 2013]. Working via a different principle than the sole colligative property, their efficacy is not only proportional to their concentration. For this reason, the

effective concentration of cryoprotectant could be reduced to lower the risk of toxicity and osmotic stress.

Rapid freezing or cryofixation, is the temperature-based method most broadly accepted by the scientific community to preserve biological samples in their near-native state [Dubochet, 2007]. Cryofixation consists in the rapid cooling of a sample below a certain temperature. By rapidly decreasing the temperature, water molecules do not have the time to arrange and organize in a crystalline structure. For good preservation, high cooling rates between 10^4 and 10^6 °C·s⁻¹ are required to prevent crystallization. Combined with the high cooling rate, a final temperature below the glass transition temperature of water ($T_g(\text{water}) = -137^\circ\text{C}$) is necessary to avoid the rearrangement of water molecules over longer times. In fact, below T_g water molecules do not have the necessary kinetic energy to rearrange and cryofixed samples can be stored indefinitely [Steinbrecht and Zierold, 1987]. When water is cooled in this manner, it reaches an amorphous or vitrified state.

A rigorous definition of the vitrified state of water is still a matter of debate in the scientific community [Mishima and Stanley, 1998; Dubochet, 2007; Limmer and Chandler, 2014]. Within the context of this work, it will be simply defined as a solidified state in which the elements forming the sample have preserved the spatial organization of the liquid state prior to freezing.

Depending on sample characteristics and experimental requirements, various methods were developed over the decades to rapidly freeze hydrated samples. For the cryopreservation of biological tissues and sections of organs, one of the first developed methods was *slam freezing* [van Harreveld and Crowell, 1964]. In slam freezing, samples are held at the end of a piston and rapidly projected, using gravity or a loaded spring, against the polished surface of a highly conductive metal block (e.g. copper, silver) that is in contact with a cryogenic fluid (i.e. liquid nitrogen, liquid helium). Using this method, samples were successfully preserved to a depth of 10 – 15 µm. However, a gradient in the preservation quality was observed moving farther from the metal surface. From 0 to 5 µm in depth, no ice damage was visible in the sample. Between 5 and 10 µm, the condensation of heterochromatin in the nuclei started to be visible. From 10 µm, ice damage was visible also in the cytoplasm. Mitochondria showed no sign of ice damage until 15 µm of depth [Allison, Daw and Rorvik, 1987]. Incremental improvements of the slam freezing technology were observed over the years. Oxidation of the polished metal surface was degrading the heat transfer and therefore, decreasing the sample preservation quality after each cycle. The issue was solved by plating the copper with a thin gold layer that would allow multiple cycles

before the need of renewal. Freezing quality was also deteriorated by the presence of frost on the metal surface. Developing of dry environments around the cold surface was part of the progressive improvements of slam freezing. Being close to the cold surface, samples often reached freezing temperatures before the contact with the polished surface. Implementation of diaphragms and removable windows prevented undesired slow freezing of the samples [Dykstra, 1992].

To increase the preservation depth, systems allowing the simultaneous rapid cooling of both sides of the sample were developed (*jet freezing*) [Müller, Meister and Moor, 1980]. The tissue or slice was placed in between two polished metal foils and held suspended between two nozzles pointing at each metal foil. From the nozzles, a jet of liquid propane was used to cryofix the sample. After cryofixation, the piston was submerged in liquid nitrogen to remove the foils and recover the sample.

To study the structure of vesicles or single cells, *spray freezing* was developed. The sample in the form of a water suspension was nebulized in drops of about 30 μm in diameter. Drops were frozen when the stream was generated into liquid nitrogen-cooled liquid propane (m. p. -188°C). The sample was then collected from the propane and desiccated on a cryogenic stage. Dry drops were then mixed with a viscous hydrocarbon at $\sim -100^\circ\text{C}$ (e.g. ethylbenzene, butylbenzene) to produce a paste that was solidified in liquid nitrogen. The sample was then fractured in liquid nitrogen, Pt/C was evaporated on the exposed surface of the sample to make a replica, and the replica was imaged in electron microscopy. Due to the multiple steps involved in the sample preparation and the high susceptibility to the operational parameters, this method is prone to generate artifacts. For this reason it should only be used if other, more reliable methods cannot be utilized [Van Venetië *et al.*, 1980; Dykstra, 1992].

Being inexpensive and adaptable to different kinds of samples (e.g. cell suspensions, solutions of molecules, thin slices of tissues), *plunge freezing* is still nowadays among the most common methods to cryofix samples despite being introduced about 40 years ago [Dubochet and McDowall, 1981; Dobro *et al.*, 2010; Renaud *et al.*, 2018]. Plunge freezing consists in the rapid immersion ($\sim 10 \text{ m}\cdot\text{s}^{-1}$) of the sample in a cryogenic fluid. To achieve a good preservation quality, a fast dissipation of the thermal content of the sample is as usual a critical parameter that needs to be maximized. This can be done by optimizing the shape and material of the sample holder and by an appropriate choice of the cryogenic fluid. For instance, liquid nitrogen generates a substantial boundary layer of gas around the sample holder that ultimately decreases the cooling rate of the sample. This is due to the low boiling point of liquid nitrogen (b. p. -196°C). Better results were reported using fluids with higher boiling points such as liquid

ethane (b. p. -89°C) and liquid propane (b. p. -42°C) cooled by liquid nitrogen [Dubochet and McDowall, 1981; Al-Amoudi *et al.*, 2004]. The absence of the boiling liquid around the sample increased the heat dissipation therefore improving the fixation quality.

The convenience of plunge freezing is particularly evident for the study of macromolecular objects in transmission electron microscopy at cryogenic temperature [Dobro *et al.*, 2010; Renaud *et al.*, 2018]. In fact, thin, suspended water layers in the tens of nanometers can be easily formed using commercial TEM grids as a support. A suspension of sample molecules in water is usually applied on the TEM grid and the excess water is removed using absorbing paper (blotting). The remaining liquid stays as a uniform film across the holes of the grid. Then, the grid is plunged in a liquid nitrogen-cooled cryogenic fluid to vitrify the sample [Passmore and Russo, 2016].

Despite its versatility, plunge freezing suffers from sample thickness limitations (few micrometers). *High pressure freezing* (HPF) was developed to overcome this limitation. High pressure (~ 2000 bar) is applied at the moment of freezing to prevent ice crystal growth and enable the cryofixation of samples up to $200\ \mu\text{m}$ in thickness [Steinbrecht and Zierold, 1987].

For the imaging of cryofixed samples by cryo-electron microscopy, various approaches are possible. Thin samples (plunge-frozen blotted grids) can directly be moved into a cryo-TEM for imaging after cryofixation. For bulk samples (e.g. tissues, micro-organisms), thin slices (~ 50 nm) can be cut and transferred onto TEM grids for imaging in cryo-TEM (CEMOVIS) [Al-Amoudi *et al.*, 2004]. Alternatively, the possibility of milling the samples at cryogenic temperature using a focused ion beam (cryo-FIB) and imaging it in cryo-SEM has been reported [Schertel *et al.*, 2013].

Freeze substitution is an established procedure that has the aim of warming up the sample to room temperature while preserving its cryofixed conformation [McDonald, 2009]. To increase contrast in electron microscopy, it is common to couple freeze substitution with sample staining (e.g. heavy metal salts, osmium tetroxide). Following freeze substitution, the sample can be embedded in an epoxy resin for mechanical stability, cut in 50 nm thin slices and imaged in TEM [McDonald, 2009]. For tomographic reconstructions, another approach might be, for example, to replace the sectioning with FIB milling and following SEM imaging [Kizilyaprak *et al.*, 2014].

4.3. Current technological limitations of cryofixation technology

Whenever cryofixation is part of a correlative microscopy workflow, a transfer step is required. This transfer step has the risk of perturbing the sample and imposes a time lapse between the last observation and the fixed state that would be imaged later. This limitation is intrinsic to all currently available cryofixation technologies. In case of manual handling of the sample, the maximum time resolution is operator-dependent but it falls in the range of the tens of seconds. In case of HPF, automatized transfer systems reduced the time lapse between live imaging and cryofixation to around five seconds [Verkade, 2008; McDonald, 2009]. A modern, state of the art HPF instrument can reach a time resolution of one second from the last observation in light microscopy (EM ICE High Pressure Freezer, Leica Microsystems). As a further time resolution improvement, a commercially available HPF was modified to trigger biological events (i.e. membrane trafficking) using blue light and imaged in electron microscopy with millisecond time resolution. The sample was cryofixed for imaging in electron microscopy tens of milliseconds after the event was triggered. [Watanabe, Liu, *et al.*, 2013; Watanabe, Rost, *et al.*, 2013]. Watanabe *et al.*, however, did not achieve imaging of the event during cryofixation nor did they provide direct correlation to light microscopy for a given sample. Correlative light and electron microscopy studies of phenomena faster than the transfer step are currently impeded.

5. Microfluidics for cryofixation

A fundamental limitation for all cryofixation methods is the sample size. To prevent water molecules from organizing into crystalline structures, heat needs to be dissipated fast enough from the sample. Regardless of the applied cooling rate at the surface, however, heat dissipation is ultimately limited by the thermal conductivity of the bulk. Exact numbers on the size limit for the vitrification of pure water are difficult to achieve. Results can be strongly affected by the experimental conditions (e.g. thermal conductivity at the interface, effective surface area for the heat transfer). This is the reason for the wide range of values that can be found in literature. A biological sample, however, is not made out of pure water. Empirically it was found that the maximum size of a biological sample that can be vitrified using HPF is around 200 micrometers. At atmospheric pressure ice damage of the most fragile parts (i.e. nuclei) starts to be visible for samples thicker than 5 μm [Allison, Daw and Rorvik, 1987]. Achievable results vary with the concentration in cryoprotectants and the effective amount of water that is present in the biological sample. In fact, the water concentration within the cell environment can vary substantially. Cells have hydrophilic components rich in water (e.g. cytoplasm, outer medium)

and hydrophobic components virtually water-free (e.g. inner part of phospholipid bilayers). On a smaller scale, the existence of so called hydrophobic pockets within hydrophilic objects like proteins are also known [Hillyer and Gibb, 2016; Xi *et al.*, 2017]. Within the same biological sample, differences in the relative water/solute content within the cell environment can lead to variations in cryofixation quality throughout the sample.

Microfluidic devices are readily fabricated on the order of tens of micrometers [Whitesides, 2006]. Prior to this work, microfluidics was proposed by our laboratory as a viable tool for cryofixation, opening possibilities for correlative microscopy applications [Mejia *et al.*, 2014]. In the microfluidic device for cryofixation, the sample is confined in a microfluidic channel that is placed on top of a resistive heater. The device is placed on an upright microscope and the sample is visually accessible throughout the experiment, before, during and after cryofixation. The resistive heater controls the temperature of the sample which is thermally connected to a heat sink submerged in a liquid nitrogen bath. While the heater is on, the sample is kept at suitable temperature for live imaging. After turning off the heater, the sample is cryofixed in place within milliseconds. With *in situ* cryofixation, the time resolution in correlative microscopy experiments is only limited by the actual freezing time of the sample, which is on the order of the milliseconds (**Figure 4**).

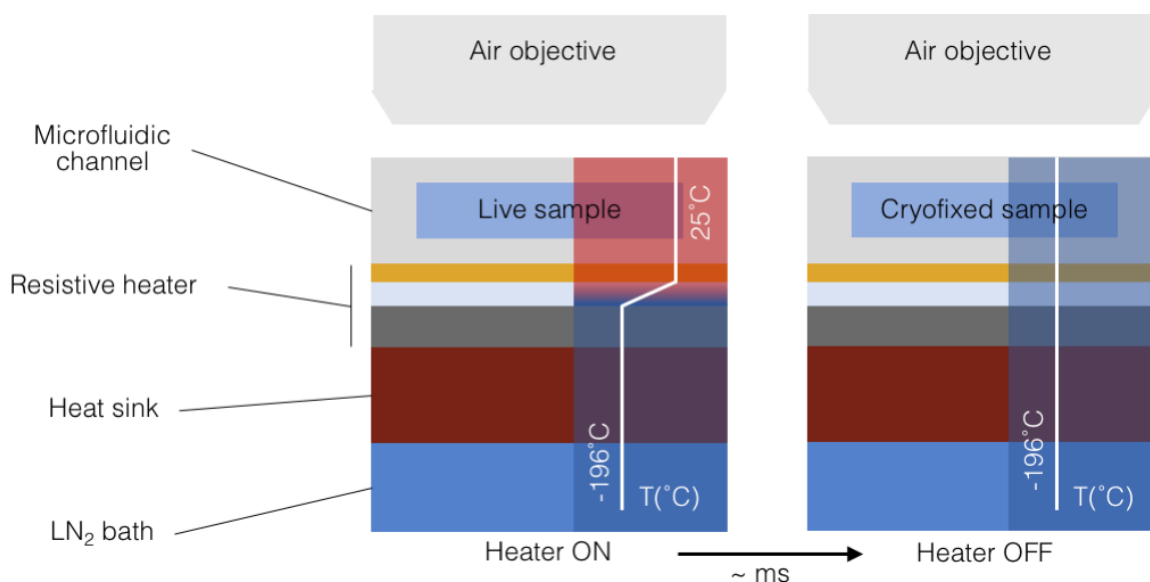


Figure 4 Schematic of the working principle of the microfluidic device for cryofixation. The device is located on an upright microscope and the sample is visually accessible from the top side of the device. The sample is confined in the microfluidic channel and placed on top of a resistive heater. The heater is in contact with a heat sink submerged in a liquid nitrogen bath. The temperature of the sample is controlled by the resistive heater. The sample is cryofixed within milliseconds after turning off the heater. Schematic modified from [Mejia *et al.*, 2014].

Mejia *et al.* set the groundwork for further technological developments that were part of this work. In the work from 2014, the possibility to achieve rapid freezing of a water sample in a microfluidic channel was demonstrated [Mejia *et al.*, 2014]. It was shown that fluorescent beads flowing in a channel could be frozen *in situ* and the flow was arrested within 100 ms from the triggering of the cryofixation. In that design, the heat sink was cooled via a continuous flow of liquid nitrogen through the heat sink. The freezing quality was assessed by comparing the channel's appearance upon fast freezing and slow freezing. Cooling rates were estimated via computer simulations, varying parameters such as channel height and distance from the cold surface.

Without an established method to calibrate the temperature within the microchannel, the system lacked the precision temperature control required for life science experiments. In fact, although yeast cells were cryofixed in the channel, the living state of the cells was never assessed. Secondly, the vigorous boiling of liquid nitrogen transmitted vibrations to the stage, degrading its mechanical stability and likely contributing to the low yield of successful experiments.

With the accomplishments of Mejia *et al.* as a starting point, the milestones for this work were **(Figure 5)**:

1. Making the microfluidic device for cryofixation a suitable tool for living biological samples.
2. Tailoring the microfluidic components of the device for *Caenorhabditis elegans* (*C. elegans*), the model system of choice.
3. Demonstration of compatibility of the cryofixation device with
 - a. Established correlative light and electron microscopy workflows.
 - b. Immersion light cryo-microscopy.

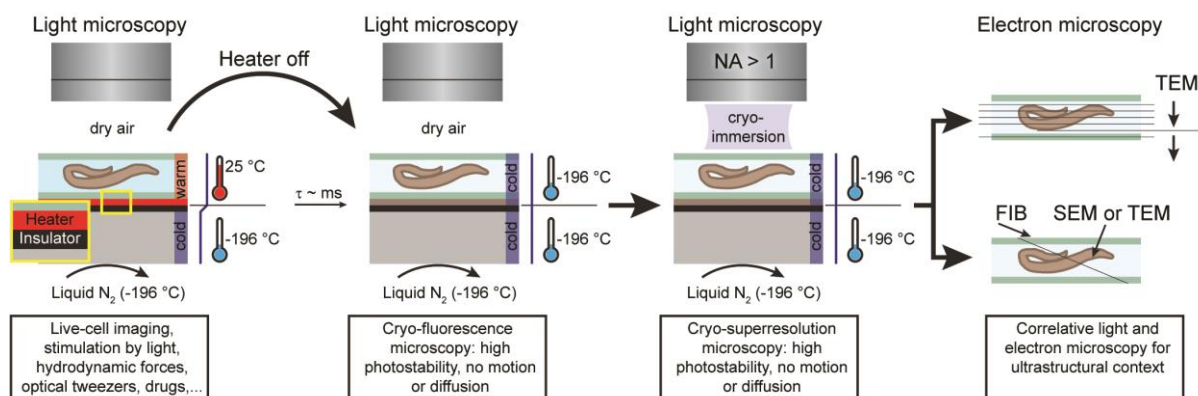


Figure 5 Overview of the potential workflow with the microfluidic system for cryofixation. During live imaging, the sample is cryofixed within milliseconds. The cryofixed sample is kept at cryogenic temperature and then transferred to immersion cryo-microscopy. Later, the sample is processed for imaging in electron microscopy. Schematic courtesy of Thomas Burg, PhD.

6. Structure of the thesis

This thesis is divided into seven chapters and an appendix. In the Introduction (Chapter 1) the motivations of the work, the technological challenges and the state of the art were exposed.

In Chapter 2, the system design and the microfabrication methods are described.

Chapters 3 through 6 report and discuss the results.

Chapter 3 is focused on the cryofixation event. Specimens are live imaged in the microfluidic channel and cryofixation is performed within the field of view of the microscope. Video acquisitions in brightfield microscopy and enhanced contrast microscopy (DIC microscopy) are analyzed to investigate whether it is possible to detect ice formation in the microfluidic channel upon cryofixation.

In Chapter 4, fluorescence intensity is measured to investigate the influence of the rapid temperature decrease on the GCaMP intensity. This chapter also demonstrates the compatibility of samples cryofixed in the microfluidic channel with the immersion cryo-microscopy setup.

In Chapter 5 the quality of the cryofixation via transmission electron microscopy is assessed. Therefore, the use of the cryofixation system with established correlative light and electron microscopy workflows is demonstrated.

In Chapter 6 the experiments on temperature measurement at the microscale that did not produce applicable outcomes are collected. In particular, it is reported up to which extent the fabrication of electrical temperature sensors embedded in the resistive heater outline was possible. As well, the limits for the use of rhodamine B as a temperature probe are reported.

Chapter 7 is dedicated to the conclusions and the discussion of the fundamental and technological limitations of the technology developed and used throughout the work.

In Appendix I, a summary table for the parameters used in each experiment was reported.

Chapter 2

System design & Methods

1. Microfluidic device for cryofixation

The core components of the microfluidic device for cryofixation are the microfluidic chip and the main heater.

The microfluidic chip is where the sample resides and it is formed by an injector chip and a polydimethylsiloxane (PDMS) microfluidic channel. The sample enters the microfluidic device from the inlets, flows through the bypass channels and reaches the PDMS microfluidic channel via etched through holes in the injector chip. A view window in the injector chip allows observation of the sample throughout the experiment (**Figure 6**).

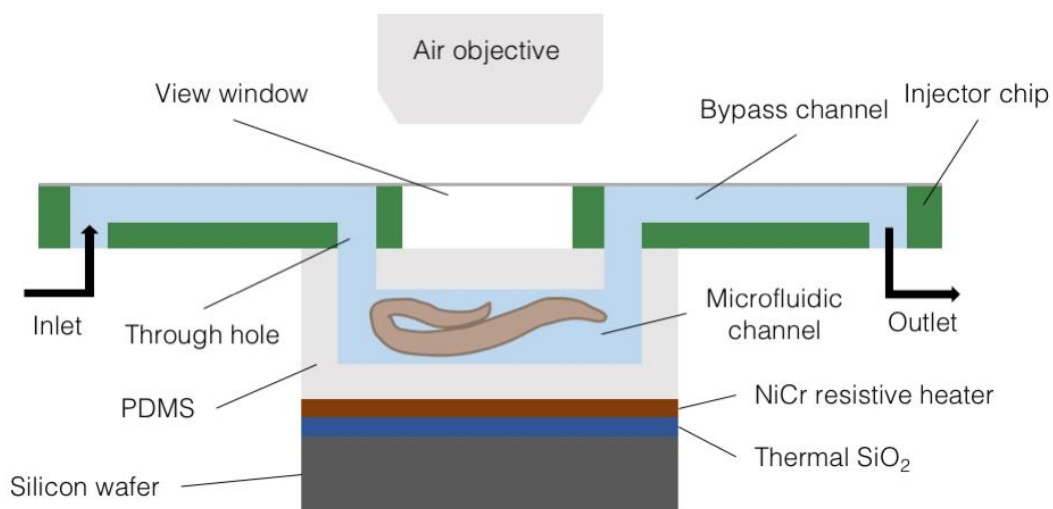


Figure 6 Schematic of the core components of the microfluidic device for cryofixation. The microfluidic device is formed by an injector chip which is bonded to a PDMS microfluidic channel. From the macroscale tubing, the sample flows into the bypass channels of the injector chip and reaches the microfluidic channel via through holes. The microfluidic chip is in contact with the main heater. The main heater is formed by a silicon substrate with a thermally grown SiO_2 layer on which metal traces are patterned to form the heater. In particular, NiCr is used for the resistive heater strip and gold is used for electrical wiring (see **Figure 8**) (schematic not to scale).

The injector chip is a silicon device, developed within our group over the years. Its function is to bring the sample from the macroscale fluidics to the microfluidic channel. Connecting the macroscale tubing to the injector chip, the sample first flows into the U-shaped bypass channels and eventually enters the PDMS microfluidic channel. The bypass channels allow rapid exchange of the sample without interfering with the microfluidic channel content. This feature can be exploited for operations such as buffer exchanges, delivery of drugs or triggering of events via chemical stimuli. To enable chemical fixation of cryofixed samples, its dimensions are compatible with commonly used vials for freeze substitutions (**Figure 7**).

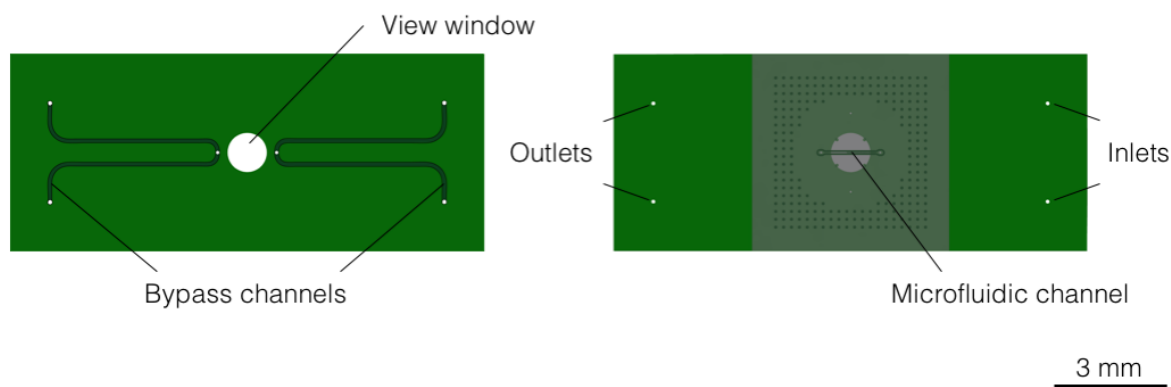


Figure 7 Top and bottom sides of the microfluidic device for cryofixation. (Left) The top side of the injector chip has U-shaped bypass channels that bring the sample from the macroscale tubing to the microfluidic channel. The shape of the bypasses allows exchange of the sample media without perturbing the content of the microfluidic channel. For instance, chemicals can be delivered to trigger events before cryofixation. Modified from [Fuest and Nocera et al., 2018].

During the experiment, the temperature within the microfluidic channel is controlled by the main heater. The main heater is formed by a silicon substrate with a layer of thermally grown SiO_2 (cf. **Figure 6**) on top of which a NiCr heater strip and gold traces for electrical connection were patterned (**Figure 8**). The thermally grown SiO_2 layer is used as a thermal insulator to spread the thermal gradient that exists between the heated sample and the cold silicon substrate.

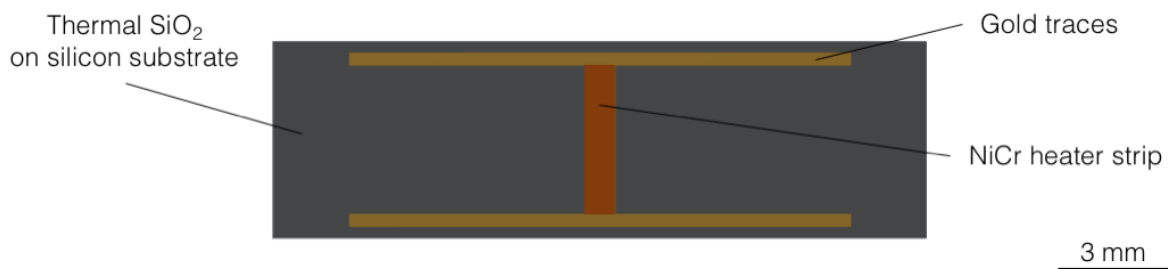


Figure 8 Outline of the main heater. On the silicon substrate, NiCr and gold are deposited to form the main heater. The high resistivity of NiCr is exploited to generate the heat that during the experiment keeps the sample at a suitable temperature. Gold is used to electrically connect the heater strip to an external power supply.

The microfluidic chip used in the device for cryofixation is designed to enable rapid cooling of the sample. To this end, a polydimethylsiloxane (PDMS) channel was fabricated within a thin foil of low thermal mass. To maximize the rate of heat dissipation the channel bottom separating the sample from the main heater was made only about $17 \mu\text{m}$ thin (**Figure 9**). Thinner PDMS foils turned out to be too fragile and did not survive the peeling step during the fabrication procedure of the fluidic chips (cf. Chapter 2, 2. Microfluidic chip fabrication procedure).

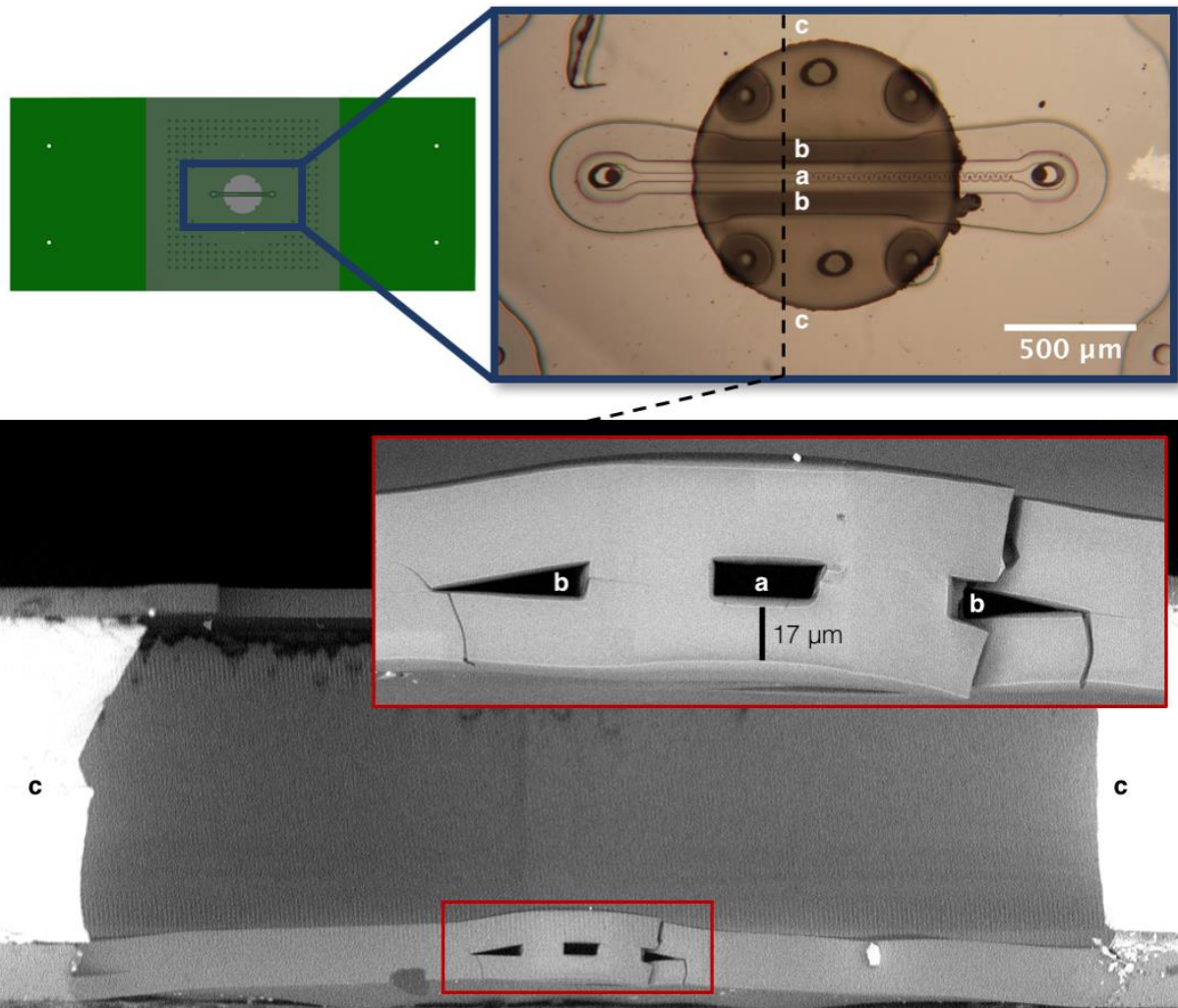


Figure 9 Cross-section of the microfluidic chip in scanning electron microscopy. The dashed line represents where the breaking of the chip was done. The inset shows the part of the channel separating the sample from the main heater surface. Across images, same parts of the chip are labeled with the same letters (a-c).

The microfluidic device for cryofixation used during this thesis work consisted of a self-contained system suitable for use with any commercial upright microscope with epi-illumination (Figure 10).

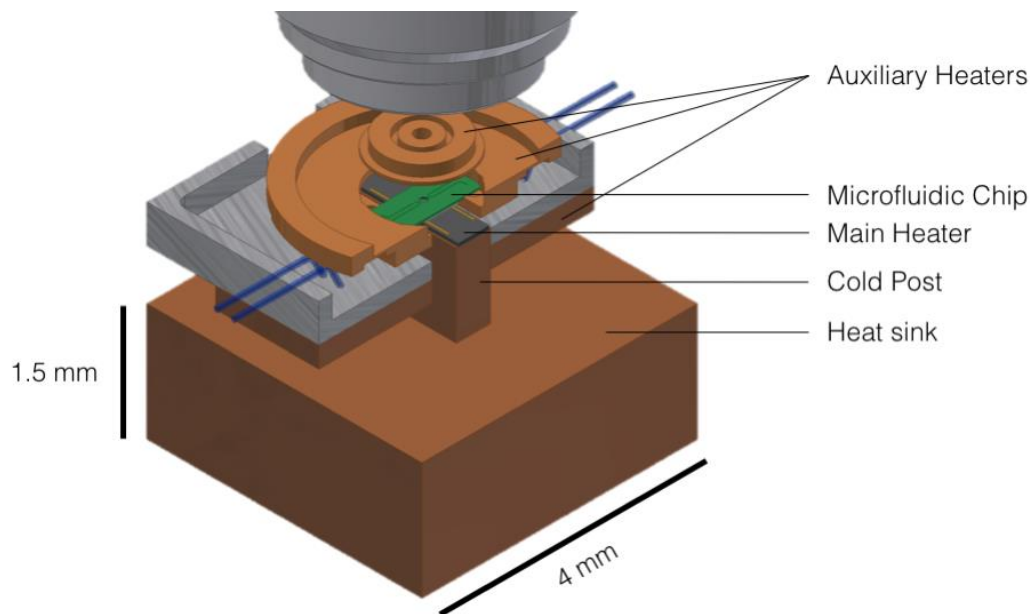


Figure 10 Components of the microfluidic device for cryofixation. The microfluidic chip is enclosed in a copper holder that provides connections to the macroscale tubing and auxiliary heaters to prevent the undesired freezing of the sample outside the microfluidic channel. The sample is observed from the top side. During assembly, the microfluidic device is aligned and put in contact with the main heater. During an experiment, the heat sink is submerged in a liquid nitrogen bath and the main heater maintains the sample at a suitable temperature for live imaging. Cryofixation is performed by turning off the main heater with uninterrupted observation of the sample. Modified from [Fuest and Nocera et al., 2018].

During the experiment, the heat sink is partially submerged in liquid nitrogen to allow rapid dissipation of the heat generated by the main heater that is attached to the cold post. The main heater maintains the sample at the suited temperature up until cryofixation, which is carried out when the main heater is turned off. The microfluidic chip, placed over the main heater, is contained in a copper housing that has the double purpose of connecting the chip to the macroscale fluidics and preventing undesired freezing of the sample. The copper holder is provided with auxiliary heaters that work independently from the main heater and keep the rest of the device at room temperature before, during, and after cryofixation of the channel content. The holder provides a reversible connection between the microfluidic device and the macroscale tubing for easy transfer of the sample after cryofixation. The microfluidic device is held in place by one single screw ring pressing against the ring heater. The screw ring is the only item to remove in order to access the microfluidic device after cryofixation of the sample. The ring heater and microfluidic device include view windows that allow continuous observation of the sample in the light microscope before, during and after cryofixation (**Figure 10**).

The microfluidic device for cryofixation can be modeled as shown in **Figure 11**.

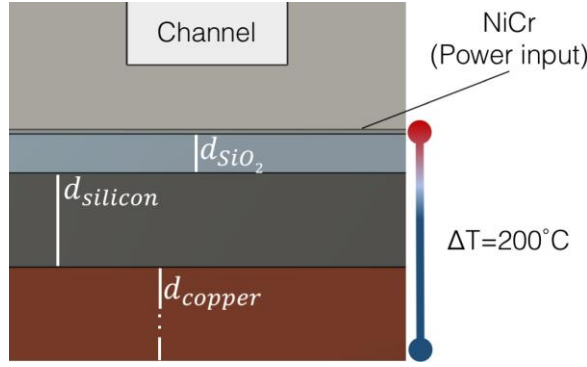


Figure 11 Schematic of the thermal gradient across the different layers of the microfluidic device for cryofixation. Cross-section view across the shorter side of the microfluidic channel (yz -plane, not to scale).

The layer thickness, and thermal conductivity of the materials are listed in **Table 1**.

Table 1 Numerical values for each variable used to calculate the heat resistances of every layer of the microfluidic device for cryofixation (R_i): thickness of the layer (d_i), thermal conductivity of the material at 25°C (k_i) [Rumble, 2018].

	d_i (μm)	k_i ($\text{W}\cdot\text{m}^{-1}\cdot\text{K}^{-1}$)
SiO₂	2.50	1.5
Silicon	300	150
Copper post	2000	385

Using Fourier's law

$$\dot{q} = -\frac{T_1 - T_{n+1}}{\sum_{i=1}^n \frac{d_i}{k_i \cdot A_i}} = -\frac{\Delta T}{\sum_{i=1}^n R_i} \quad (4)$$

A power of about 40 W was theoretically estimated to maintain a temperature gradient of 200°C across the device. Experimentally, the power needed to run experiments was ~ 65 W. The discrepancy might be due to the side cooling of the channel via the PDMS layer bridging the cold surfaces of the silicon dioxide.

The PDMS layer of the microfluidic chip has a square shape that measures 5 mm per side (cf. **Figure 7**). Extending beyond the surface of the NiCr heater strip, the PDMS also joins the rest of the fluidic chip to the unheated surface of the silicon dioxide. The heat dissipation through

the PDMS layer outside the NiCr heater is the main reason auxiliary heaters are required to maintain the peripheral fluidics above the freezing point of water.

Using Eq. (4), it was possible to estimate the heat flow across the overall PDMS area outside the NiCr heater surface. This value was found to be about 6.5 W.

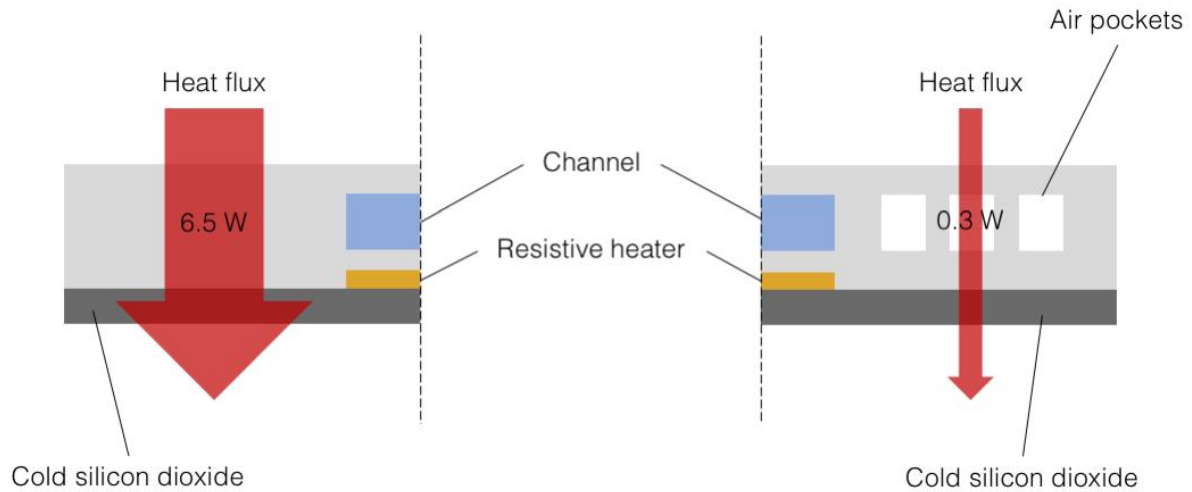


Figure 12 Power required to maintain the fluidic chip at 25°C. Adding air pockets in the PDMS around the microfluidic channel, a 20-fold decrease in heating power is required.

To minimize the heat dissipation through the PDMS, the bulk of the material was replaced with air pockets. With the implementation of air pockets, the contact between the fluidic chip and the cold silicon dioxide was limited by the effective area of the PDMS structures that prevent the collapse of the air pockets. Adopting this solution, the power required to maintain fluidic chip at 25°C was found to be 0.3 W, a 20-fold decrease in power compared to the case without air pockets. In **Table 2**, the numerical values for the parameters used in these calculations are reported.

Table 2 Comparison of the power needed to maintain the fluidic chip at 25°C (\dot{q}) in the case where a bulk PDMS layer is used or insulating air pockets are implemented in the PDMS layer. The thickness of the layer (d_i), the area perpendicular to the heat flow direction (A_i), the thermal conductivity of the material at 25°C (k_i) [Rumble, 2018], and the heat resistance (R_i).

	d_{PDMS} (μm)	A_i (mm^2)	k_i ($\text{W}\cdot\text{m}^{-1}\cdot\text{K}^{-1}$)	R_i ($\text{K}\cdot\text{W}^{-1}$)	\dot{q} (W)
bulk	100	23.50	0.15	28	6.5
air pockets	100	1.21	0.15	553	0.3

2. Microfluidic chip fabrication procedure

The microfluidic chip is formed by a silicon injector chip, a sealing layer and a channel layer (Figure 13).

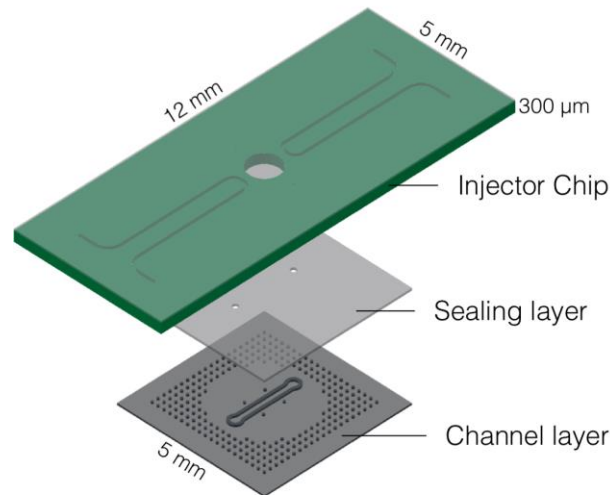


Figure 13 The different layers forming the microfluidic chip. Schematic courtesy of Marie Fuest, PhD.

The injector chip connects the macroscale tubing to the microfluidic channel.

The sealing layer is a thin PDMS membrane against which the channel layer is bonded. It allows the introduction of the sample from the injector chip to the microfluidic channel via laser cut holes.

The channel layer is a thin PDMS layer on which channel features are patterned using standard soft lithography.

For the fluidic chip fabrication, a similar procedure to the one reported by Mejia *et al.* was used [Mejia *et al.*, 2014] (Figure 14). In the procedure used in this work, the dimensions of the injector chip were modified for compatibility with pre-existing freeze substitution workflows. Also, the parylene deposition step before peeling of the channel layer from the mold was removed.

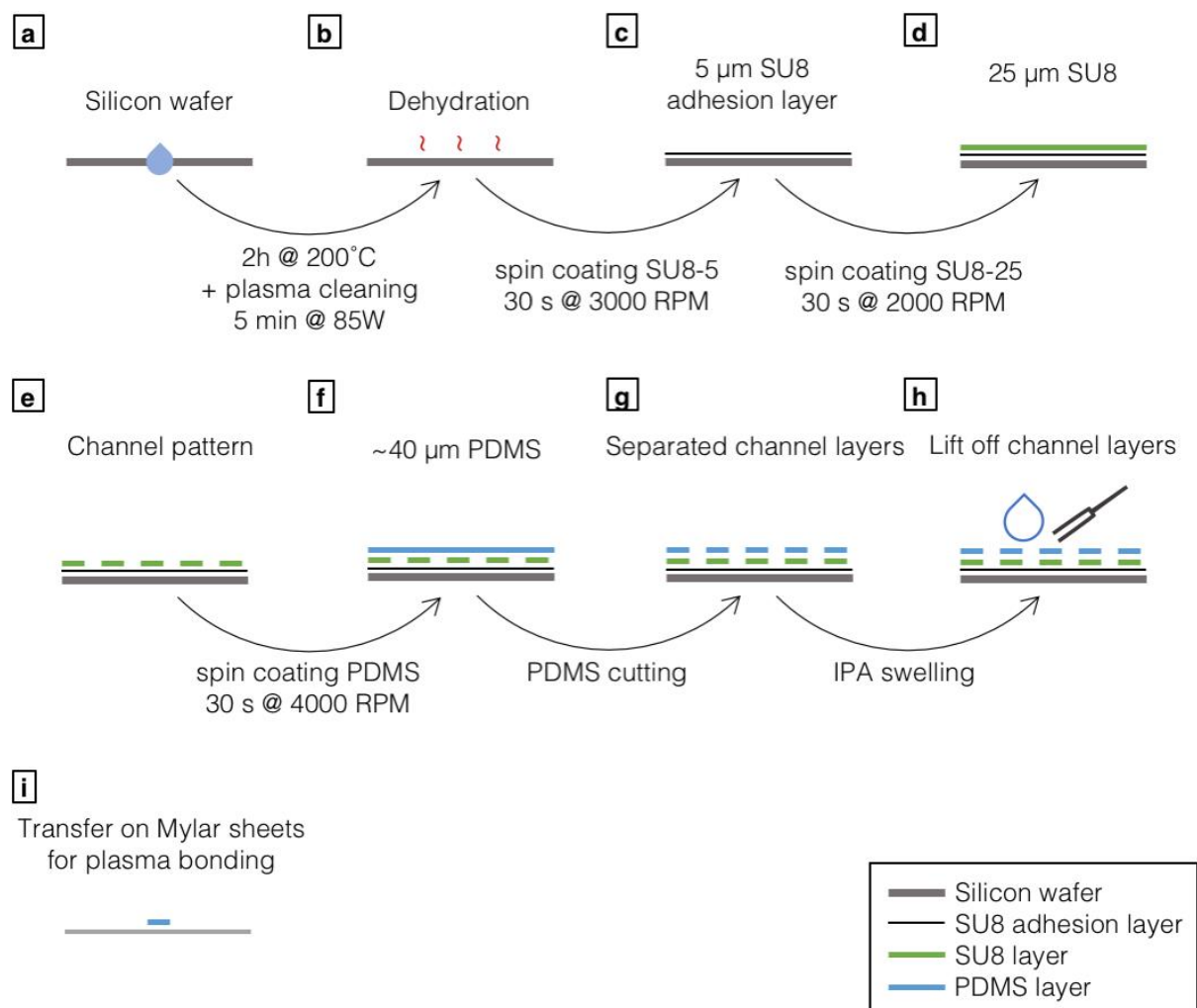


Figure 14 Workflow for the fabrication of the microfluidic channel layer of the microfluidic chip for cryofixation.

The mold (SU-8 master) for patterning the channel features was fabricated using soft lithography. Prior to lithography, a silicon wafer was placed in an oven at 200°C for 2 hours to remove most of the water adsorbed to the surface. After baking, the wafer surface was plasma cleaned for 5 minutes at 85 W (**Figure 14a-b**). Skipping this dehydration step would result in the bubbles formation in the photoresist.

To provide a 5 μm adhesion layer, the wafer was spin coated for 30 seconds at 3000 rpm with an acceleration of 6000 rpm/s with negative epoxy photoresist (SU-8 5, MicroChem). The wafer was then baked according to the manufacturer data sheet and fully exposed to UV light to be then post-baked to cure (**Figure 14c**). Next, the wafer was spin coated with negative photoresist (SU-8 25, MicroChem) for 30 seconds at 2000 rpm with an acceleration of 6000 rpm/s, resulting in a 25 μm thick layer and then baked according to the manufacturer data sheet (**Figure 14d**). A photolithography mask was used to selectively expose the photoresist layer to UV light in the shape of the fluidic patterns. The wafer was then post-baked to cross-link the

exposed photoresist and uncured photoresist was removed by dissolving it in SU-8 developer (**Figure 14e**).

To form the PDMS structures, PDMS monomer and cross-linker (SYLGARD 184 silicone elastomer, Dow Corning) were mixed in 10:1 ratio and degassed for 30 minutes. For the channel layer fabrication, the silicon master was spin coated with uncured PDMS for a total thickness of about 40 μm (**Figure 14f**). PDMS was cured in an oven at 80°C for 30 minutes. Once cured, channel layers were cut directly on the master in square shapes with sides of about 5 mm using a scalpel blade (**Figure 14g**). Cut patterns were then removed from the master using isopropanol (IPA) and tweezers (**Figure 14h**) to be then transferred on Mylar sheets to dry (**Figure 14i**).

The fabrication workflow of the sealing layers is shown in **Figure 15**.

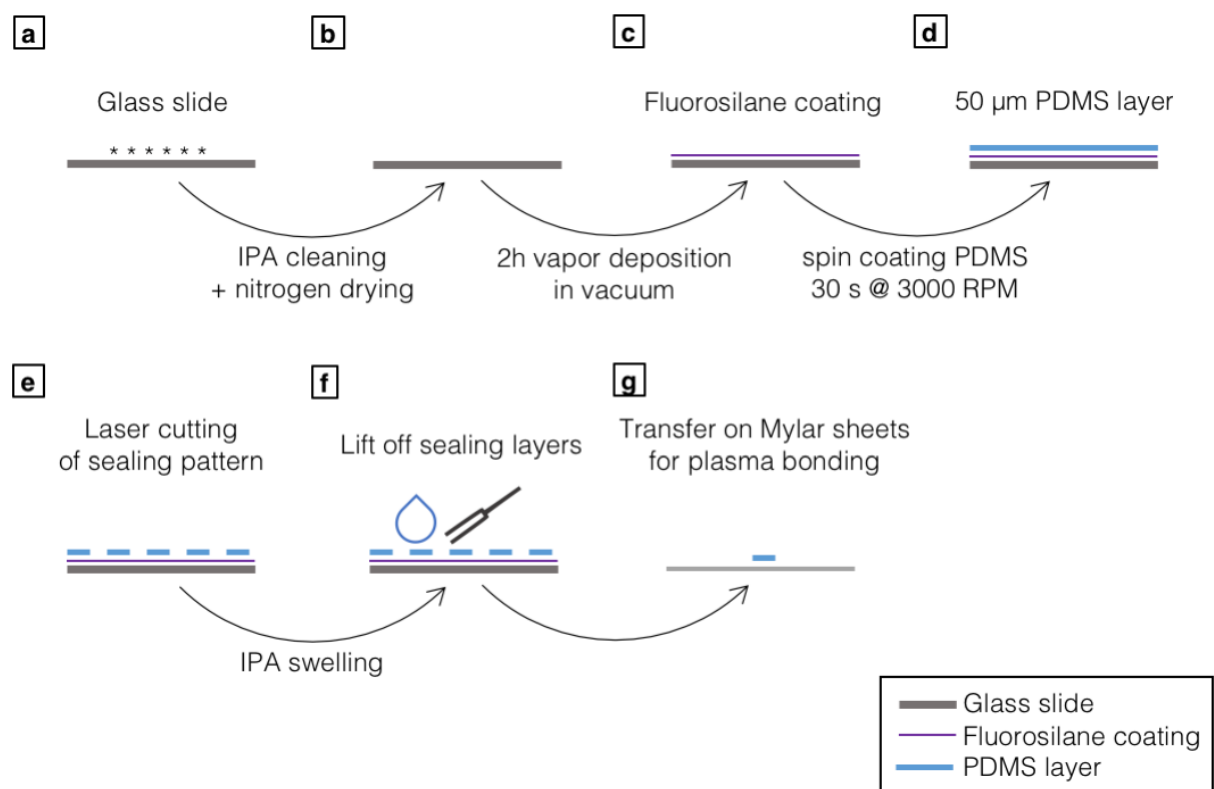


Figure 15 Workflow for the fabrication of the sealing layer of the microfluidic chip for cryofixation.

Large microscope glass slides were rinsed with IPA to remove dust particles (**Figure 15a**). Clean slides were then coated with fluorosilane (1H,1H,2H,2H-Perfluorooctyltrichlorosilane 97%, Alfa Aesar) via vapor deposition in a vacuum chamber for 2 hours (**Figure 15b-c**). Uncured PDMS was spin coated on the fluorosilane-coated slides for a thickness of about 50 μm (30 seconds at 3000 rpm with an acceleration of 6000 rpm/s) (**Figure 15d**). PDMS was cured in an oven at

80°C for 30 minutes. Holes and the layer outline were cut out using a laser cutter (VLS4.60, Universal Laser System, 40 W power) (**Figure 15e**). Holes were about 50 μm in diameter and the layer was cut in a square shape with sides of 5 mm. In **Table 3**, typical parameters for the laser cutting of the layers are reported.

Table 3 Laser cutter parameters for the making of the sealing layers of the microfluidic chip for cryofixation.

	Holes	Lines
Power (%)	1	5
Speed (%)	100	100
PPI	100	500

Cut patterns were then removed from the microscope slides using IPA and tweezers (**Figure 15f**) to be then transferred on Mylar sheets to dry (**Figure 15g**).

The same Mylar sheets were later used as handling support during the plasma bonding steps. Mechanical micromanipulators were used to align and put in contact the layers for bonding. To assemble the microfluidic chip, first the sealing layer was bonded to the injector chip and then the channel layer was bonded to the sealing layer (cf. **Figure 13**).

3. Main heater fabrication procedure

In **Figure 16**, the workflow for the fabrication of main heaters for the microfluidic device for cryofixation are shown.

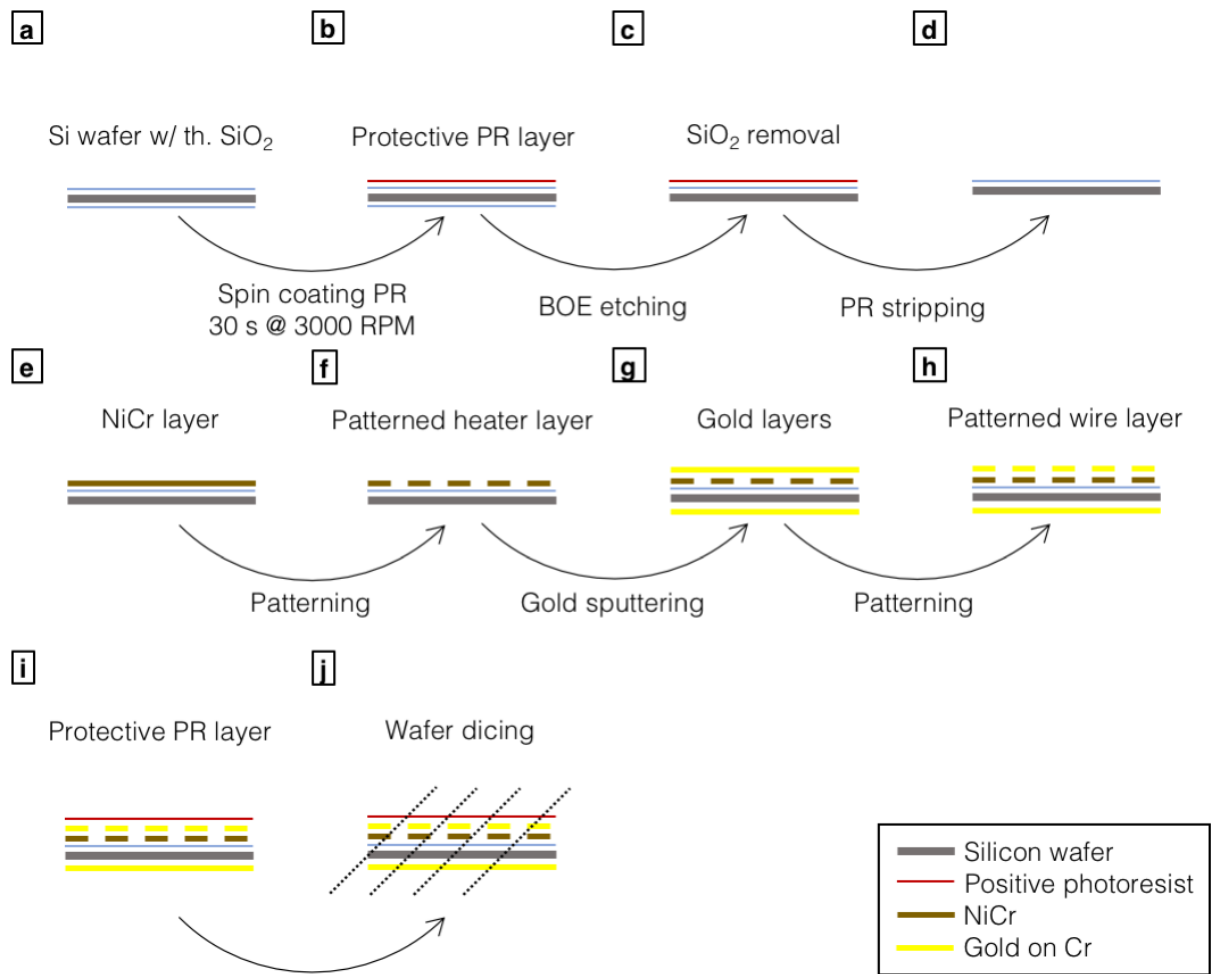


Figure 16 Workflow for the fabrication of the main heater for the microfluidic device for cryofixation.

A double side polished silicon wafer with 2.5 μm of thermal SiO₂ was used as substrate (**Figure 19a**). One side of the wafer was spin coated with a $\sim 7 \mu\text{m}$ layer of positive-tone photoresist (AZ 4562, MicroChemicals) (**Figure 19b**). The thermal oxide on the unprotected side of the wafer was chemically etched using a proprietary mixture based on ammonium fluoride and hydrofluoric acid (Buffered Oxide Etch, Transene) (**Figure 19c**). Positive photoresist was dissolved from the wafer using the suited remover solution (TechniStrip P 1316, MicroChemicals) (**Figure 19d**).

Residues from the photoresist were removed by submerging the wafer in a freshly made piranha solution for 5 minutes. A nickel-chrome (NiCr) layer of 600 nm was sputtered on the SiO₂ side of the silicon wafer (**Figure 19e**). The NiCr layer was spin coated with 5 μm of positive photoresist (AZ 4562, MicroChemicals). A photolithography mask was used to pattern the photoresist with the heater strip layout via UV light exposure. The wafer was developed using a proprietary mixture based on tetramethylammonium hydroxide, 2.4% solution in water (AZ 826MIF, MicroChemicals). Unprotected NiCr was etched using a proprietary mixture of

cerium ammonium nitrate solution (Nichrome Etchant TFN, Transene) (**Figure 19f**). Positive photoresist was dissolved from the wafer using the suited remover solution (TechniStrip P 1316, MicroChemicals).

Both sides of the silicon wafer were sputtered with gold (**Figure 19g**). On the side with the NiCr features, 400 nm were sputtered to pattern wire traces. On the side without features, 50 nm were sputtered as an adhesion promoter for the indium bond. Before each gold deposition, a 5 nm chrome layer was sputtered as an adhesion layer. The gold layer for the wire traces was patterned with a similar photolithography procedure to the one already described for the NiCr etching (Gold etchant, Ref. 651842, Sigma-Aldrich; Chrome etchant ETCH N°1, Technic) (**Figure 19h**).

The patterned side of the wafer was spin coated with a 5 μm layer of positive photoresist (AZ 4562, MicroChemicals) to protect the features from dicing debris (**Figure 19i**). The wafer was then diced to obtain main heater chips of the suited size (4 x 15 mm) (**Figure 19j**).

3.1. Main heater with temperature sensors fabrication procedure

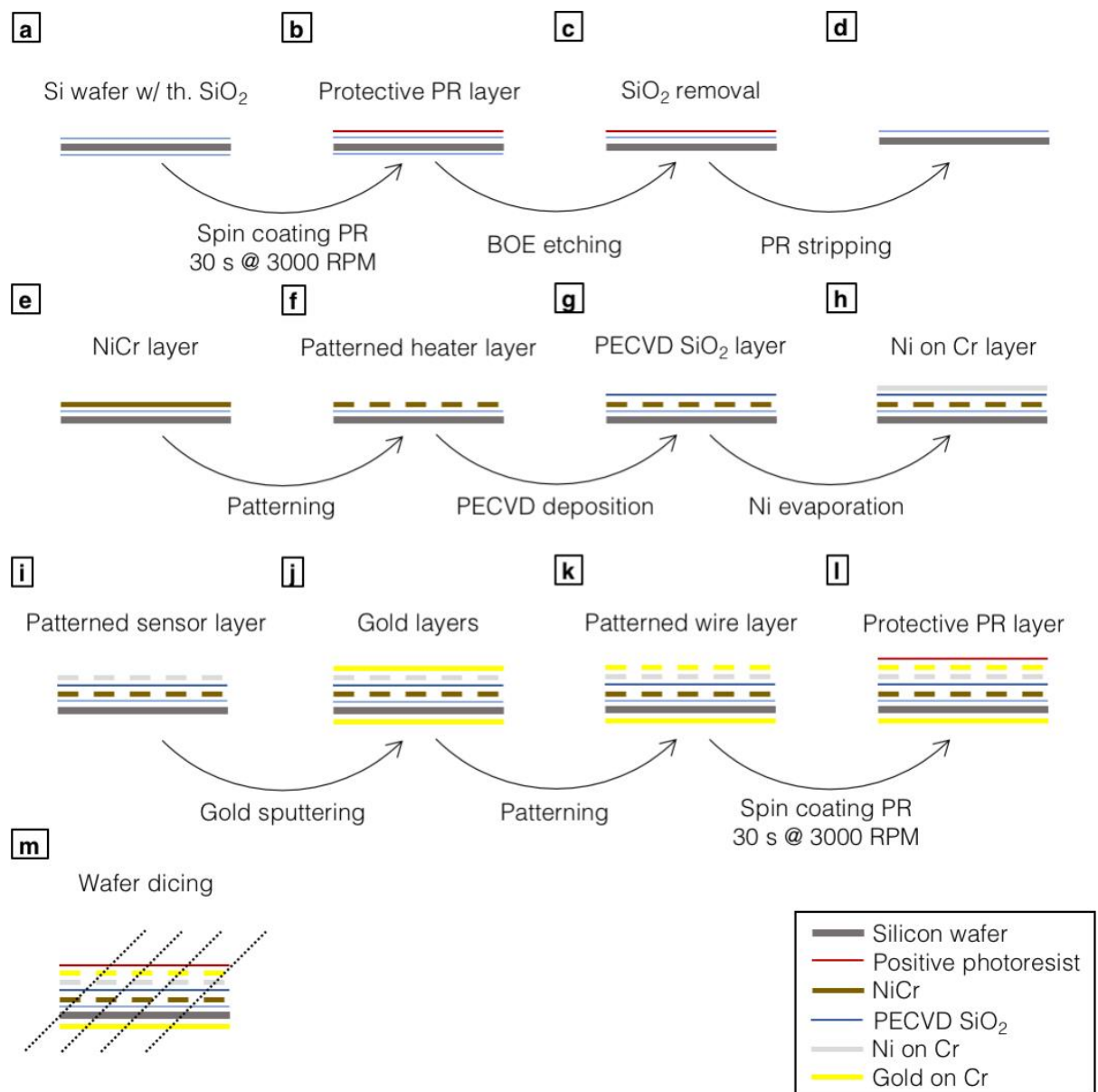


Figure 17 Workflow for the fabrication of the main heater with temperature sensors for the microfluidic device for cryofixation.

A double side polished silicon wafer with 2.5 μm of thermal SiO₂ was used as substrate for the fabrication of the main heaters with electronic temperature sensors (**Figure 17**). Silicon dioxide etching and NiCr deposition and patterning steps were carried out as for the main heater wafer without electronic temperature sensors (**Figure 19a-f**).

The NiCr patterned wafer was loaded in a Plasma Enhanced Chemical Vapor Deposition (PECVD) chamber. Argon plasma at a power of 50W was generated in the chamber to clean the

wafer surface from possible organic residues. Following the plasma cleaning, a 1 μm thick layer of SiO_2 was deposited on the NiCr side of the silicon wafer (**Figure 19g**).

Next, a nickel layer of 20 nm was sputtered on top of the PECVD SiO_2 using 5 nm chrome as adhesion layer (**Figure 19h**). The nickel layer was spin coated with positive photoresist (AZ 4562, MicroChemicals) of 5 μm in thickness. The photoresist was then patterned with the outline of the temperature sensors via UV light exposure and developing (AZ 826MIF, MicroChemicals). Unprotected nickel and chrome portions of the layers were etched off with suited etching solutions (nickel etchant TFG, Transene; Chrome etchant ETCH N°1, Technic) (**Figure 19i**). Remaining positive photoresist was dissolved using the suited stripping solution (TechniStrip P 1316, MicroChemicals).

To allow electrical connection to the NiCr layer, the PECVD SiO_2 was etched in correspondence of the NiCr strip extremities. First, the wafer was spin coated with a 5 μm thick layer of positive photoresist (AZ 4562, MicroChemicals). Then, the photoresist was exposed under UV light to pattern the regions of PECVD SiO_2 to be etched. The positive photoresist was then developed (AZ 826MIF, MicroChemicals) and the PECVD SiO_2 was etched off in BOE (Buffered Oxide Etchants, Transene) to create the connecting pads. Positive photoresist was stripped with the usual procedure (TechniStrip P 1316, MicroChemicals).

Both sides of the wafer were then sputtered with gold on chrome as adhesion layer. On the patterned side, 250 nm of gold on 15 nm of chrome were deposited. On the back side, 50 nm of gold on 15 nm of nickel were deposited. Gold was patterned to create wire traces connecting to the heater strip and temperature sensors. Gold deposition, patterning and wafer dicing were carried out as already described for the heater wafer without electronic temperature sensors (**Figure 19j-m**).

4. Heat transfer maximization

In **Figure 18**, the details of the cold post and the heat sink assembly are shown. In the previous generation of the device [Mejia *et al.*, 2014], the post and the heat sink were forming a single cryostage. The separation of the cold post from the heat sink was crucial for the assembling process of the second generation device used in this work. However, it also generated one additional interface along the heat path. The presence of interfaces between the heater and the heat sink impedes the heat dissipation from the main heater to the liquid nitrogen bath. This is because with every interface oxide layers and air gaps are inevitably formed increasing the heat

resistance of the heat path. The overall effect of a Poor heat dissipation degrades the quality of the cryofixation.

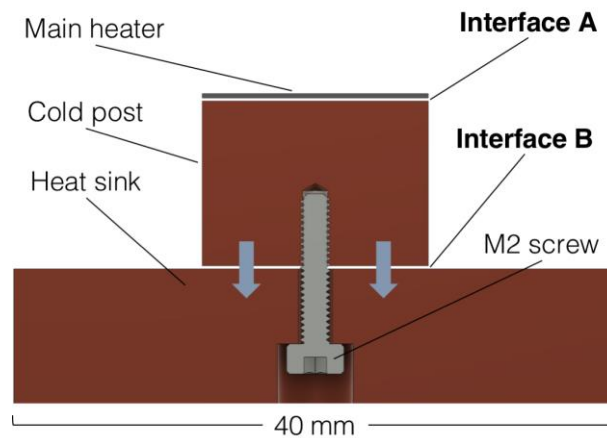


Figure 18 Cross section schematic showing the interfaces between the main heater, the cold post and the heat sink. A similar setup was also used to characterize the heat resistance of different interface materials.

To maximize the heat transfer across the device despite the presence of interfaces, a series of interface materials were characterized reading their heat resistances. The heat resistance of the bare surfaces (“No material”) was used as reference to assess the quality of the other interface materials (**Figure 19**).

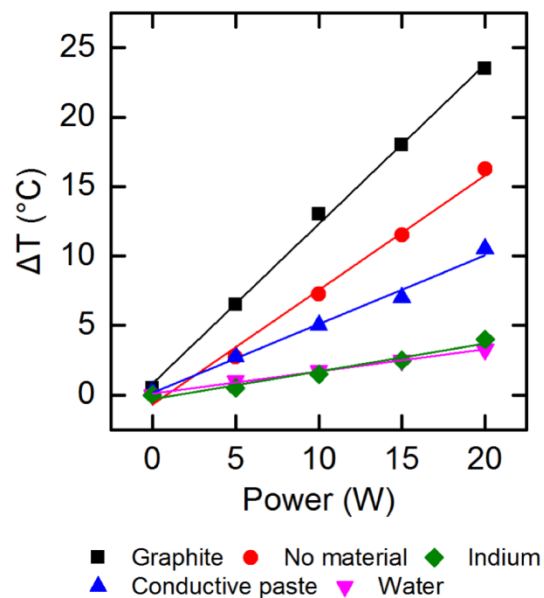


Figure 19 Measurement of the temperature rise of the cold post as a function of heating power for different interface materials. The bare interface (“No material”) was used as a reference to assess the quality of other interface materials.

Table 4 Heat resistance values and their respective standard errors (SE) measured for different interface materials.

INTERFACE MATERIAL	HEAT RESISTANCE \pm SE ($^{\circ}\text{C}\cdot\text{W}^{-1}$)
Graphite	1.2 ± 0.03
No material	0.8 ± 0.04
Conductive paste	0.5 ± 0.03
Indium	0.2 ± 0.02
Water (solid)	0.2 ± 0.006

From **Table 4**, it is possible to see that not every interface material improved the reference condition. In fact, using graphite heat resistance increased by 50%. On the other hand, using indium foil as the interface material, it was possible to match the heat resistance of water.

The use of water as the interface material was discarded because of practical reasons. First, water promotes the oxidation of the copper surfaces that would increase heat resistance over time unless manually removed. Second, water tends to evaporate if the device is not immediately used after the assembling procedure. Third, a supplementary and permanent fixing mechanism would be necessary to hold the mechanical components in place when water is in a liquid state. Because of its low heat resistance, indium (Indium solder ribbon, 99.99% indium, Indium Corporation) was chosen as the interface material between the device components (**Figure 18**, Interface A and B).

Due to the different requirements of the two interfaces with the cold post, indium was applied via two different methods: indium bonding and mechanical compression. To form the indium bond (Interface A), the cold post was heated up on a hot plate to 200°C and a small bead of indium was placed on the post and allowed to melt. To remove the oxides and spread the melted indium over the post surface, a drop of liquid flux was used (Flußmittel C66, Amasan). If necessary, more indium was added onto the post. Flux residues were cleaned off the post using a cotton swab and deionized water (DI water). Once the indium was cleaned, the main heater was placed on top and aligned with the help of a custom-made tool. After the alignment was completed, the hot plate was turned off and the indium was left to solidify at room temperature.

To ensure proper heat dissipation between the cold post and the heat sink (Interface B), an indium foil of about $100\ \mu\text{m}$ in thickness was placed between the components. Tightening of a screw through the heat sink and into the cold post ensured proper contact between the surfaces.

For the measurement of the heat resistance of Interface B (cf. **Figure 18**), a NiCr wire of about 5 cm in length was bent in a loop, wrapped on itself and glued on top of a cold post (Stycast 2850 FT Black Epoxy, Emerson & Cuming). The device was equipped with two temperature sensors (Pt1000, Farnell), one glued on the cold post and the second glued on the heat sink. Interface materials used for characterization were placed between the cold post and the heat sink. The heat resistance was measured by computing the difference in temperature between the cold post and the heat sink against the power applied at the NiCr wire.

5. Assembly setup procedure

For the assembly of the fluidic part (**Figure 20a**), the microfluidic chip is first loaded into the copper holder with the microfluidic channel facing downwards (**Figure 20a** inset 1). To prevent freezing of the U-shaped bypass channels, an auxiliary heater is placed onto the chip and it is held in place by a retaining ring (**Figure 20a** inset 2).

Printed circuit boards (PCBs) are glued and wire bonded to the microfabricated heater chip. Then, the heater is indium bonded to the cold post as described previously (**Figure 20b**).

For the assembly of the remaining parts, the cold post with the indium bonded main heater is first placed inside an aluminum frame (**Figure 20c-d**) and then the fluidic part is placed on the same frame over the heater and retained in position via magnets. At this stage of the assembling process, the main heater and the microfluidic channel are still separated. Using a xyz θ -axis micromanipulator (**Figure 20c**), the cold post is aligned to the main heater and put into contact with the microfluidic channel. In the inset of **Figure 20c**, a channel (red dashed lines) aligned and in contact with the main heater (blue dashed lines) is shown. Once in contact, the parts are locked in position using UV glue (NOA81, Norland Products). Next, macroscale tubing (silicone tubing 0.51ID-0.94OD, Dow Corning) is connected using a flange system sealed by o-rings. After the dry-box is placed on the aluminum frame, the last auxiliary heater is attached to the bottom side of the aluminum frame using magnets. Later, the assembly is connected to the heat sink as previously described.

After the assembling is completed, the device is loaded into the empty liquid nitrogen bath and connected to the data acquisition and temperature control electronics. Finally, the device is placed on the microscope stage for the experiment (**Figure 20d**).

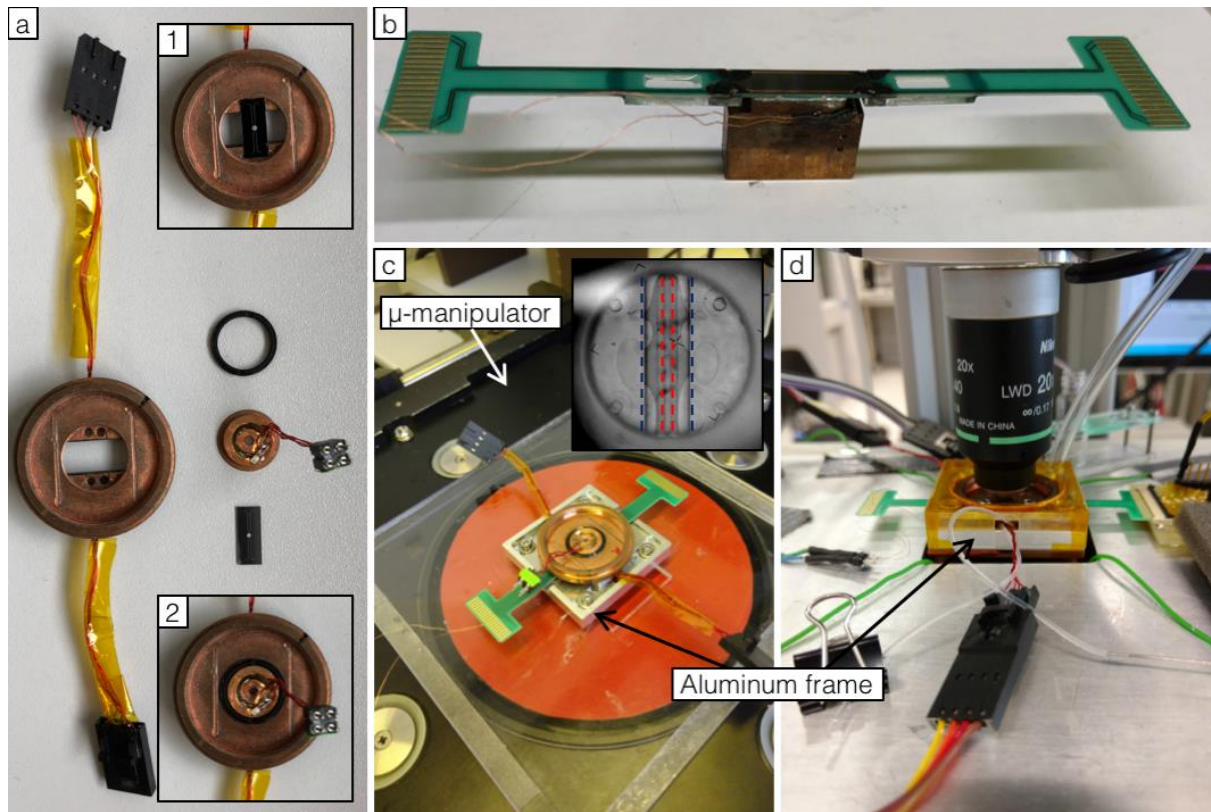


Figure 20 Main steps of the assembly process of the microfluidic device for cryofixation. (a) Fluidic components of the device: the microfluidic chip is inserted in the copper holder (inset 1), the ring heater that maintains the U-shaped bypass channels at room temperature is held in place by a retaining ring (inset 2). (b) First, the PCBs for electrical connection are glued and wired to the microfabricated main heater. Then, the heater chip is indium bonded to the cold post. (c) Using a micromanipulator and a stereomicroscope, microfluidic channel and main heater are aligned and put in contact (inset), then glued in position using UV glue. (d) After attachment to the heat sink, the device is loaded into the empty liquid nitrogen bath, electrical connections are plugged in and the complete assembly is moved onto the microscope stage to start the experiment.

6. Electronic controls of the setup for *in situ* cryofixation

Power to the main heater was delivered by an external power supply (N5750A, Agilent Technologies). Power to the four auxiliary heaters was supplied via two custom made circuit boards. Each board was provided with an Arduino board (Arduino Micro, Arduino) that controlled the power for two of the auxiliary heaters. The temperature of the parts was read via a resistance temperature detector (NI9226, National Instruments) and adjusted via a PID loop. To have the fastest possible freezing, cryofixation was performed by opening a solid-state relay placed within the main heater electrical circuit. For the experiments, main and auxiliary heaters were controlled via a LabView interface. Electronic controls for the microfluidic device for cryofixation, from the design of the circuit boards to the realization of the LabView interface, were developed by Mario Matteo Modena, PhD.

7. Rhodamine B temperature dependence

Rhodamine B (RhB) in water has maxima of excitation and emission at 554 nm and 576 nm, respectively [Kristoffersen *et al.*, 2014]. To confirm that rhodamine B was suitable as a non-contact thermometer in the microfluidic device for cryofixation, a 1% (m/m) solution of rhodamine B (Rhodamine B-ITC-Dextran, 70 kDa, Sigma-Aldrich) in DI water was loaded into the channel and imaged with a 10x/0.3 NA air objective, a 405 nm LED lamp with suited filter set (75 HE, Zeiss) and an Andor Neo sCMOS camera with 0.5 s exposure time. For each measurement, an ROI within the channel was selected and its intensity averaged after background subtraction. The temperature of the system was controlled using a PID loop implemented by a temperature controller (TED 200 C, ThorLabs), a temperature sensor (TH10K, ThorLabs) and a Peltier element (TEC3-2.5, ThorLabs). The temperature of the device was changed from 15 to 35°C with 5°C intervals and fluorescence intensity was recorded at each interval after temperature equilibration. Measurements were performed during both heating and cooling cycles to ensure the absence of bleaching or any other hysteresis effect.

8. Rhodamine B bead measurements

A square capillary (40 x 400 μm) was filled with 1 μm rhodamine B-loaded melamine beads in water (Sigma-Aldrich, ref. 90518) as provided by the manufacturer. The ends of the capillary were sealed with Vaseline (Roth, ref. 5775.2). The capillary was placed on a block of black anodized aluminum, then a glass coverslip was placed on top of the capillary before image acquisition. The microscope was equipped with a 20x/0.40 NA air objective with 3.9 mm working distance, a mercury lamp was used as light source (IntensiLight, Nikon), filter set was composed of a 546/10 nm excitation filter, a 575 nm dichroic mirror and a 580 nm longpass emission filter. Image acquisition was done using an Andor Neo sCMOS camera with 500 ms exposure time.

9. Main heater calibration procedure

Prior to each experiment with *C. elegans*, the temperature of the channel was calibrated by first measuring the fluorescence intensity of the 1% (m/m) rhodamine B solution in DI water at room temperature. The heat sink was then cooled to liquid nitrogen temperature and the power to the thin-film resistive heater was tuned to ensure the rhodamine B intensity matched the room

temperature value within $\pm 3\%$ of the initial value. Power at the main heater was not directly controlled. Instead, the value of a proportionality constant (k_{prop}) was tuned to adjust the power applied according to the temperature measured at the cold post.

Nematode motility is a commonly used indicator for the physiological health state of the nematode. Here, motility was used as an independent rough indicator for the outcome of the calibration procedure.

10. *C. elegans* sample preparation

C. elegans were grown on nematode growth medium (NGM) agarose plates, fed with *E. coli* OP50 and incubated at 20°C [Brenner, 1974]. For sample preparation, the surface of an agarose plate was washed with about 2 mL of M9 buffer and 10% (m/m) cryoprotectant. The worm suspension was filtered through a nylon membrane filter with 10 μm pore size (Nylon Net Filter 10 μm , Millipore) to concentrate L1 worms. The worms were then collected in a vial for pressure-driven injection in the microfluidic device or in a plastic syringe for manual injection. Except for the sample used for the high speed recorded cryofixation, all samples were filtered before injection. Specimens used in this work (wildtype and GCaMP strains) were kindly provided by the Bringmann Lab of the Max Planck Institute for Biophysical chemistry, Göttingen.

Different cryoprotectants have been used in this work (e.g. trehalose, glycerol, sucrose) before a toxicity screening was run. Trehalose (D(+)-trehalose dihydrate, Carl Roth) is a disaccharide known to be a good cryoprotectant [Chiu, Kelly and Walz, 2011; Warkentin, Sethna and Thorne, 2013]. Our toxicity assay of 8 different types of commonly used cryoprotectants showed the highest survival rate for *C. elegans* in 10% (m/m) trehalose, with a survival rate of $92\% \pm 5\%$ in M9+10% (m/m) trehalose compared to $97\% \pm 3\%$ survival in the M9 control. The toxicity study was carried out by Jan-Erik Messling during his Master's thesis within our laboratory.

11. Post-cryofixation sample transfer

For the measurement of the time limitations for the transfer step, a simplified version of the cryofixation device was used. A heat sink and a cold post were assembled together using indium foil as the interface material. The components were submerged in liquid nitrogen and the temperature of the cold post was measured via a resistance-based temperature sensor (Pt1000,

Farnell). When temperature was stabilized at the liquid nitrogen temperature (-196°C), the partial assembly was removed from the liquid nitrogen bath and temperature was recorded until it increased above the glass transition temperature of water (-137°C).

12. Sample preparation and imaging for CLEM

C. elegans specimens were cryofixed in M9 buffer with 10% (m/m) glycerol (Invitrogen) as cryoprotectant. Samples were imaged using a Canon EOS 700D digital camera attached to an infinity-correction tube (Proximity series, InfiniTube) and a 10x/0.2 NA air objective with a 14.3 mm working distance. After recovering of the microfluidic device from the assembly, the microfluidic channels were opened near the inlet and outlet holes of the silicon injector chip using a razor blade. The operation was carried out working with the sample and tools under liquid nitrogen level. Tools were pre-cooled to liquid nitrogen temperature before touching the sample.

Samples were processed for freeze substitution at -90°C using a Leica EM AFS (Leica Mikrosysteme). First, they were submerged in anhydrous acetone with 0.1% tannic acid for 24h and later in anhydrous acetone, 2% OsO₄, 0.5% anhydrous glutaraldehyde (EMS Electron Microscopical Science) for additional 8 hours. Freeze substituted *C. elegans* were embedded in Agar 100 (Epon 812 equivalent) that was cured at 60°C over 24h. Samples were sectioned into ~70 nm thick sections with an ultramicrotome and imaged in transmission electron microscopy (TEM) (CM120, Philips Inc. Eindhoven, The Netherlands). This particular freeze substitution procedure (staining, chemical fixation and resin embedding parameters) was chosen because it enhances the contrast of otherwise poorly visible biological ultrastructures (membranes, nuclei), suitable for morphological studies and, for the purpose of this study, to emphasize possible ice crystallization artefacts. Freeze substitution, sectioning and imaging by TEM were performed by Dr. Dietmar Riedel of the Facility for Transmission Electron Microscopy of the Max Planck Institute for Biophysical Chemistry in Göttingen.

13. Cryoimmersion light microscopy of cryofixed *C. elegans*

C. elegans expressing GCaMP were cryofixed using the microfluidic device for cryofixation. Sample preparation prior to injection was executed as previously described and 10% (w/w) trehalose in M9 buffer was used as cryoprotectant. Samples were cryofixed in collaboration with Marie Fuest, PhD and Rodrigo Galilea Kleinstaubler. Images in cryoimmersion were acquired in collaboration with Margherita Bassu, PhD.

Prior to cryoimmersion light microscopy, the state condition of the microfluidic channel and sample was assessed using a low numerical aperture air objective (10x/0.2 NA). Frost was usually found on the outside of the microfluidic channel. To improve the image quality of the sample, the channel was cleaned from the frost using a looped copper wire pre-cooled in liquid nitrogen (**Figure 21**).

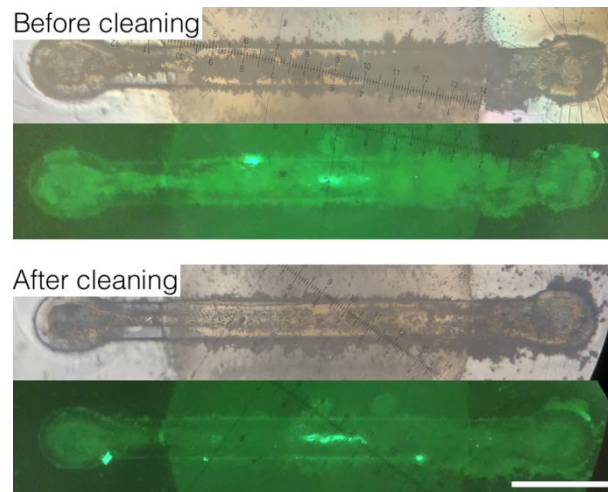


Figure 21 Before cryo-immersion, samples were checked using a low-NA air objective (10x/0.2 NA) to confirm the integrity of the microfluidic chip and sample. After the transfer process from the cryofixation device, frost was found on the outside of the microfluidic channel. To improve the image quality, a looped copper wire was used to displace the frost. Scale bar measures 300 μm .

For the quality check, a dedicated setup was developed (**Figure 22**). Compared to the cryoimmersion setup, this setup allowed a faster turnover by keeping the sample in a moisture-free cryo-temperature environment with the compromise of using a lower NA air objective. The setup consisted of a liquid nitrogen bath with a custom made acrylic support to hold the different required components and a retractable plastic shield around the dewar to confine the nitrogen vapor and to minimize frost formation. The acrylic support had access slots for liquid nitrogen refill, cooling of tools (e.g. tweezers, sample cleaning tools), an aluminum stage for the imaging of the cryofixed sample, a vial holder for the sample transfer and a heater for the generation of nitrogen gas to keep a positive pressure inside the observation chamber (**Figure 22a**). The aluminum imaging stage, vial holder and resistive heater were all in contact with liquid nitrogen during the experiment. Once the sample was transferred on the imaging stage, the vial was removed from the holder. An acrylic lid was placed onto top of the acrylic support to enclose the sample in a moisture-free and cryogenic environment (**Figure 22b**). Positive pressure was maintained within the observation chamber by the continuous boiling of liquid

nitrogen in contact with the resistive heater. With the acrylic lid in place, the dewar was moved under the microscope. The lid was provided with an access port for liquid nitrogen refill, an observation window in correspondence to the aluminum stage, NdFeB magnets for the dry-tent and holes from which dry nitrogen was flushed from the dewar to the dry-tent. The dry-tent consisted of a thin plastic foil taped around an iron ring and sealed around the air objective. When the objective approached the sample, the iron ring engaged with the magnets on the acrylic lid providing a good seal against frost formation (**Figure 22c**). The microscope was equipped with a 10x/0.2 NA air objective with 14.3 mm working distance, a halogen lamp for brightfield imaging and a mercury lamp for fluorescence imaging with a Zeiss Set 38 HE filter set (Excitation filter: 470/40 nm, Dichroic mirror: 495 nm, Emission filter 525/50 nm). Images were acquired via the eyepieces of the microscope using a smartphone camera.

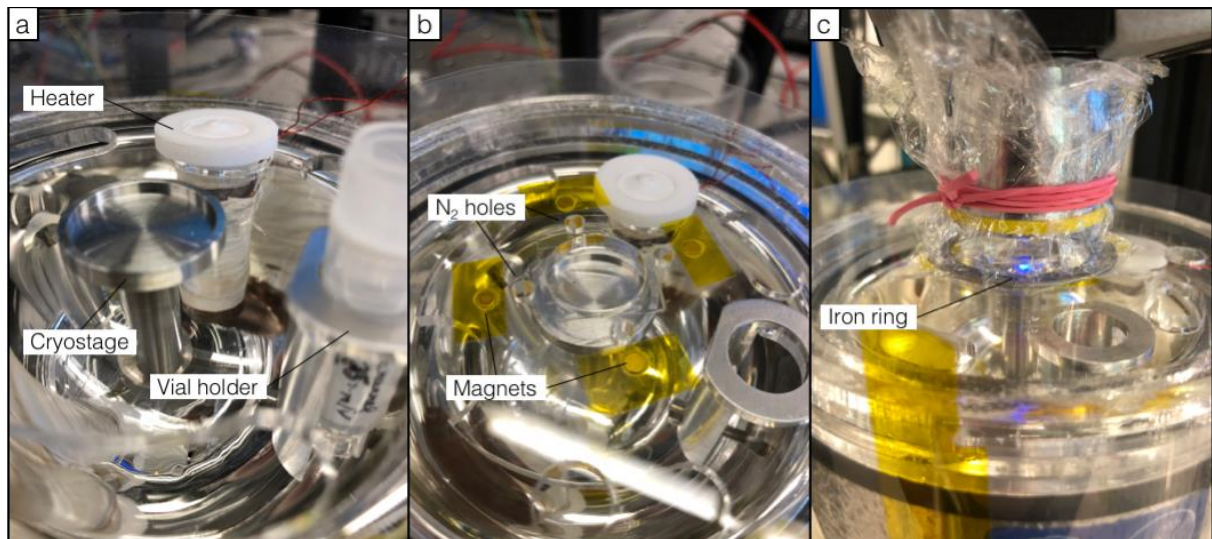


Figure 22 Setup for the quality check of the cryofixed sample before cryoimmersion light microscopy. (a) A dewar was equipped with an aluminum cryostage for imaging the samples, a vial holder and a resistive heater for the generation of dry gas nitrogen. (b) The sample was enclosed in a confined environment using an acrylic lid with an observation window. To prevent frost formation on the sample, a pressure was maintained inside the dry environment by the continuous boiling of liquid nitrogen in contact with the resistive heater. (c) A dry-tent with an iron ring was attached to the air objective. NdFeB magnets on the lid ensure good sealing of the dry-tent while nitrogen gas was flushed into the tent through holes in the acrylic lid.

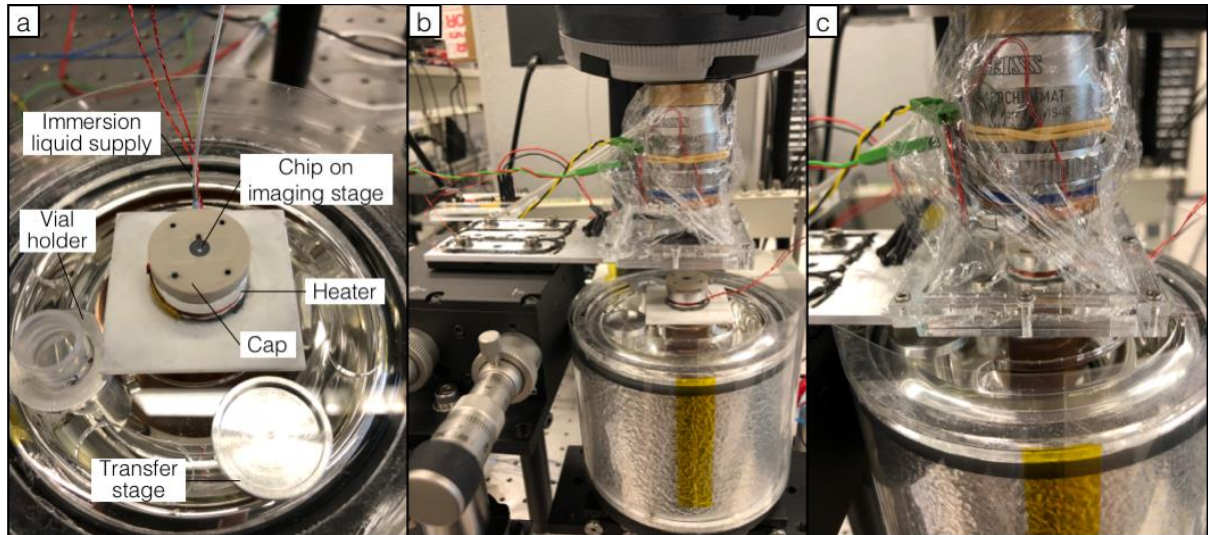


Figure 23 Setup for cryoimmersion light microscopy. The setup was modified from the one described by Faoro *et al.* [Faoro *et al.*, 2018] for imaging of cryofixed samples in microfluidic chips.

For the cryoimmersion light microscopy, the setup described by Faoro *et al.* [Faoro *et al.*, 2018] was modified to accommodate the microfluidic chip for cryofixation. The transfer of the microfluidic chip onto the cryo-immersion stage was done in a liquid nitrogen vapor environment to prevent recrystallization of the sample. Nitrogen gas was continuously generated by the heater of the imaging stage. The microfluidic chip was first moved from the vial to the transfer stage and then, in a second step, from the transfer stage to the imaging stage. To initiate cryo-immersion imaging, the sample was placed on a stage partially submerged in liquid nitrogen. The temperature of the stage was adjusted to the refractive index-matching temperature ($\sim 145^{\circ}\text{C}$) using a resistive heater wrapped around the stage. The fluid for the immersion objective (HFE-7200, 3M) was supplied through a tube reaching the sample via the cap holding the microfluidic chip onto the stage (**Figure 23a**). The stage with the liquid nitrogen dewar was then moved to the microscope (**Figure 23b**) and the stage was lifted to the immersion objective while its temperature was adjusted to match the refractive index of the cryo-immersion liquid (**Figure 23c**).

For the room temperature measurements, GCaMP *C. elegans* were washed from a culture dish using M9 buffer and embedded in 3% (w/w) agarose in M9 buffer. *C. elegans* in agarose were imaged between a glass slide and a coverslip using Kapton tape strips as spacers. The side of the coverslip sides were sealed with additional Kapton tape to minimize water evaporation.

The microscope used for the cryoimmersion imaging was a Axio Scope.A1 (Zeiss) equipped with a STEDYCON Unit (Abberior Instruments) for image acquisition. The image acquisition unit was used to record images in standard confocal and STED mode and it was equipped with the lasers reported in **Table 5**.

Table 5 STEDYCON lasers wavelength (nm) and maximum power (mW).

Laser	Wavelength (nm)	Max power (mW)
Excitation 1	488	0.155
Excitation 2	640	0.330
STED	775	730

Emission filters were a single bandpass filter (650-700 nm) and a double bandpass filter (502-572 nm + 608-627 nm). GCaMP was imaged using the 488 nm laser and the double bandpass filter. Granules were imaged using the 640 nm laser and the single bandpass filter. The objective used for the imaging was a water immersion Zeiss LD C-Apochromat 63×/1.15 NA, modified to enable cryo-microscopy below the glass transition temperature of water [Faoro *et al.*, 2018]. For every measurement, a dwell time of 10 us/pixel was used. For drift and bleaching measurements, one acquisition per line was collected. For two-color images (in confocal and in STED), five acquisitions per line were accumulated.

Chapter 3

Cryofixation of *Caenorhabditis elegans* within the field of view of a light microscope

Part of this chapter was published in “Cryofixation during live-imaging enables millisecond time-correlated light and electron microscopy” – M. Fuest*, [G. M. Nocera*](#), M. M. Modena, D. Riedel, Y. X. Mejia, T. P. Burg *Journal of Microscopy*, **2018**.

In this chapter, the ability to maintain the roundworm *Caenorhabditis elegans* (*C. elegans*) viable in the microfluidic cryofixation system and conduct cryofixation during live imaging was investigated. This is non-trivial task because the sample must be stably confined and temperature needs to be accurately controlled during live imaging.

Microfluidics is a useful tool for the handling of small organisms. A microfluidic chip can be designed to confine the organism while feeding nutrients over time. For imaging during neuronal and behavioral studies, however, it might be required to implement features that also impede undesired movements during data acquisition. For reversible anesthetization of drosophila larvae, mechanical compression was applied via a cooled deformable membrane [Chaudhury *et al.*, 2017]. To confine zebra fish larvae during the chemical stimulation, tridimensional obstacles within the microfluidic chip were implemented [Candelier *et al.*, 2015]. For *C. elegans*, narrow channels are generally used to limit the movements of the specimens [Chronis, Zimmer and Bargmann, 2007]. Here, to maintain the specimen within the FOV of the microscope without impeding its free movements, zig-zag features within the channel path were implemented.

Temperature is a critical parameter for the good health state of a living organism. Temperature control within the microfluidic channel is key for implementing the cryofixation system for life science experiment. In particular, to achieve cryofixation of a live imaged sample with framerate time resolution. To control the temperature of the channel, the calibration of the main heater was required. Here, the measurement of the fluorescence intensity of a temperature-sensitive dye (rhodamine B) was used to calibrate the main heater was used.

To assess the preservation quality of the samples, the capability of light microscopy for detecting ice formation was investigated.

1. *C. elegans* confinement in microfluidic channel

The model system selected for this work was the nematode *Caenorhabditis elegans*. *C. elegans* is a versatile model system used for various research fields (e.g. neuroscience [Schwarz, Lewandrowski and Bringmann, 2011], behavioral biology [Chronis, Zimmer and Bargmann, 2007], genetic studies [Brenner, 1974]). Its small dimensions, ~1 mm long and ~50 μm thick for the adult, make this nematode also suitable for microfluidic-based experiments. In particular, its first and smallest larval stage (L1) is about 12 μm thick and about 200 μm long. These dimensions make the L1 larval stage perfectly compatible with the microfluidic cryofixation system.

Carried by the flow or due to their own motility, *C. elegans* can easily leave the field of view (FOV) of the light microscope. About 0.05 bar applied to the microchannel (the minimum pressure measurable on the setup) was already sufficient to observe *C. elegans* flowing in the channel at about 4 mm/s. With a FOV of 300 μm , the nematode crossed from one side of the image to the other in about 75 ms. To control the position of specimens within the field of view, a system of traps was developed and incorporated in the microfluidic channel design (**Figure 24**).

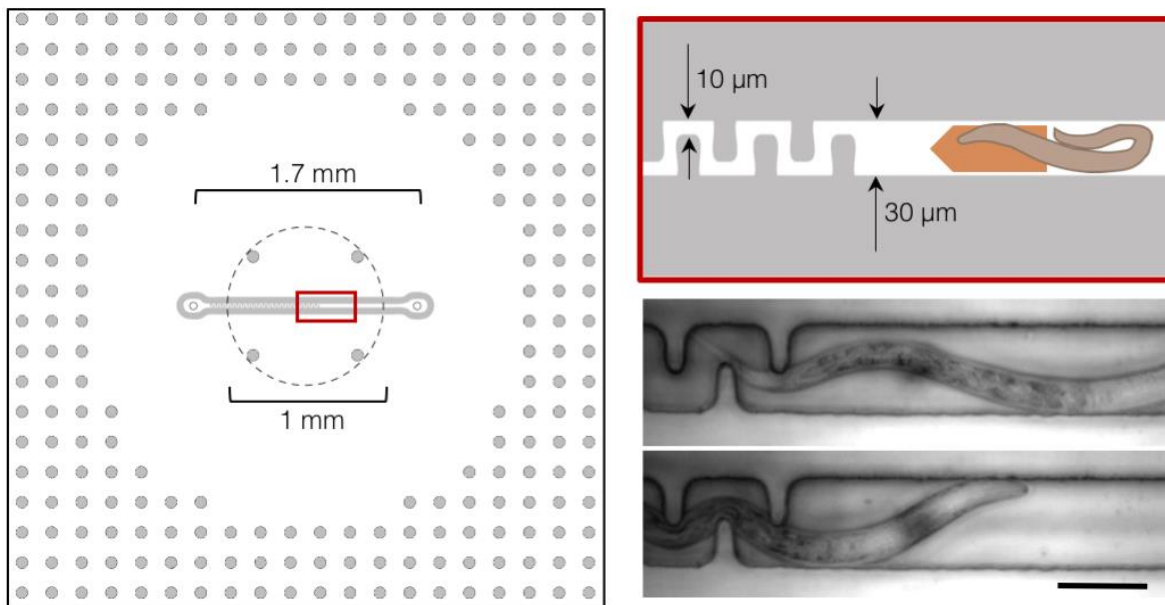


Figure 24 Microfluidic trap system to confine *C. elegans* within the FOV of the light microscope. When a suspension of *C. elegans* is injected into the microfluidic device, nematodes are stopped by the zig-zag feature of the channel (red inset). Depending on the experiment, the operator has the possibility to decide to have the nematode free to move in the larger part of the channel (upper photo) or restrain it into the narrow features of the channel to limit its body movements (lower photo). Scale bar measures 30 μm . Modified from [Fuest and Nocera et al., 2018].

The trap feature in the microchannel constrains the nematode in the field of view of the microscope (red inset) preventing it from moving across the whole microchannel length (1.7 mm). The narrow trap features of the microchannel (10 μm in width) have the dual purpose of increasing the flow resistance and creating physical obstacles for the nematode. The user can choose to stop the nematode at the trap entrance (upper photo) or to immobilize it within the serpentine features by applying flow pulses (lower photo).

2. Temperature control of the microfluidic channel enables cryofixation of living samples

In the previous version of the microfluidic device for cryofixation, the only parameter that indicated the temperature of the channel was the solid or liquid state of the channel contents [Mejia *et al.*, 2014]. With the aim to enable life science experiments in the cryofixation device, a more accurate temperature measurement was necessary. *C. elegans* are viable between 13 and 26°C [Wittenburg and Baumeister, 1999]. Therefore, the channel temperature had to be controlled with an accuracy of about $\pm 5^\circ\text{C}$. The results shown in this section demonstrate that this can be accomplished by calibrating the heater power based on the temperature-dependence of rhodamine B fluorescence.

During the experiment, the temperature within the microfluidic channel is controlled by the power applied at the main heater. The temperature within the microfluidic channel ($T_{channel}$) as a function of the heater power (P_{heater}) was modeled as

$$T_{channel} = k_{prop}^{-1} \cdot P_{heater} + T_{post} \quad (5)$$

With T_{post} being the measured temperature of the cold post and k_{prop} being a proportionality constant. Interface thermal conductivities and thicknesses can vary for each assembled device, preventing an accurate numerical solution for k_{prop} . Instead, k_{prop} is experimentally determined for each individual experimental setup.

Because of channel size constraints, common resistance-based temperature sensors or thermocouples could not be used to calibrate the main heater. To overcome this limitation, a temperature-dependent fluorescent dye was used. The quantum yield of rhodamine B (RhB) strongly depends on temperature in the 0-100°C range [Ross, Gaitan and Locascio, 2001], making this molecule a useful tool for non-contact temperature measurement [Ross, Gaitan and Locascio, 2001; Chauhan *et al.*, 2014; Soleilhac *et al.*, 2016]. To confirm that the rhodamine B change in fluorescence intensity was suitable for this application, a calibration curve was recorded similar to previous reporteds [Ross, Gaitan and Locascio, 2001] (**Figure 25**).

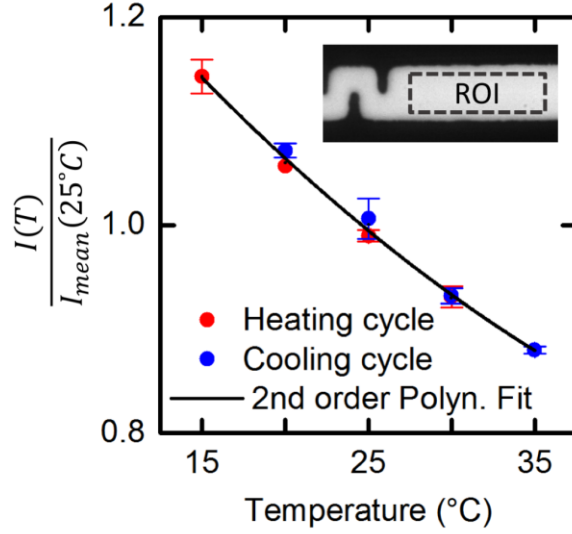


Figure 25 Measured intensity over temperature change for rhodamine B water solution. Rhodamine B is used to measure the temperature within the microfluidic channel in a non-contact fashion. Multiple heating and cooling cycles showed no hysteresis in the measurements. The temperature resolution was calculated from error bars and resulted in 0.6°C. Modified from [Fuest and Nocera et al., 2018].

The solid line in **Figure 25** represents a second order polynomial fit of the form

$$I = A_0 + A_1T + A_2T^2 \quad (6)$$

where I is the fluorescence intensity, T is the temperature and the factors A_n have the values reported in **Table 6**

Table 6 Second order polynomial fit coefficients from **Eq. (6)** with respective standard errors.

A_0	1.4 ± 0.03
A_1	$-2.1 \cdot 10^{-2} \pm 3 \cdot 10^{-3}$
A_2	$1.6 \cdot 10^{-4} \pm 6 \cdot 10^{-5}$

The polynomial fit provided an R-squared value of 0.9974.

Error bars of the plot represent minima and maxima measured intensities at each temperature for heating or cooling cycle. The resolution of the measurements (2.4%) was calculated from the error bars, equivalent to 0.6°C at the normalization temperature of 25°C.

3. Integration of cryofixation with live imaging

After calibrating the temperature, nematodes injected in the microfluidic device were able to bend and move across the channel, proving the compatibility of this version of the microfluidic device with live imaging microscopy (**Figure 26**, left panel). Continuous imaging of the sample allows recording of the cryofixation event with time resolution only limited by the exposure time of the camera (**Figure 26**, right panel).

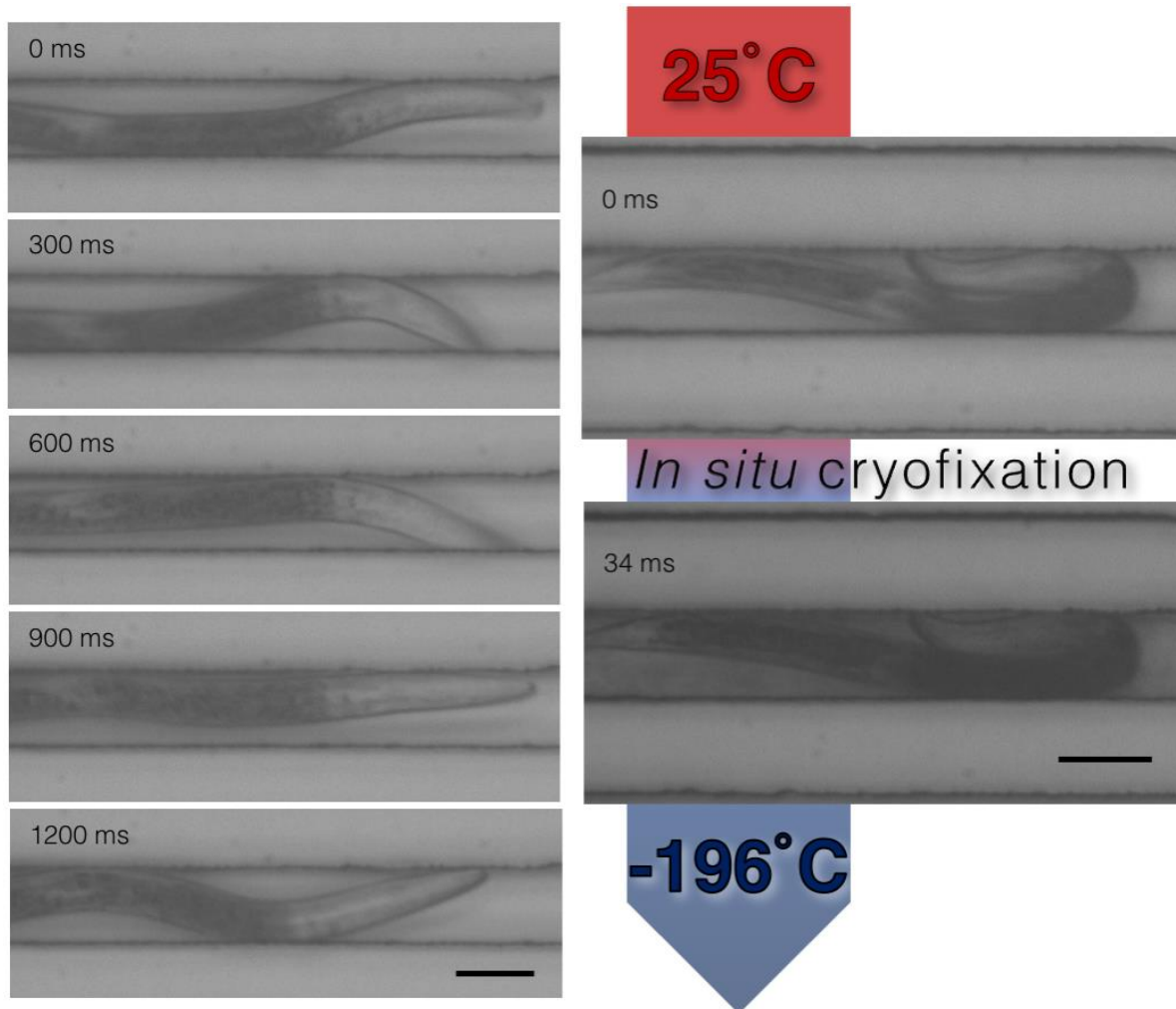


Figure 26 Integration of live imaging with in situ cryofixation. Left panel: live imaging in the microfluidic system for cryofixation shows the bending of *C. elegans*. Nematode bending was used in the cryofixation experiments as confirmation that the temperature of the microfluidic channel was suitable for *C. elegans* and therefore the calibration of the resistive heater was successful. Right panel: in situ cryofixation of *C. elegans* in brightfield mode. Observation of the sample is uninterrupted during fixation and only limited by the acquisition framerate. Scale bars measure 30 μm .

4. Extent of ice formation analyzed by brightfield and DIC microscopy

The appearance of a frozen sample in light microscopy dramatically changes depending on whether the freezing event occurred rapidly (\sim ms) or slowly (\sim s) (**Figure 27**).

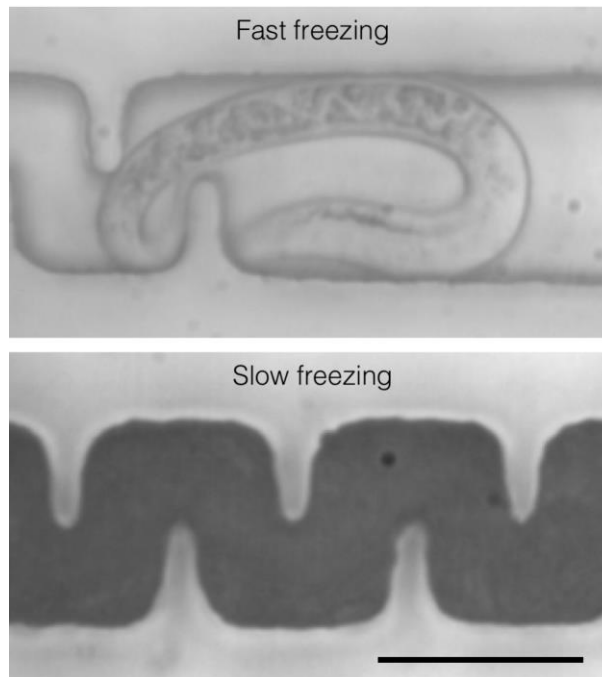


Figure 27 Comparison of image quality for fast frozen and slow frozen samples in brightfield microscopy. In the fast frozen sample, features are well defined as before freezing. In the slow frozen sample, channel content appears completely dark since ice crystals scatter the light, dramatically degrading the image quality. Scale bar measures 30 μ m.

Fast frozen samples appear clear and *C. elegans* features are visible as in live imaging. Slow frozen samples appear completely dark in brightfield microscopy because ice crystals scatter the light, considerably degrading the image quality.

In brightfield microscopy, an overall darkening of the FOV was observed upon cryofixation (cf. **Figure 26**, right panel). To investigate whether this sudden darkening of the sample is due to ice crystallization or not, the gray values of different regions of interest across the FOV were measured over time. Cryofixation was triggered at the 1000 ms time point from the start of the video (**Figure 28**).

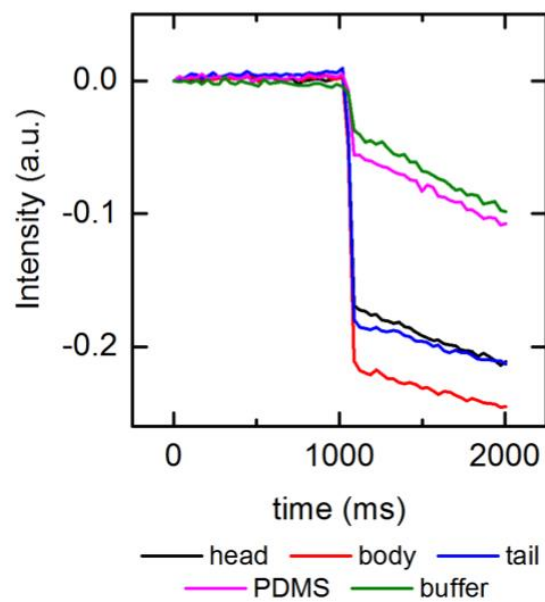
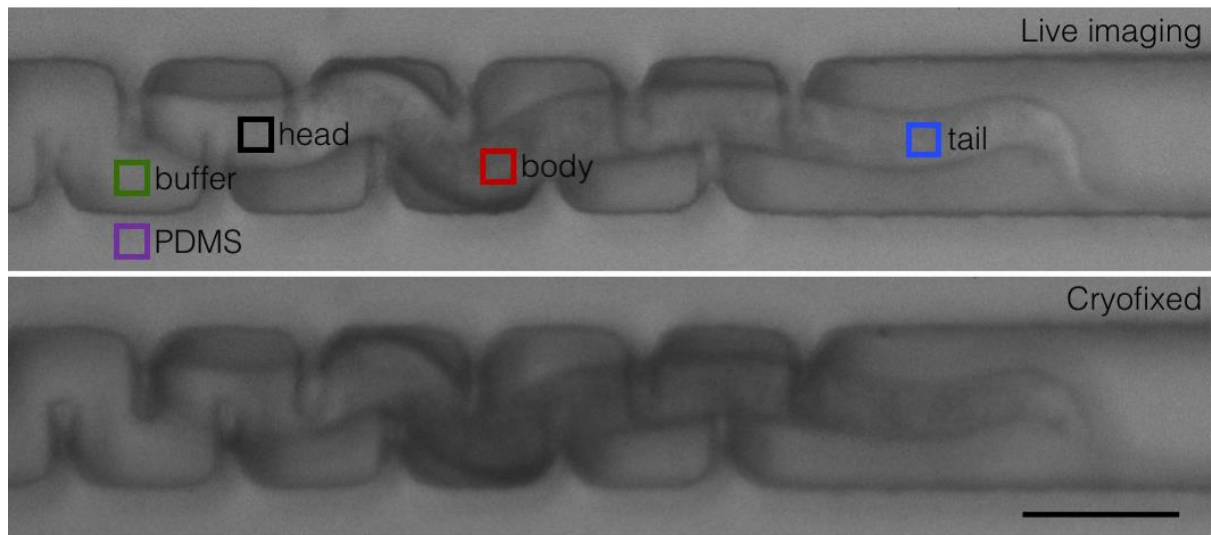


Figure 28 Measurement of the image intensity during cryofixation recorded in brightfield microscopy. Cryofixation was triggered at the 1000 ms timestamp. Measurements revealed that the change in intensity upon cryofixation was different for different zones of the nematode. The zone with the strongest decrease was the body region of the nematode, equivalent to 80% of the intensity before freezing. Because of the region-specific difference in intensity, the formation of ice cannot be excluded. For the acquisition of the video, a 10x/0.2 NA air objective with a 14.3 mm working distance was used. For the data recording, an Andor Neo sCMOS camera at 34 ms exposure time was used. Raw data provided by Marie Fuest, PhD and Rodrigo Galilea Kleinstauber. Scale bar measures 30 μm .

Regions of interest were divided in worm sections (head, body, tail), PDMS channel wall and channel content outside the worm outline (buffer). For the normalization of the ROI intensities, the following equation was used:

$$\bar{I}_{ROI}(t) = \frac{I_{ROI}(t) - I_{ROI}(0)}{I_{ROI}(0)} \quad (7)$$

Where $\bar{I}_{ROI}(t)$ is the normalized intensity of one ROI over time, $I_{ROI}(t)$ is the measured intensity of the ROI over time and $I_{ROI}(0)$ is the first value of intensity that was measured in the acquisition of the ROI.

The measurement confirmed that the nematode decreased in intensity more strongly than the PDMS channel walls and the buffer solution. The strongest decrease was measured in the ROI relative to the center part of the worm body, equivalent to 80% of the value before freezing.

Different parts of the nematode (i.e. head, body, tail) showed different decreases in intensity. This indicates that the measurement is not relative to a surface phenomenon (e.g. reflection of the light on the PDMS) but it is indeed specific to sample regions. It cannot be excluded, therefore, the formation of ice upon freezing. However, the decrease in intensity of parts of the sample lacking in water (i.e. PDMS) might indicate a contribution to the darkening by the change in the refractive index over the large temperature change.

To highlight the possible ice crystal growth during the first milliseconds of the cryofixation event, a framerate of 100 fps and differential interference contrast (DIC) were used (**Figure 29**). Ice crystals and liquid water have a difference in refractive index of $\sim 10^{-2}$ (1.310 and 1.333, respectively) [Hale and Querry, 1973; Warren, 1984]. DIC microscopy highlights small differences in refractive index, achieving higher contrast compared to classical brightfield illumination without requiring sample staining [Stephens and Allan, 2003].

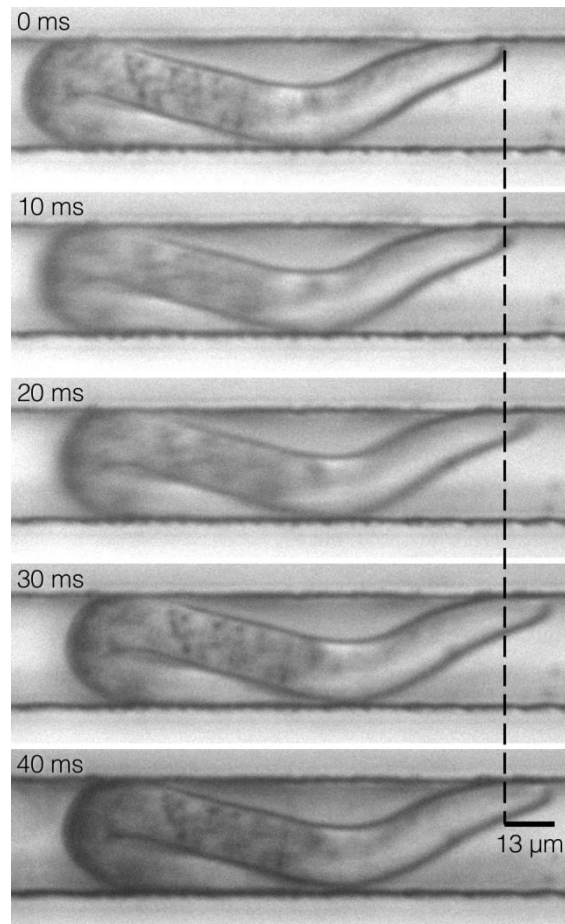


Figure 29 Cryofixation of *C. elegans* recorded at 100 fps in DIC microscopy. Frames around the cryofixation event show the translation of the nematode along the microfluidic channel. The translation is believed to be caused by an uneven thermal contraction of the microfluidic channel upon freezing. Timestamps are arbitrary and not synchronized with the freezing event. For the acquisition of the video, a 10 \times /0.2 NA air objective with a 14.3 mm working distance was used. For the data recording, an Andor Neo sCMOS camera at 10 ms exposure time was used. Modified from [Fuest and Nocera et al., 2018].

In **Figure 29**, frames around the cryofixation event are showed. Timestamps in the upper left corner of each frame are arbitrary and not relative to the freezing event that was not synchronized to the video recording. Between 0 and 30 ms, the worm translated along the channel from left to right by about 13 μ m. The specimen did not change conformation in the translation, excluding that the movement was due to nematode motility. This sudden movement was likely caused by a pressure gradient across the channel linked to the freezing event. The specimen stopped translating at the 40 ms timestamp and no further changes in the worm position were observed.

The video recorded in DIC microscopy was analyzed as previously done for the brightfield acquisition, plotting the normalized intensity of the different ROIs over the experiment time.

Normalization was computed as reported in Eq. (7). In **Figure 30**, the normalized intensities of the ROIs are reported.

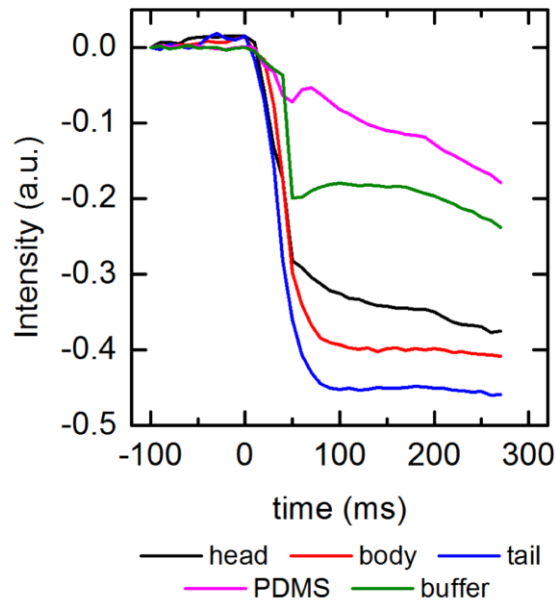


Figure 30 Measurement of the image intensity during cryofixation recorded in DIC microscopy. The measurement confirmed a stronger decrease in intensity for the nematode than for the rest of the FOV. Time axis is consistent with **Figure 29**.

Similar to the acquisition in brightfield microscopy, DIC microscopy confirmed a stronger darkening within the nematode regions.

Upon cryofixation, brightfield microscopy and DIC microscopy both detected a decrease in the nematode intensity compared to the rest of the FOV. However, using light microscopy it was not possible to assess whether the darkening was related to the light scattering by the ice crystals or the change in refractive index due to the change in temperature.

Chapter 4

Cryofluorescence microscopy of *Caenorhabditis elegans* prepared by microfluidic cryofixation

Cryogenic temperatures arrest the diffusion of molecular species. In fluorescence microscopy, this is advantageous for preventing photobleaching of samples. In addition, quantum yield of fluorescent molecules generally increases at cryogenic temperature, allowing the collection of higher signals. However, due to the stabilization of dark states at low temperature, it is not clear whether cryofixation would eventually preserve the signal of fluorescent markers. The release of calcium ions is a ubiquitous trigger for cell signaling cascades. Fusing green fluorescent protein (GFP) to calcium-binding proteins, it is possible to image the signaling cascades where they propagate. The HBR4: *goIs3[pmyo-3::GCaMP3.35::unc-54-3'utr, unc-119(+)]* *C. elegans* strain expresses the calcium indicator GCaMP3.35 in the muscle fibers. During muscle contraction, the free intracellular calcium concentration increases, calcium ions bind to GCaMP molecules increasing the brightness of the contracted muscle fibers [Schwarz, Spies and Bringmann, 2012]. The increase of the GCaMP fluorescence has kinetics in the 100 ms range [Tian *et al.*, 2009]. The microfluidic system for cryofixation was used here to study the cryogenic preservation of the fluorescent calcium signaling event with high time resolution.

Immersion objectives can achieve higher NAs than air objectives. The result is a higher spatial resolution of the acquired images. The microfluidic device for cryofixation imposes the use of air objective, limiting the image resolution that can be achieved. The limitation can be bypassed by transferring the sample to other microscopy setups with better optics. Here, the setup used by Faoro *et al.* was modified to accommodate the microfluidic chip and allow confocal microscopy at higher NA on cryofixed *C. elegans*. To prevent frost build-up on the cold surfaces and sample thawing, the samples needed to be kept in a dry environment below the glass transition temperature of water throughout the handling, transfer and imaging steps. In this chapter, a workflow for the transfer and imaging of cryofixed samples in immersion cryo-microscopy is presented. Subsequently, the gain in contrast moving from widefield microscopy to immersion cryo-confocal microscopy is reported.

The immersion cryo-microscopy setup was equipped with a benchtop STED module. STED microscopy uses powerful lasers to image samples with sub-diffraction resolution. The preservation of samples at cryogenic temperature would be beneficial for imaging without loss of signal by photobleaching. Here, the stability of the fluorescent compounds of the GCaMP strain of *C. elegans* under different illumination conditions are shown.

1. Cryofixation preserves GCaMP fluorescence

The muscle fibers of the *C. elegans* strain used in this experiment increase in fluorescence intensity upon contraction, as visible along the inner parts of the curved body (**Figure 31**, left panel). An important question in cryo-light microscopy is to what extent the fluorescence of target molecules (here GCaMP) can be preserved by cryofixation. Dark states of fluorescent molecules are more stable at low temperature [Moerner and Orrit, 1999]. The gained stability of the dark states might result in a dimmer signal in fluorescence cryo-microscopy compared to regular fluorescence microscopy. Here, the preservation of fluorescent signals after cryofixation is shown. In cryo-microscopy, it was possible to see how the curved parts of the nematode, where muscle fibers were contracting, were brighter than parts that were not contracting. For instance, the upper part of the head presented almost no contrast compared to the background whereas a clear fluorescence signal was observed in the lower part that was contracting in the moment of the freezing (**Figure 31**, right panel).

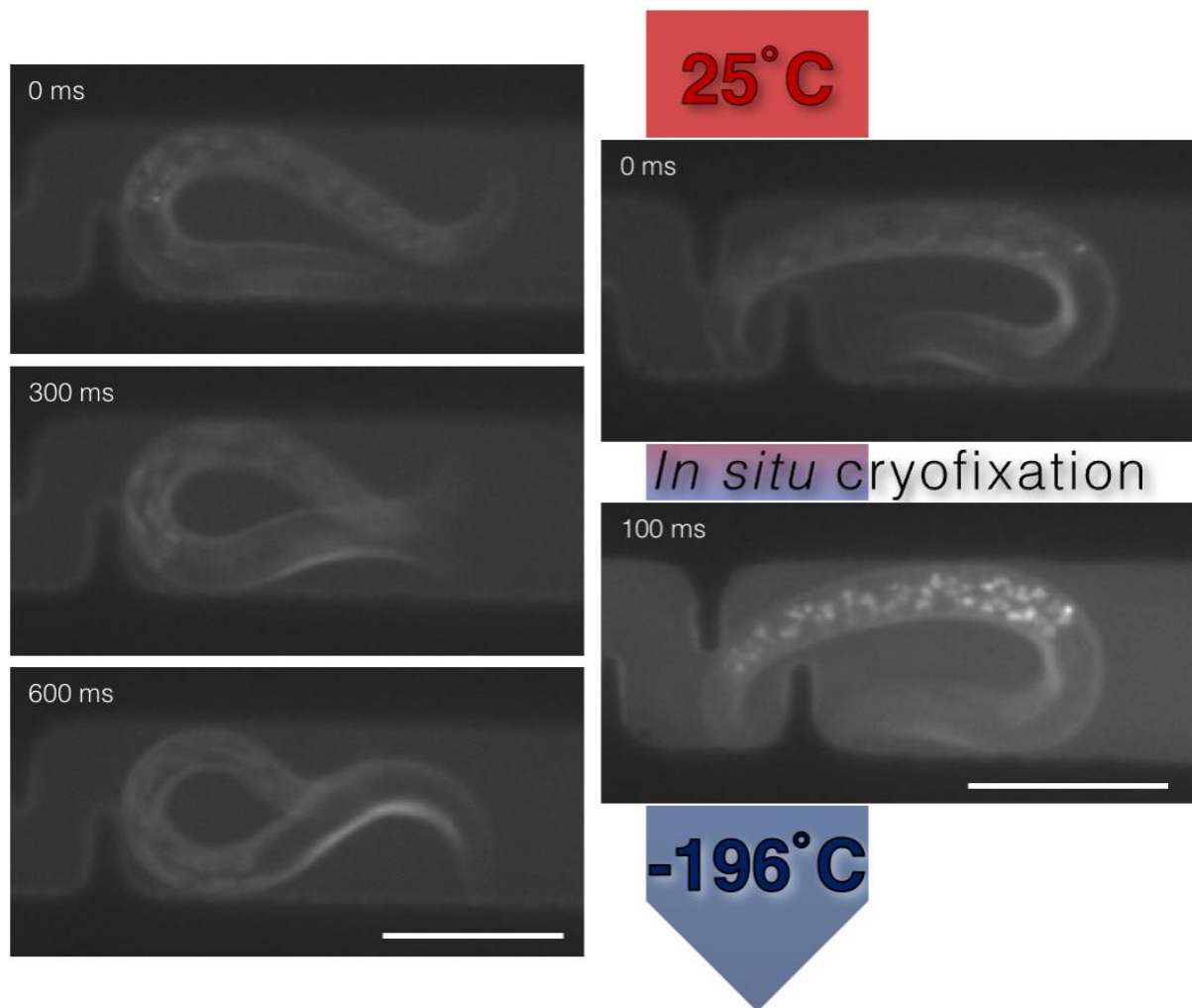


Figure 31 Integration of live imaging with in situ cryofixation. Left panel: frames from the live imaging in fluorescence microscopy of a *C. elegans* bending before in situ cryofixation. Fluorescence signal comes from GFP (sides of the body) and gut granule autofluorescence. The genetic strain used here expresses GCaMP in the muscle fibers. When contracted, muscle fibers are brighter than the rest of the body. The inner part of the nematode body becomes brighter the more is contracted over time (0 – 600 ms). Right panel: frames before (top) and after (bottom) cryofixation of a *C. elegans* during body bending, imaged in fluorescence microscopy. Fluorescence signal is preserved by the cryofixation and not reduced by dark states that are usually more stable at low temperature. *C. elegans* were suspended in M9 buffer with 10% (m/m) trehalose added as cryoprotectant. Imaging was performed using a 20x/0.40 NA air objective with 3.9 mm working distance. The microscope was equipped with a 480/40 nm excitation filter and 510 nm long pass emission filter. Images were acquired using an Andor Neo sCMOS camera with an exposure time of 100 ms and a rate of 10 frames per second. A Nikon IntensiLight mercury lamp was used as the excitation source. Scale bars measure 30 μm . Modified from [Fuest and Nocera et al., 2018].

Once the sample is cryofixed, time constraints disappear. Removing time limitations, it is possible to acquire images of the transient event using exposure times longer than the duration of the event observed. As shown in the left panel of **Figure 31**, typical body bends have a duration on the order of hundreds of milliseconds. Here, this sub-second event was reconstructed in its volume using a total exposure time of 2.6 seconds (**Figure 32**).

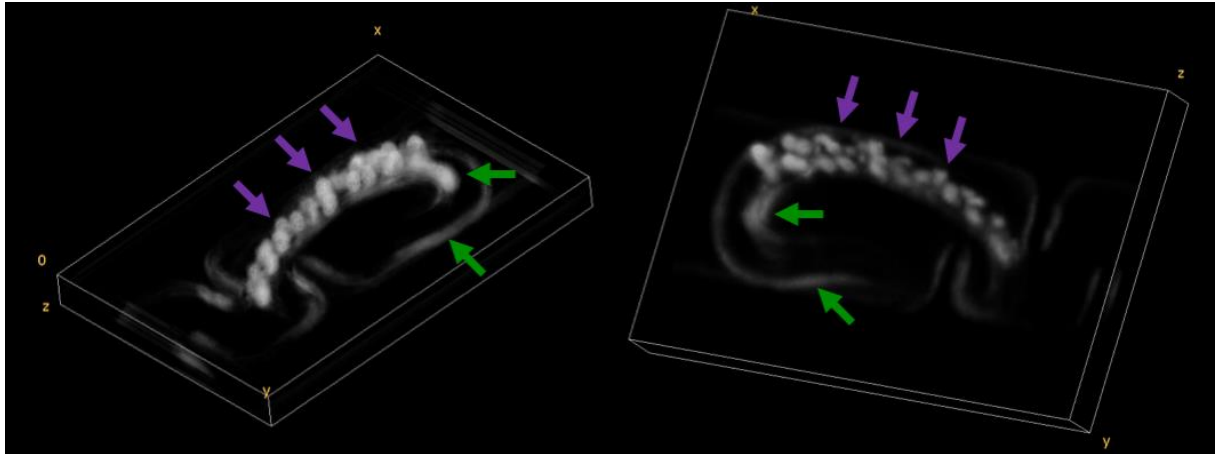


Figure 32 Volume reconstruction of a *C. elegans* cryofixed in a microfluidic channel. Fluorescence signal comes from GFP (green arrows) and gut granule autofluorescence (purple arrows). Once cryofixed, a transient event can be imaged with a total exposure time longer than its duration. Top view of the nematode (left) and bottom view of the same sample (right). The volume was reconstructed using Fiji software [Schindelin et al., 2012]. A z -stack of 26 wide-field images was taken with $1\ \mu\text{m}$ between slices. Each image was acquired at 100 ms exposure time. Images of the z -stack were registered on the xy -plane using StackReg plugin [Thevenaz, Ruttimann and Unser, 1998] to compensate vibrations of the setup and improve the final image quality. Images were successively deconvoluted to remove out-of-focus light [ImageJ.net, 2017]. Modified from [Fuest and Nocera et al., 2018].

Despite the low numerical aperture of the air objective in use (20x/0.4NA), it was possible to reconstruct the gut granules as separate objects (purple arrows) and the contracted muscle fibers in the inner part of the bent body (green arrows) (**Figure 32**).

Video acquisition of *C. elegans* cryofixation in fluorescence microscopy (**Figure 31**, right panel) was analyzed to study the effects of cryofixation on GCaMP and gut granules. Although the cryofixation was not synchronized to the video, the transition between live imaging and cryomicroscopy was easily recognizable because of the low time resolution of this particular acquisition. In fact, the time resolution was limited by the long exposure time (100 ms) required for the accumulation of a strong enough signal.

The analysis of the video showed two different behaviors for the two fluorescent parts of the sample. Upon cryofixation, the fluorescence intensity of the gut granules increased 2-fold whereas GCaMP intensity remained constant (**Figure 33**).

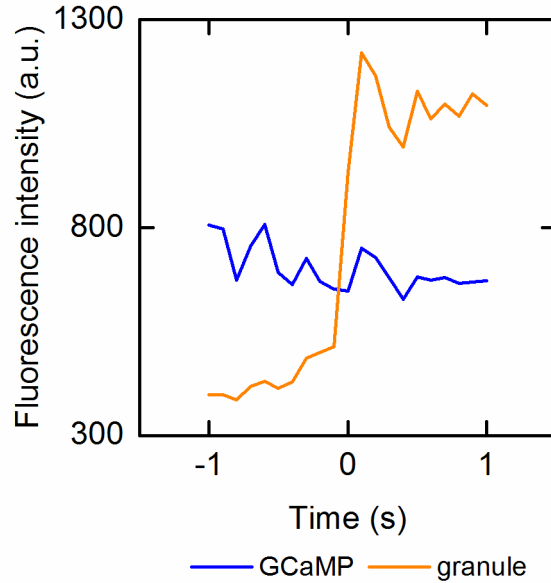


Figure 33 Fluorescence intensity measurement over the cryofixation event. GCaMP intensity remained constant upon cryofixation whereas gut granule intensity increased 2-fold. Frames of the recorded video were registered over the xy -plane to minimize measurement errors due to setup vibrations. For this operation, the plugin StackReg was used [Thevenaz, Rüttimann and Unser, 1998]. Mean values of intensities of the contracted muscles were measured over a region of interest (ROI) to trace the GCaMP intensity. The same was done for the gut granule auto-fluorescence intensity. Freezing was not synchronized with the video acquisition.

A combination of mechanisms may explain the observed increase in fluorescence of the gut granules. Gut granules are lipid vesicles whose molecular composition and function in the *C. elegans* physiology are still a matter of debate in the community. Emitting in a broad range of wavelengths ranging from blue to orange, it is likely that this auto-fluorescence does not arise from one single chemical species but rather from a mixture of small aromatic compounds. For instance, the anthranilic acid glucosyl ester (AAGE) is believed to be responsible for the granule emission in the blue region of the spectrum and compounds from the lipofuscin family are considered to be the source of the auto-fluorescence in the orange region of the spectrum [Clokey and Jacobson, 1986; Coburn *et al.*, 2013]. The dim signal observed at room temperature on the green-red side of the spectrum, strongly increased in intensity upon cryofixation. This behavior might be explained via two different mechanisms or a combination of them. First, the rigidity of their molecular structure makes aromatic fluorescent molecules have the tendency to increase their quantum yield with the decrease in temperature [Berezin and Achilefu, 2010]. This is probably due to the more restricted non-radiative pathways that are available to these molecules to dissipate the energy of their excited electronic state (**Figure 1**). A second hypothesis for the intensity increase upon cryofixation is the redshift of the blue emitting compounds. With this hypothesis, the change in intensity would not actually be an increase of the overall intensity

but rather a shift of the emission to longer wavelengths of the spectrum. Unfortunately, it was not possible to test these hypotheses with the microscopy apparatus used in this work. To acquire information on the physico-chemical nature of fluorescent molecules (electronic and vibrational states), it is necessary to couple a spectrophotometer to the microscopy setup.

To explain the stability of GCaMP fluorescence intensity over the cryofixation event, the same reasoning can be applied. GCaMP is a fusion protein of GFP with the calcium-binding protein calmodulin. The most stable conformation of GCaMP is an unfolded conformation when calcium ions are not present in solution. In the unfolded state, the fluorescent center of GFP is exposed to water molecules that quench its fluorescence. When calmodulin binds calcium ions that are present in solution, the most stable conformation of GCaMP has GFP in its quasi-native state, resulting in an increase in quantum yield [Wang *et al.*, 2008; Akerboom *et al.*, 2012]. Although the basic structure of the fluorophore at the core of GFP is also an aromatic ring, there is a substantial difference between GFP and AAGE. In the case of GFP, the fluorescent center is covalently bound to the long peptide chain forming the backbone of the protein structure (238 amino acids, 26.9 kDa). The anthranilic acid, on the other hand, is bound to a glucose molecule (0.18 kDa) (**Figure 34**).

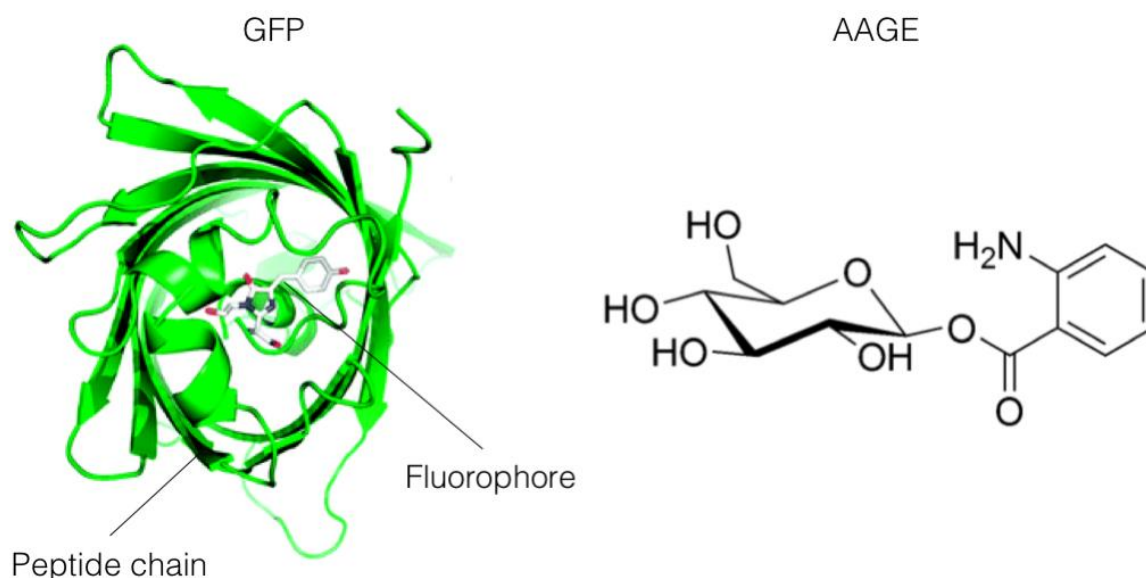


Figure 34 Molecular structure of the fluorescent species present in the cryofixed *C. elegans*. GFP and AAGE both have a small aromatic molecule as the emitting center. The long peptide chain of GFP is believed to prevent fully-radiative dissipation mechanisms at cryogenic temperature. GFP structure adapted from [Van Thor, 2009], AAGE structure adapted from [Coburn et al., 2013].

The protein structure around the fluorophore might indeed act as a protective cage. Creating a closed chemical environment, the emitting center of GFP might be less sensitive than AAGE to changes in the surrounding medium (e.g. solvation, conformational changes).

2. Immersion microscopy at cryogenic temperature

Here, *in situ* cryofixed *C. elegans* were imaged in confocal microscopy at about -145°C, using a high-NA immersion objective (63x/1.15 NA) that can work below the glass transition temperature of water (-137°C). The results of these experiments show that the transfer process faithfully preserves the shape of the sample and enables the acquisition of cryofluorescence images with significantly improved contrast and resolution. Cryofixed samples were provided by Marie Fuest, PhD and Rodrigo Galilea Kleinsteuber. Data in cryo-immersion were acquired in collaboration with Margherita Bassu, PhD.

2.1. *C. elegans* shape is preserved after sample transfer

Removing the sample from the microfluidic cryofixation system poses the risk of recrystallization or mechanical damage. Here, channel features (walls, traps) were used as fiducial markers to assess whether the sample transfer damaged the sample quality. The channel features from the cryofixation frame and in confocal immersion cryo-microscopy were superimposed to compare the shape of the nematode before and after the transfer step (**Figure 35**).

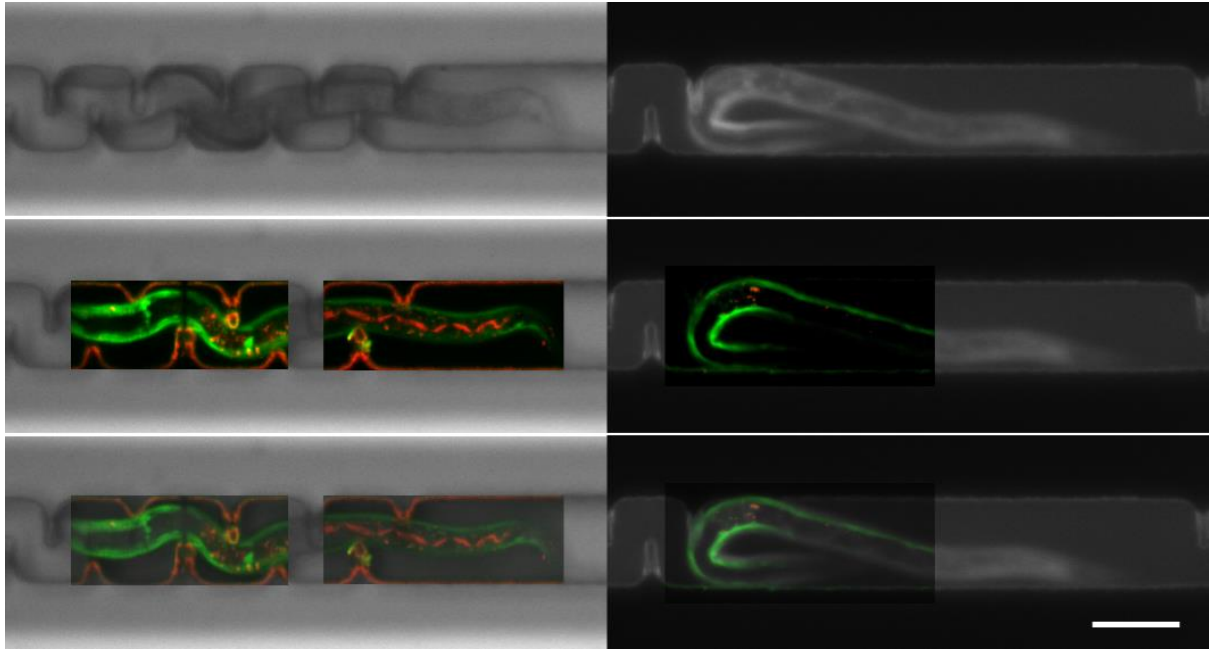


Figure 35 Overlay of the nematodes before and after transfer (cryofixation frame and immersion cryo-microscopy). The superposition of the channel features showed good alignment of the nematode body, indication of good preservation of the sample throughout the transfer steps. Cryofixed samples were provided by Marie Fuest, PhD and Rodrigo Galilea Kleinstaubler. Data in cryo-immersion was acquired in collaboration with Margherita Bassu, PhD. Scale bar measures 30 μm .

From the absence of changes in the shape of the nematodes, the preservation quality of the samples was evaluated to be good with no detectable damage.

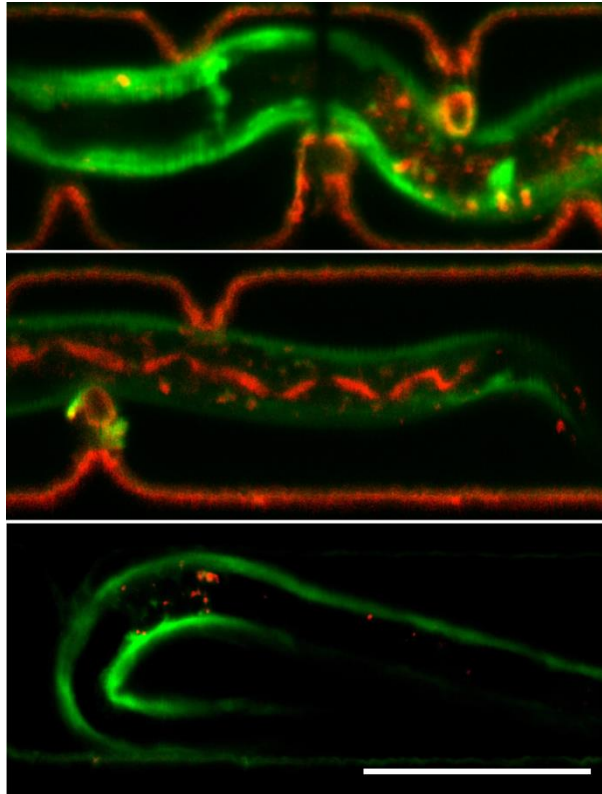


Figure 36 *C. elegans* cryofixed in the microfluidic channel and imaged in confocal microscopy at $\sim -145^{\circ}\text{C}$ using a cryoimmersion objective (63x/1.15 NA). Green, GCaMP; red, gut granules. Cryofixed samples were provided by Marie Fuest, PhD and Rodrigo Galilea Kleinstenber. Data in cryo-immersion was acquired in collaboration with Margherita Bassu, PhD. Scale bar measures 30 μm .

As observed in live imaging and low-NA cryo-microscopy, two fluorescent objects are visible in the sample: the muscle fibers (green channel) and the autofluorescent gut granules (red channel).

Acquiring multiple FOVs, it was possible to reconstruct the nematode body. From the relative brightness of the image, it was also possible to see which muscles were contracting in the moment of freezing. Indeed, the increase in calcium concentration that triggers the muscle contraction also makes the GCaMP molecules more fluorescent [Tian *et al.*, 2009] (**Figure 37**, green arrows).

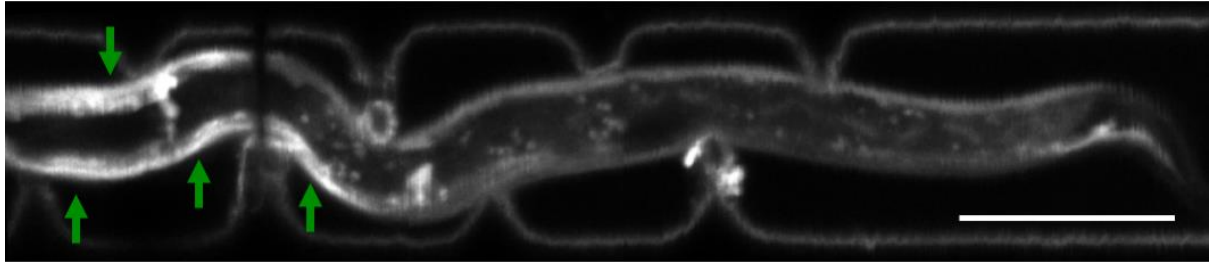


Figure 37 Reconstruction of nematode body stitching three FOVs acquired in fluorescence immersion cryo-microscopy. Fluorescence signal comes from GCaMP molecules expressed in the muscle fibers and from autofluorescent gut granules. Brighter muscle fibers (arrows) are associated with more contraction at the moment of fixation. Cryofixed sample was provided by Marie Fuest, PhD and Rodrigo Galilea Kleinsteinber. Data in cryo-immersion was acquired in collaboration with Margherita Bassu, PhD. Scale bar measures 30 μm .

2.2. Image quality in confocal cryoimmersion microscopy

As previously introduced, the low numerical aperture of the optics of the cryofixation device limits the achievable image quality. Here, a significant improvement in image quality was attained by transferring the sample to a confocal cryoimmersion microscope.

Although kept under liquid nitrogen until moved to a dry cryogenic environment for imaging, samples showed frost build up, in particular near the channel outline (**Figure 38**). The image quality observed with the air objective deteriorated due to frost formation. However, this was alleviated once the sample was observed in immersion cryo-microscopy. The lack of detection of frost in immersion cryo-microscopy was probably due to the matching of the refractive index of the immersion fluid with the refractive index of the ice.

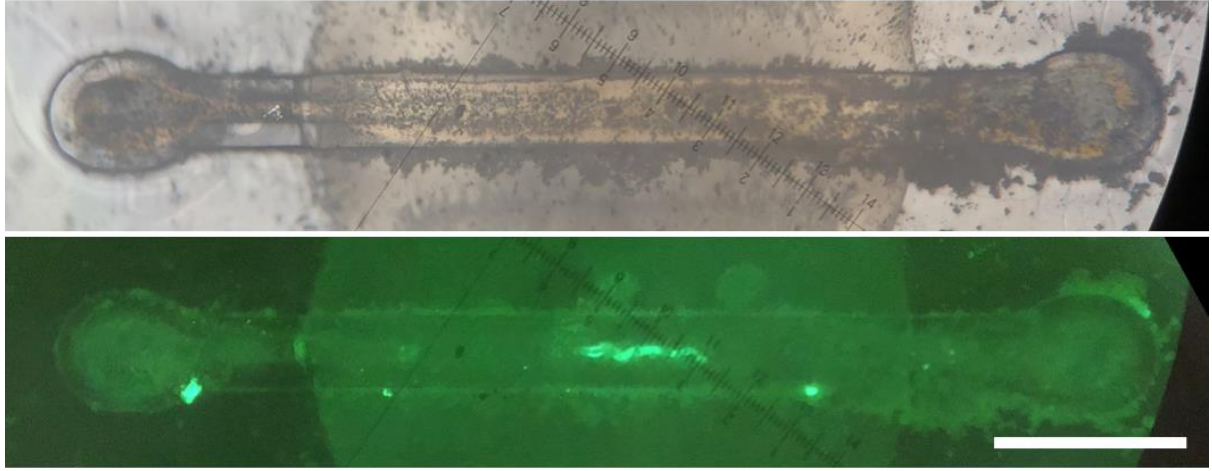


Figure 38 Microfluidic chip containing cryofixed *C. elegans* imaged in a dry cryogenic environment ($10\times/0.2$ NA). In fluorescence, it is possible to see the outline of the nematode in the middle of the microfluidic channel. Fluorescence signal comes from GCaMP and autofluorescent gut granules. The presence of frost, that prevents good imaging when an air objective is used, is alleviated likely by the matching of water refractive index in immersion cryo-microscopy. Scale bar measures $300\ \mu\text{m}$.

The gray values of a line traced across the nematode body were compared between the cryofixation frame and the immersion cryo-confocal image. Plotting the normalized values against the length of the line, the change in contrast was assessed. The normalized intensity along the traced line ($\bar{I}(x)$) was computed using the following equation:

$$\bar{I}(x) = \frac{I(x) - I_i}{I_{bg}} \quad (8)$$

Where I_i is the intensity measured in the middle of the nematode body and I_{bg} is the intensity of the background as schematized in **Figure 39**.

The contrast attained in confocal cryoimmersion microscopy was assessed to be about 20 times higher than in widefield microscopy (**Figure 39**).

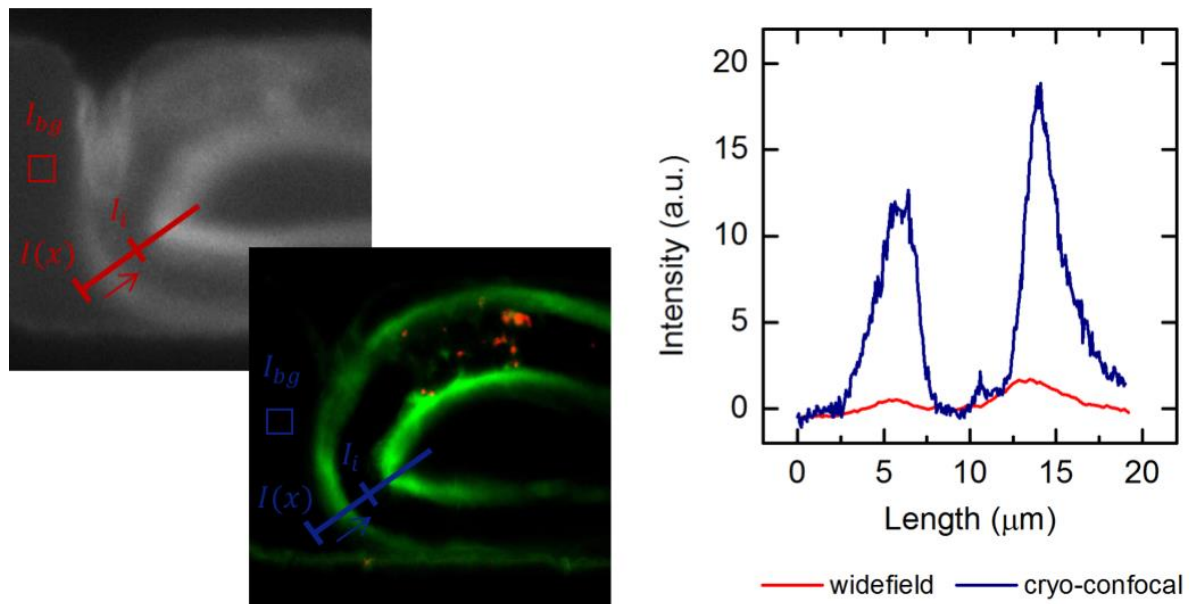


Figure 39 Measured intensity across nematode body in widefield and in confocal cryomicroscopy. In confocal cryomicroscopy, the contrast measured across the nematode body was about 20 times higher than in widefield microscopy. Data in cryo-immersion was acquired in collaboration with Margherita Bassu, PhD.

The two peaks in **Figure 39** appear to have different relative intensities and smaller full width at half maximum (FWHM) in cryo-confocal microscopy compared to widefield microscopy. However, these measurements can be biased by the uncertainty along the z-axes of the sample. In fact, due to the round shape of the nematode and its thickness, different image planes will have different relative intensities on the same region of interest.

For instance, in the right panel of **Figure 35** three consequences of this aspect can be remarked. First, the muscle groups of the head of the nematode, that appear strongly fluorescent in widefield, are not visible in cryo-confocal. Second, only few granules are visible in cryo-confocal whereas there seem to be many more in widefield. Third, the muscles seem to run in the inner part of the nematode body rather than on the edge, although perfectly following its contour. All three of these observations can be explained by the position of the image plane in the upper part of the nematode body rather than the middle plane.

3. STED effects on cryofixed GCaMP and gut granules

To characterize the stability of GCaMP and granules at cryo-temperature under different illuminating conditions, STED and confocal images of the same region were acquired at different values of STED laser power (15%, 50% and 100%) while excitation power was kept

constant at 100% power. Maximum power values of each laser are reported in **Table 5**. The result of the image analysis is shown in **Figure 40**.

Super-resolution imaging was not possible in this work due to restrictions of the setup:

- i. The STED laser wavelength used in this work was 775 nm, while the most suited for GFP is 575 nm [Willig *et al.*, 2006];
- ii. The axial chromatic aberration of the immersion objective could not be corrected with the STEDYCON;
- iii. The cryo-stage of the setup was not optimized for the study of fluorescence over long acquisition times (cf. Chapter 7, 2. Limitations of cryoimmersion setup).

Nonetheless, an initial characterization of GFP and gut granule intensities at cryogenic temperature for super-resolution applications (e.g. stabilization of dark states, photo-switching) was carried out because it was considered of scientific interest for the future development of the technique.

The intensity of the ROIs of muscles and gut granules was measured over the experiment time. Intensity was normalized using the following formula:

$$\bar{I}(\mathbf{t}) = \frac{I(\mathbf{t}) - I_{min}(\mathbf{t})}{I_{max}(\mathbf{t}) - I_{min}(\mathbf{t})} \quad (9)$$

Where $I(\mathbf{t})$ is the intensity of a selected ROI over the measurement time. Minima and maxima are relative to the intensities of a single dataset. The error bars represent the spread in the measurement over three datasets. The same normalization was computed for the intensity of the gut granules.

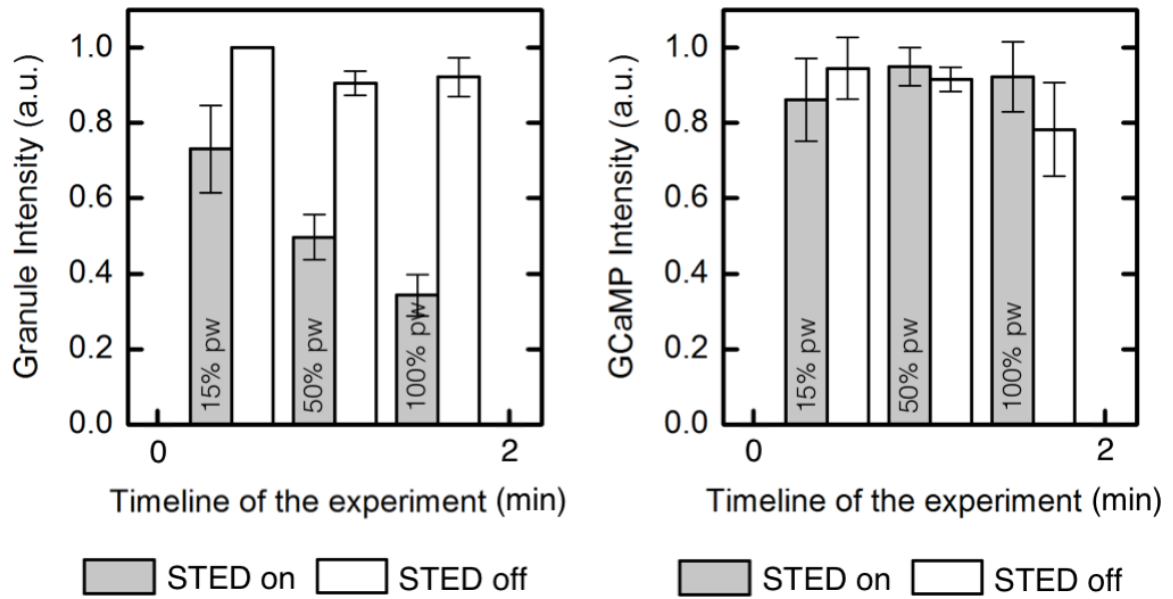


Figure 40 Normalized intensities of GCaMP and gut granules over the experiment time at increasing STED laser power. Data acquired at cryo-temperature ($\sim -145^\circ\text{C}$). Error bars represent the spread in value over 3 ROIs of the same FOV. Data acquired in collaboration with Margherita Bassu, PhD.

Gut granule intensity consistently decreased with the increase in STED power. Furthermore, the process was reversible for all STED powers (**Figure 40**, left panel). The intensity of GCaMP in confocal and in STED stayed the same within the error of the measurement for every value of STED laser power (**Figure 41**, right panel).

Interesting to remark was the effect of the temperature on the relative decrease in intensity of the gut granules. In fact, to reach about 50% decrease of intensity, 6% of STED laser power was required at room temperature (44 mW) whereas at cryo-temperature 50% of STED laser power (365 mW) was required.

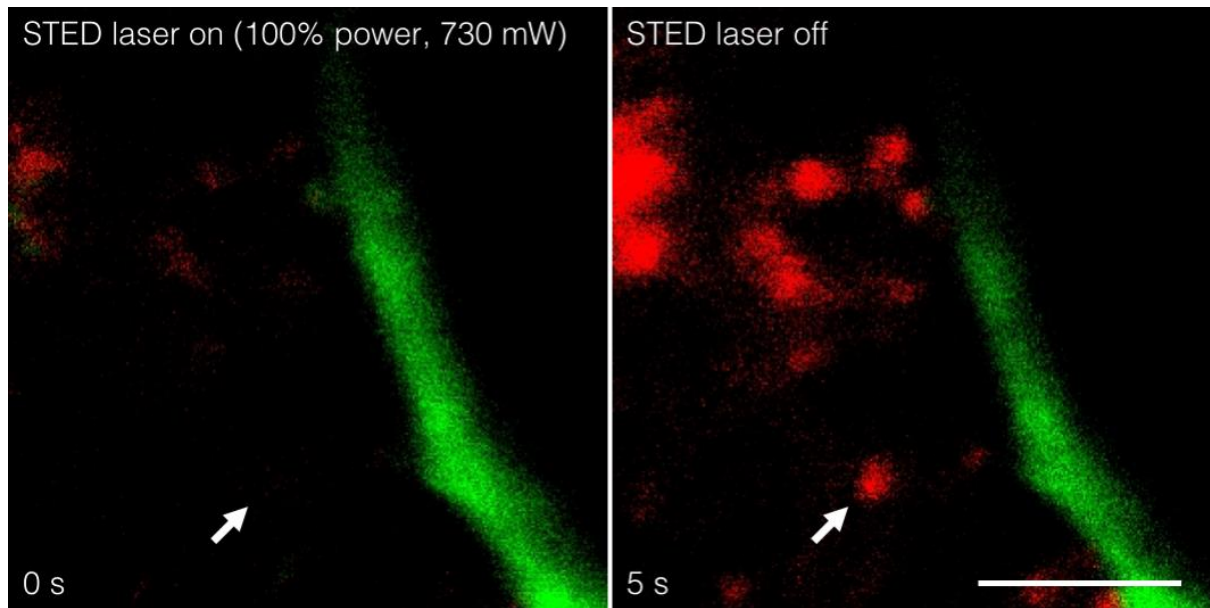


Figure 41 STED and confocal acquisitions of the same image in cryo-immersion confocal microscopy. Fluorescence signal coming from GCaMP (green channel) and autofluorescent gut granules (red channel). Gut granules are turned off by the STED laser in a reversible fashion (arrow). Excitation laser and STED laser were set at 100% of power. Data acquired in collaboration with Margherita Bassu, PhD. Scale bar measures 5 μm .

Cryogenic temperatures are advantageous for preventing photobleaching. Here, intensities of GCaMP at room temperature and at cryo-temperature under continuous exposure over time were compared (**Figure 42**).

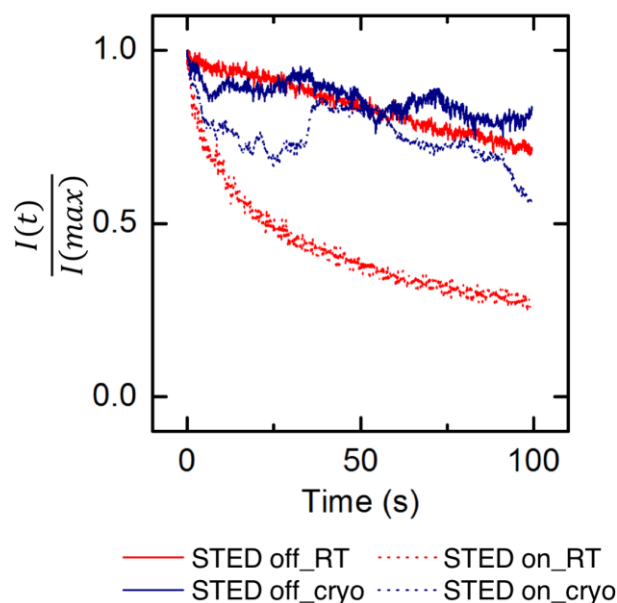


Figure 42 Intensity measurement of GCaMP at room temperature (red lines) and cryo-temperature (blue lines) over continuous exposure. Acquisitions were carried out with the STED laser turned off (continuous lines) and with the STED laser turned on (dotted lines). Cryogenic temperature prevents bleaching of GCaMP, resulting in a smaller decrease in intensity. The effect was stronger when the STED laser was turned on than otherwise. Excitation laser and STED laser were set at 100% of power. Data in cryo-immersion was acquired in collaboration with Margherita Bassu, PhD.

As expected, at room temperature bleaching with the STED on was faster than for confocal. At cryo-temperature, the overall decrease of intensity over time was less marked than at room temperature. Although the intensity decrease appeared faster with the STED laser on, quantitative estimations are difficult due to current limitations in the mechanical stability of the imaging cryo-stage (cf. Chapter 7, 2. Limitations of cryoimmersion setup). In fact, the noisy measurements at cryo-temperature are attributed to the vibrations propagated to the sample from the boiling liquid nitrogen in which the cryo-stage is submerged.

The high power of the STED laser is believed to be a risk for the re-crystallization of cryofixed samples [Wolff *et al.*, 2016]. In this work, no deterioration of the cryofixed samples was detected during an imaging time in the minute range. At the sub-cellular level, it would be interesting to assess the presence of ice damage by observing locations of the sample in EM that have already been imaged in cryo-STED.

Chapter 5

Electron microscopy of microfluidic cryofixed samples

Part of this chapter was published in “Cryofixation during live-imaging enables millisecond time-correlated light and electron microscopy” – M. Fuest*, G. M. Nocera*, M. M. Modena, D. Riedel, Y. X. Mejia, T. P. Burg *Journal of Microscopy*, **2018**.

The superior resolution of electron microscopy is of great utility to study biological systems. Whereas live imaging records information on the dynamics of a living system, electron microscopy is able to provide information of the inner structure of samples. Cryofixation offers the possibility of preserving the ultrastructure of cells without artifacts provided that ice crystallization can be suppressed. Here, a workflow combining light and electron microscopy was established and applied to study the quality of structural preservation in microfluidic cryofixation of *C. elegans* at nanometer resolution.

1. Cryofixed samples are not thawed during chip recovery

The device used in this work was designed to allow easy access to the cryofixed sample and enable the sample transfer. To recover the cryofixed sample, the assembly was moved from the shallow liquid nitrogen bath, where live imaging was performed, to a deeper liquid nitrogen bath to fully submerge it. Working under the liquid nitrogen level, the retaining ring was undone allowing the recovery of the microfluidic chip which was transferred in a vented vial for, if required, long term storage. During the transfer step, it is crucial to avoid any temperature increase above the glass transition temperature of water (-137°C). Working below this temperature, the stability of the cryofixed sample against recrystallization is insured. During the transfer procedure, moving the assembly from the microscope to the deeper liquid nitrogen bath is the step with the highest risk of recrystallization because the heat sink is no longer actively cooled by the liquid nitrogen.

To assess the extent of the available time before the sample crosses the threshold temperature, a heat sink was lifted from liquid nitrogen and the temperature at the cold post was measured until it increased above -137°C. Then, the time required to reach 25°C was linearly extrapolated

Figure 43.

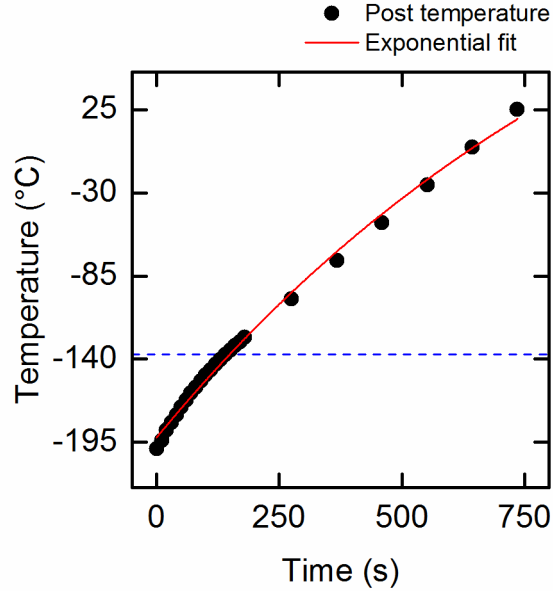


Figure 43 Temperature of a heat sink once removed from liquid nitrogen Temperature was measured until crossed the threshold value of the water glass transition temperature (-137°C, dashed line) and extrapolated to 25°C for the remaining time. From the measurement, the heat sink overcomes the threshold in about 2 minutes. Requiring about one second, the transfer of the assembly can be considered safe from recrystallization risk.

Data was fitted with an exponential curve of the form

$$T = C_0 + C_1 \cdot e^{C_2 \cdot t} \quad (10)$$

where T is the temperature of the post, t is the time and the factors C_n have the values reported in **Table 7**

Table 7 Exponential fit coefficients from **Eq. (10)** with respective standard errors.

C_0	233 ± 50
C_1	-425 ± 49
C_2	$-9 \cdot 10^{-4} \pm 1 \cdot 10^{-4}$

The exponential fit provided an R-squared value of 0.9957.

The measurements showed that the heat sink stays below the threshold temperature of -137°C for about 2 minutes after being removed from the liquid nitrogen bath. Transfer from the measurement bath to the recovery bath usually takes about one second. Consequently, the transfer step was considered free from re-crystallization risks.

2. Time-resolved light-electron microscopy workflow

To show the compatibility of microfluidic cryofixation with electron microscopy and address the quality of ultrastructure preservation, a complete light to electron microscopy workflow was carried out. The time resolution is in the millisecond range, up to 3 orders of magnitude better than the current state of the art (**Figure 44**).

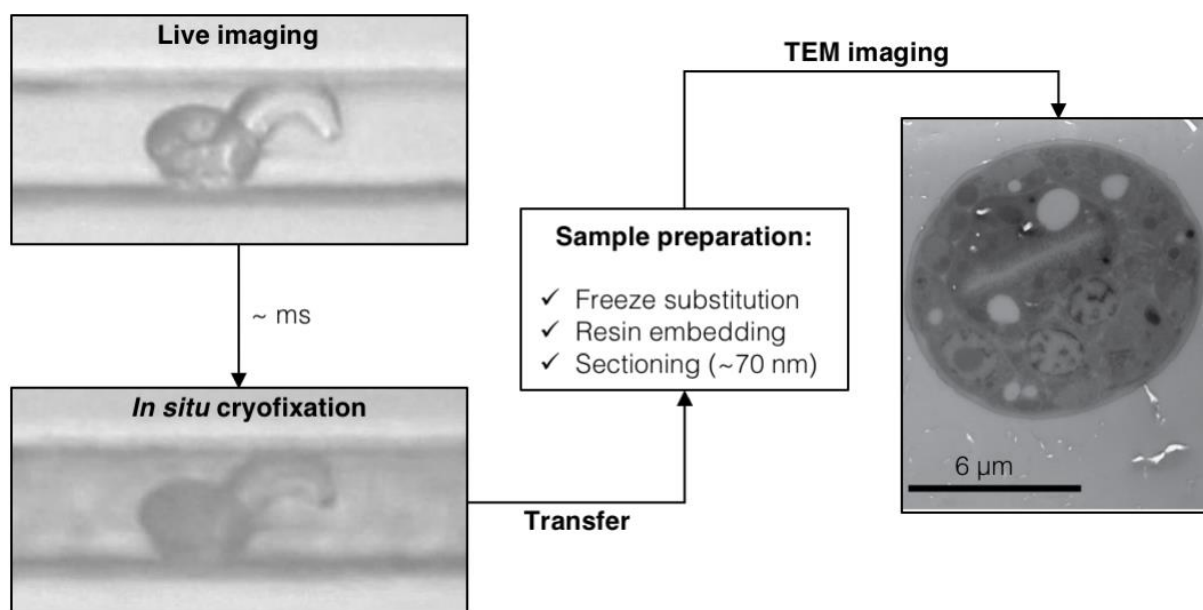


Figure 44 Light-electron microscopy workflow with millisecond time correlation. The specimen was live imaged and in situ cryofixed within millisecond. The microfluidic chip was then recovered from the cryofixation system and transferred for freeze substitution, resin embedding and thin sectioning. *C. elegans* sections were then imaged in TEM. Electron microscopy sample preparation and TEM imaging were performed by Dr. Dietmar Riedel (Facility for Transmission Electron Microscopy, MPI-BPC Göttingen). Modified from [Fuest and Nocera et al., 2018].

C. elegans was live imaged and cryofixed *in situ*. Imaging with room temperature EM requires the sample dehydration without deteriorating its ultrastructure (e.g. membranes, organelles). To warm the cryofixed sample up to room temperature while maintaining good preservation, freeze substitution was carried out. The sample was removed from the cryofixation device and, working under liquid nitrogen level, the ends of the channel were scored using a blade. Opening the sides of the channel was key to provide access to the chemicals for freeze substitution. Freeze substitution consists in a diffusion-limited chemical fixation starting at low temperature (-90°C) with stepwise warm up of the sample to room temperature. To prevent recrystallization and therefore ice damage, it is important to warm up the sample only once the water content is replaced with an organic solvent and a crosslinking chemical, usually acetone and formaldehyde,

respectively [Cavalier, Spehner and Humbel, 2009]. Contrary to high pressure frozen samples, samples cryofixed in a microfluidic channel only have the scored channel sides from which the diffusion of chemicals can take place. Despite the small accessible area ($\sim 900 \mu\text{m}^2$ per side over the ~ 1.5 mm of channel length), the microfluidic devices were found to be compatible with standard freeze substitution procedures. After freeze substitution, the sample was resin embedded, sectioned in thin slices (~ 70 nm) and imaged in transmission electron microscopy (TEM). Sample preparation and imaging for TEM were performed by Dr. Dietmar Riedel of the Facility for Transmission Electron Microscopy of the Max Planck Institute for Biophysical Chemistry in Göttingen.

In **Figure 45**, an overview of a *C. elegans* cross-section is shown. Labeling is provided to highlight some of the features of the nematode physiology.

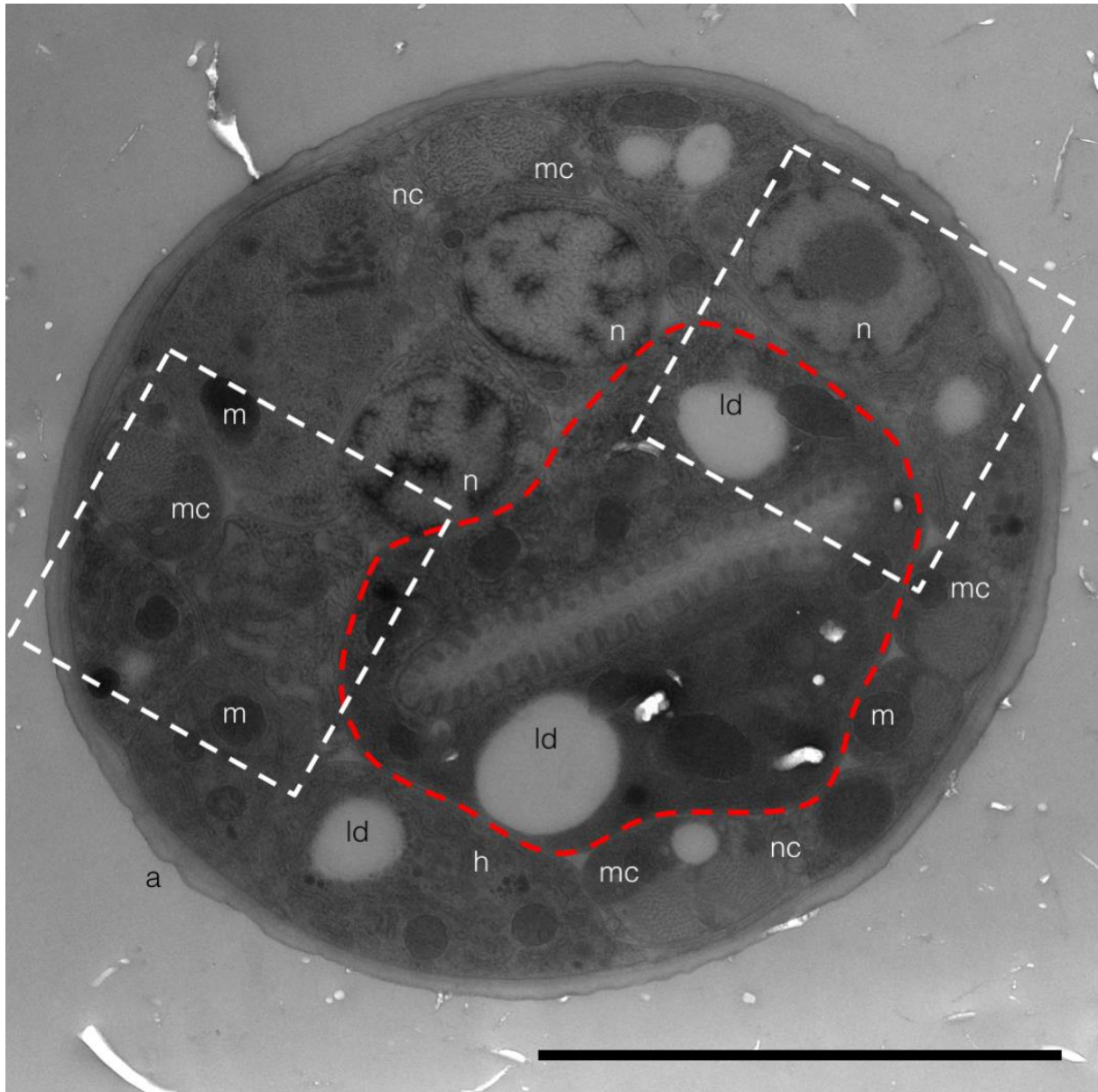


Figure 45 Overview of *C. elegans* section in transmission electron microscopy. The sample does not show major ice damage but only segregation patterns in the nuclei, characteristic of ice crystal damage. Ultrastructures (e.g. membranes, nuclear pores, cytoplasm) appear well preserved and free from voids. Red dashed line delineates the intestines. The meaning of labels are herein reported: n, nucleus; m, mitochondria; mc, muscle cells; ld, lipid droplets; h, hypodermis; nc, nerve cord; a, alae. Left and right white dashed regions are reported at higher magnification in **Figure 46** and **Figure 47**, respectively. Electron microscopy sample preparation and TEM imaging were performed by Dr. Dietmar Riedel (Facility for Transmission Electron Microscopy, MPI-BPC Göttingen). Scale bar measures 6 μm . Modified from [Fuest and Nocera et al., 2018].

3. Quality of the cryopreservation

Although freeze substitution also consists of crosslinking biomolecules to prevent their movements over time, there is a fundamental difference between chemical fixation at room temperature and cryofixation followed by freeze substitution. During chemical fixation,

biological processes are actively happening when the crosslinker is added to the medium to react with the sample. As explained in the Introduction, this can result in artifacts at the sub-cellular level. In freeze substitution, on the other hand, first the organic solvent diffuses throughout the sample and replaces the solid water. Then, the crosslinker is added to diffuse in every part of the sample. These steps are carried out at temperatures too low for starting biological activity and crosslinker polymerization (-90°C). After all water is replaced by the chemicals, the temperature is raised and all parts of the sample are synchronously chemically fixed, ideally, as they were at freezing [Dykstra, 1992].

C. elegans sections appear in transmission electron microscopy with well-defined features, indicating a good quality cryofixation. The sample is free from the voids characteristic of ice damage. From the higher magnification images (**Figure 46** and **Figure 47**), it is possible to observe well-preserved membranes and organelles (cuticle, mitochondria, hypodermis, nerve cords, alae).

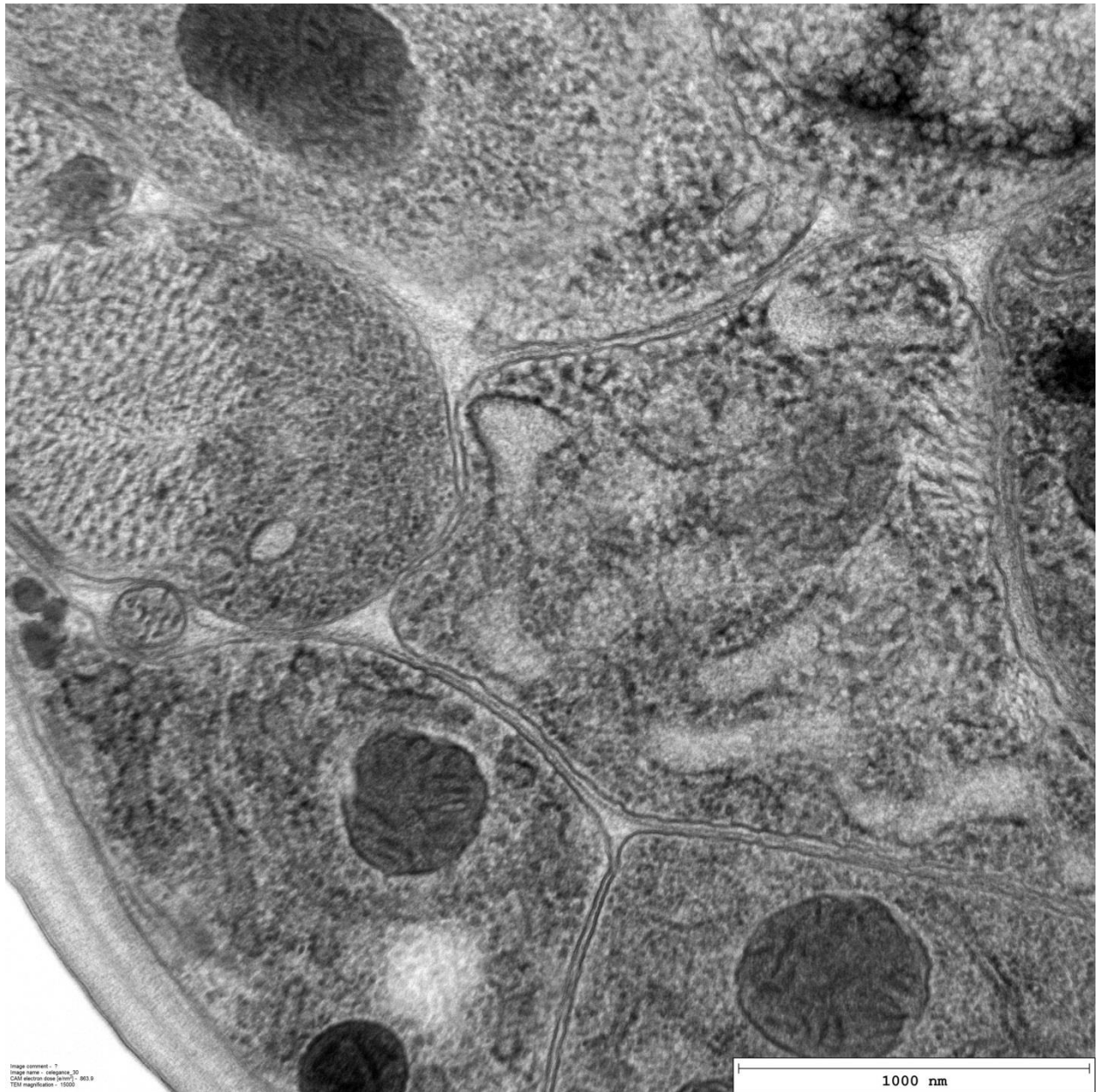


Figure 46 Higher magnification of the left white dashed region in **Figure 45**. Thin section of in situ cryofixed *C. elegans*. Membranes appear continuous and mitochondria appear well preserved, indicating the absence of ice damage. Electron microscopy sample preparation and TEM imaging were performed by Dr. Dietmar Riedel (Facility for Transmission Electron Microscopy, MPI-BPC Göttingen). Modified from [Fuest and Nocera et al., 2018].

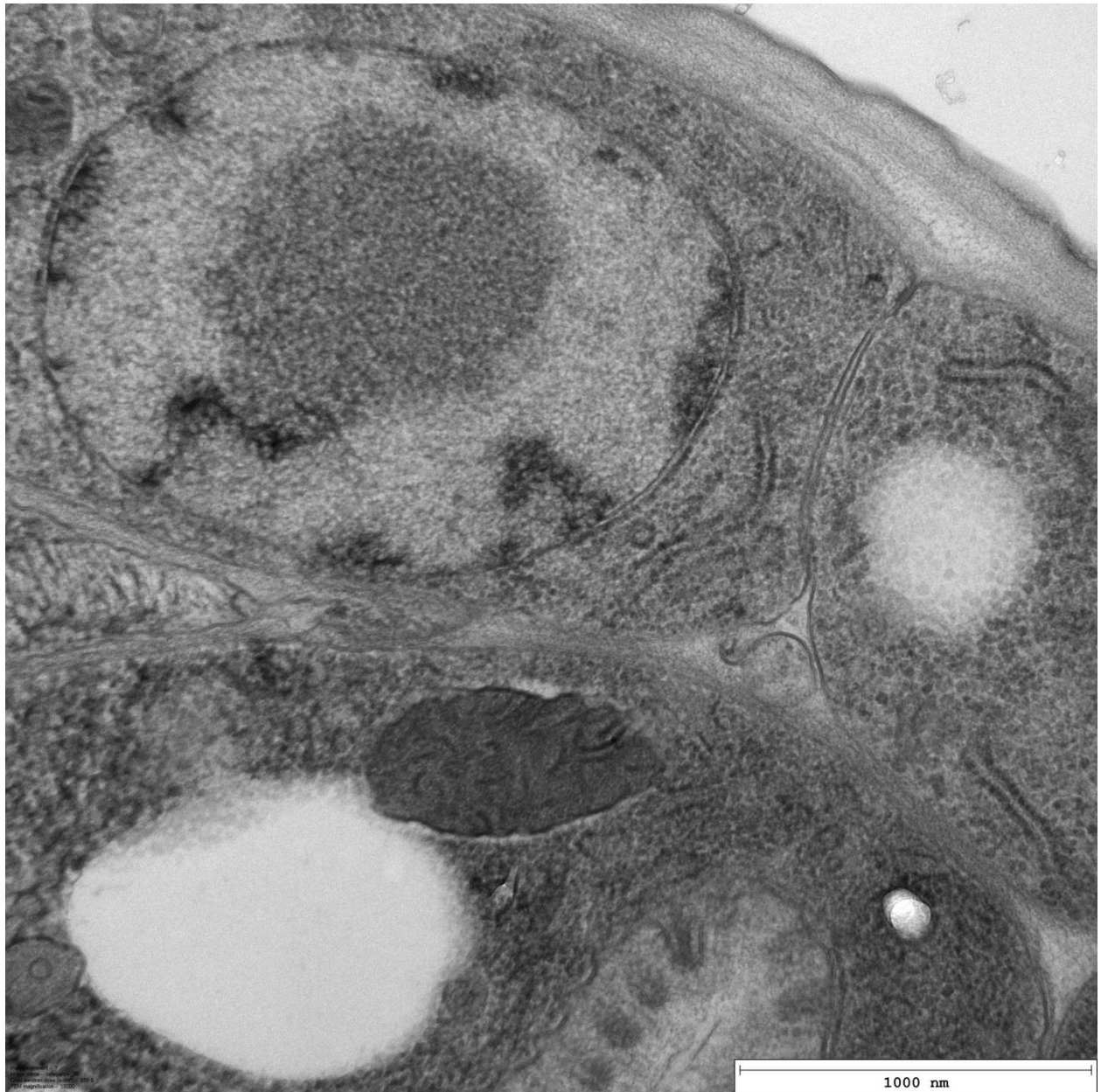


Figure 47 Higher magnification of the right white dashed region in **Figure 45**. Thin section of in situ cryofixed *C. elegans*. The nucleus shows chromatin segregation, characteristic of ice damage. However, due to the protocol utilized, it is not possible to establish if ice damage occurred upon cryofixation or during freeze substitution. White zones are voids left by the dissolving of lipid droplets. Electron microscopy sample preparation and TEM imaging were performed by Dr. Dietmar Riedel (Facility for Transmission Electron Microscopy, MPI-BPC Göttingen). Modified from [Fuest and Nocera et al., 2018].

Ice damage is seen in some parts of the sample especially in the nuclei, where some segregation patterns are observed. While it is a well-established procedure, the risk of recrystallization during freeze substitution is not completely removed and it is not possible here to distinguish between damage that occurred during cryofixation and damage that occurred during freeze substitution [Brown *et al.*, 2009]. More experiments are thus needed to establish if an even better level of

preservation can be attained with microfluidic cryofixation and optimized transfer and freeze substitution protocols.

To have an unambiguous outcome on the sample preservation quality, it is necessary to remove the freeze substitution step from the workflow and directly move the cryofixed sample from fluorescence cryo-microscopy to electron cryo-tomography [Plitzko, Rigort and Leis, 2009]. The moment this work is being written, a collaboration between our laboratory and the Plitzko-group (Dept. of Molecular Structural Biology, Max Planck Institute of Biochemistry, Munich) is under development to answer this question.

4. Preserving spatial orientation of *in situ* cryofixed samples

Preserving sample orientation is key for spatial correlation across imaging techniques. The presence of the traps makes the shape of the channel content asymmetric with respect to the yz-plane and provides landmarks for easy spatial correlation. The channel content, however, is surrounded by PDMS. To image the sample in EM, direct access to the sample is required and PDMS needs to be removed. The possibility to have the channel content freed from the outside channel material, enables further correlation with more imaging techniques. For instance, the sample could be ablated using a focused ion beam (FIB) and imaged in SEM after each ablation step to reconstruct the 3D structure of cells and organelles with electron microscopy [Kizilyaprak *et al.*, 2014]

Here, the proof of principle for the preservation of the sample shape and orientation in a correlative light end electron microscopy (CLEM) workflow is shown.

After chemical fixation of the cryofixed sample, the channel content is still visible when imaged in light microscopy. In fact, the nematode maintained the same bent body shape observed during live imaging and preserved by fast freezing (cf. **Figure 31**). On the other hand, PDMS is not transparent in SEM. Therefore, it needs to be removed to image the sample in electron microscopy (**Figure 48**).

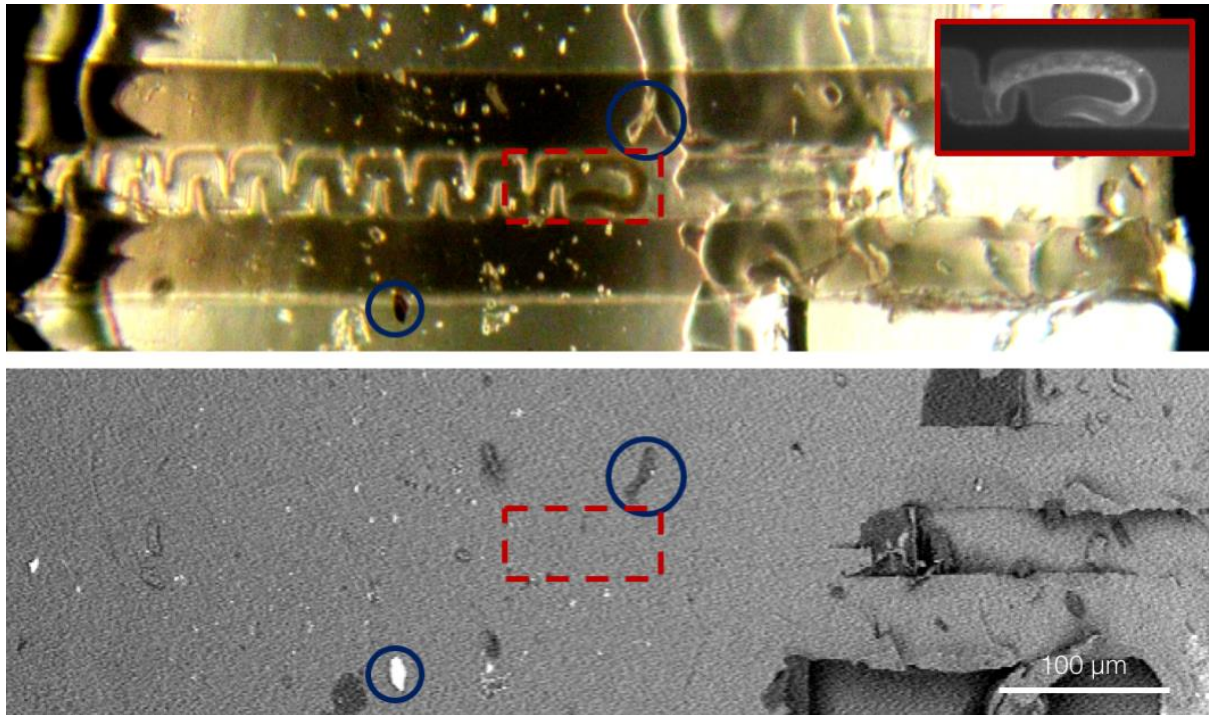


Figure 48 Sample from the in situ cryofixation of **Figure 31** after freeze substitution. Top panel: the nematode is visible in light microscopy in the microfluidic channel in the same bent shape in which it was cryofixed (red inset). Bottom panel: in SEM, the nematode is not visible through the PDMS material but its location can be retrieved using small debris as landmarks (blue circles).

The approach used here to remove of the channel material was to chemically dissolve PDMS using tetrabutylammonium fluoride (TBAF) in tetrahydrofuran (THF). TBAF is known to decompose PDMS and THF was found in literature to be the best solvent to maximize the etching rate [Kleiman, Ryu and Esser-Kahn, 2016]. **Figure 49** shows the procedure for recovering the sample and preserving its orientation.

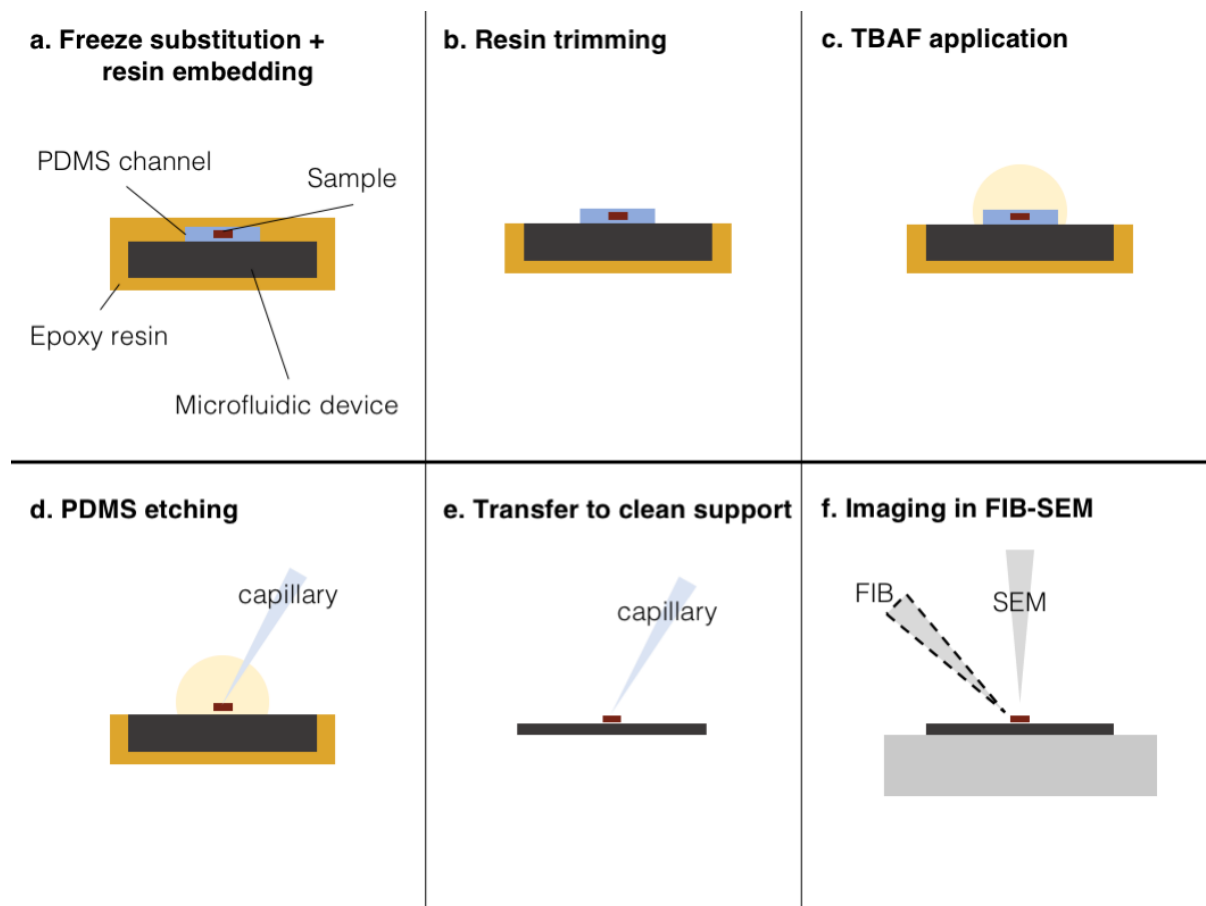


Figure 49 Schematic of the workflow that preserves sample orientation for imaging the in situ cryofixed sample in SEM following freeze substitution and resin embedding. (a) Following freeze substitution the microfluidic device containing the sample is embedded in epoxy resin. (b) PDMS was exposed milling off the excess of epoxy resin. (c) The etchant solution was applied to free the channel content from the PDMS. (d) Once free, the channel content was retrieved using a glass capillary under a stereomicroscope. (e) The channel content was then transferred to a clean support and rinsed with isopropanol to remove residues of the etchant solution. (f) The sample was then be moved to a FIB-SEM for imaging.

After freeze substitution, the sample contained in the microfluidic device was embedded in an epoxy resin. In the final step of the embedding, the microfluidic device was pressed flat against the silicone mold to minimize tilting during curing time (**Figure 49a**).

To allow the etching, the PDMS needs to be exposed to the etchant. Once the resin was cured, the excess of epoxy resin was trimmed away to expose the PDMS to the etchant (**Figure 49b**).

The etchant solution was then applied to the sample in order to free the channel content from the PDMS (**Figure 49c**).

After etching, the channel content was retrieved from the etchant solution with the help of a stereomicroscope and a glass capillary. The channel content was then transferred onto a clean support and rinsed with isopropanol to remove the residues of etchant solution (**Figure 49d-e**).

The clean sample, free from PDMS, was then be accessible for imaging in FIB-SEM (**Figure 49f**).

In **Figure 50**, the content of a microfluidic channel freed from PDMS and imaged in SEM is shown.



Figure 50 SEM image of the channel content once the channel material (PDMS) is etched off. Exposing the channel content, the sample is then suitable for FIB-SEM tomography. Using the previously acquired light microscopy images and having the trap features as fiducial markers, it is possible to retrieve the sample location with micrometer accuracy and proceed with the FIB milling. Here, the sample consists solely of epoxy resin for electron microscopy. The resin filled an empty microfluidic chip for cryofixation, which had the ends scored. After the resin was cured, the chip was processed as described in **Figure 49**. The sample was imaged in a benchtop SEM (ProX, Phenom World). The image above was reconstructed by stitching two contiguous FOVs with ImageJ Stitching plugin [Preibisch, Saalfeld and Tomancak, 2009].

With the sample in this configuration, FIB-SEM is a promising technique to correlate dynamic phenomena observed in live imaging with the ultrastructure of specific locations inside the sample. Once the PDMS is etched off, the channel features are completely visible in SEM. Previously acquired light microscopy images can be used to retrieve the sample location within the channel volume with respect to fiducial markers such as the trap features with micrometer precision. The focused ion beam can then be used to mill out resin material and expose the sample. Alternating FIB milling and SEM imaging cycles, it is possible to reconstruct the sample with sub-micrometer resolution.

A collaboration between our laboratory and Dr. Wiebke Möbius (Dept. of Neurogenetics, Max Planck Institute for Experimental Medicine, Göttingen) is currently underway to carry out this light microscopy-FIB-SEM workflow to its completeness. The possibility of adding to the workflow the immersion cryo-confocal imaging is not excluded. When completed, the workflow

will allow the spatial correlation of dynamic information from live imaging with high-resolution confocal images and electron microscopy with millisecond time resolution.

This workflow could be used, for instance, to reconstruct the complete neural activity of *C. elegans* (pan-neural imaging) using correlative light and electron microscopy. Sample could be cryofixed in situ within milliseconds following a stimulus (light, chemical, temperature change, mechanical). The cryofixed calcium signals acquired in immersion cryo-confocal could be used to highlight specific locations within the broader neural connections of the nematode (e.g. sensory neurons). Eventually, information on the early stages of the membrane trafficking (e.g. docking of vesicles, membrane fusion), could be retrieved with millisecond time resolution from samples that were previously live imaged.

Chapter 6

Temperature measurement at the microscale

A substantial part of this PhD work was spent in developing a method for the temperature measurement within the microfluidic channel. Being able to control the temperature of the channel with about 5°C precision enabled the device to cryofix viable *C. elegans*. Although RhB was eventually used to measure the temperature within the channel in a contact-less fashion, alternative methods were investigated first.

In this chapter, results from these approaches are reported.

1. Design of resistive heater with built-in electronic temperature sensors

As a first approach, a resistive heater with built-in electronic temperature sensors was designed (Figure 51).

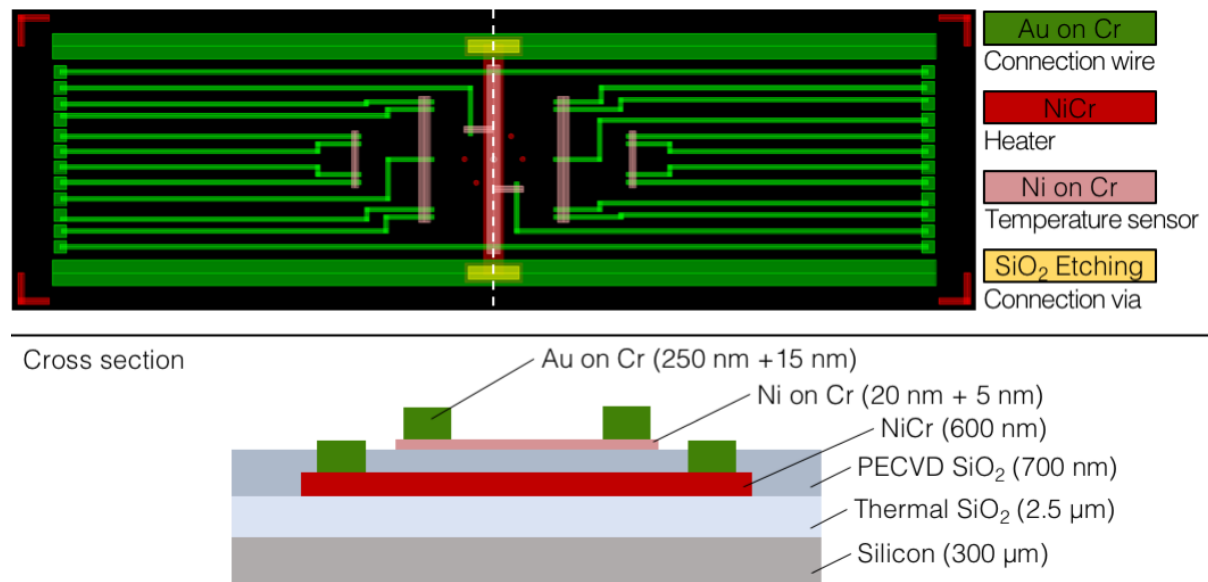


Figure 51 Outline of the microfabricated resistive heater with built-in electronic temperature sensors (top panel) and a cross section schematic corresponding to the white dashed line (bottom panel, not to scale). A silicon wafer with thermal SiO_2 was used as the heater substrate. Nickel-chrome (NiCr) was deposited as the resistive heater. Nickel (Ni on Cr) was used for the fabrication of temperature sensors. To electrically insulate NiCr and Ni layers, silicon dioxide was plasma deposited between the layers (PECVD SiO_2). PECVD SiO_2 was then etched at the extremities of the resistive heater to ensure electrical connection of the NiCr to a gold layer (Au on Cr) that was then patterned to wire the different components.

Nickel-based temperature sensors were added to the already established resistive heater outline. The original heater wafer consisted of a double-side polished silicon wafer with 2.5 μm of polished thermal silicon dioxide (Thermal SiO_2) on the heater side. Being a better thermal insulator than bare silicon, the purpose of the thermal SiO_2 layer was to contain the thermal drop between the sample at 25°C and the liquid nitrogen at -196°C. On top of the thermal SiO_2 , all

other layers were deposited. The resistive heater consisted of a nickel-chrome strip (NiCr, 600 nm). Nickel electrical resistance strongly varies with temperature. For this reason, nickel is among the materials that are commonly used to fabricate resistance-based thermometers. In this design, one main nickel temperature sensor (Ni on Cr, 20 nm + 5 nm) was placed on top of the resistive heater and two secondary temperature sensors per side were added for robustness. For electrical insulation between the NiCr and the Ni elements, a layer of silicon dioxide was plasma deposited (PECVD SiO₂, 700 nm). To insure electrical connection to the NiCr, PECVD SiO₂ was etched at the extremities of the resistive heater (SiO₂ Etching). Gold traces were used for the wiring resistive heater and temperature sensors to an external power supply and resistance readers, respectively. To prevent a voltage drop during measurement and increase accuracy, all temperature sensors were designed to have four-wire configuration resistance reading.

After fabrication, an open circuit was measured for all the metal traces crossing the NiCr layer was measured. The following measurements reported here were directly performed on the Ni and NiCr traces, after the gold traces were etched off to investigate the reason for the open circuit.

Electrical resistance measurements of the different paths of the heater outline (**Figure 52**, left panel) were used to test the continuity of the circuit formed by the deposited metal layers (**Table 8**). Resistance measurements of the metal traces were acquired with the assistance of Dr. Jörg Malindretos from the Faculty of Physics of the University of Göttingen.

Table 8 Measured electrical resistances and, in parentheses, their expected values for different elements of the wafer outline. Measurements collected with the assistance of Dr. Jörg Malindretos, Faculty of Physics (University of Göttingen).

RESISTANCE PATH	ELECTRICAL RESISTANCE (Ω)
A-B	~ 25 (~ 20)
C-D	~ 200 (~ 20)
E-F	Open (~ 15)

The nickel traces (C-D measure) showed a ten-fold higher resistance compared to the expected value. This can be due to oxidation of the metal surface. Resistance values of the NiCr traces (A-B), on the other hand, were much closer to expectation. In fact, NiCr traces were much thicker and protected by the PECVD SiO₂ layer that was removed right before the measurement. However, the open circuit across the E-F path cannot be explained by oxidation of the layer.

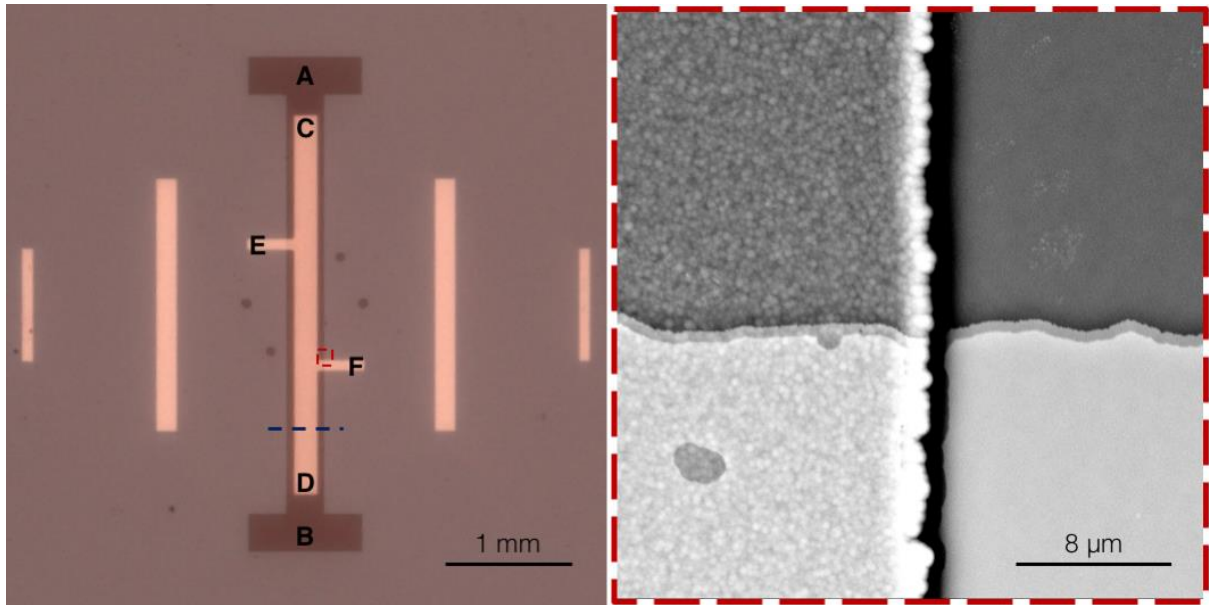


Figure 52 Top view of the patterned NiCr and Ni of the resistive heater with built-in electronic temperature sensors. (Left) Labeling of the measured resistances across the heater pattern. A-B, NiCr heater layer; C-D, Ni sensor layer; E-F, Ni sensor layer crossing NiCr. (Right) Detail in scanning electron microscopy (SEM) of the highlighted region of interest (red dashed line) in the left panel. The Ni layer appears interrupted when crossing the SiO₂ step. Blue dashed line represents the location of the cross section in **Figure 53**.

Since both paths A-B and C-D appeared continuous, the issue was likely due to the poor step coverage of the Ni layer over the edge of the PECVD SiO₂ on NiCr. Observing the edge of the PECVD SiO₂ on NiCr in scanning electron microscopy, a shadow was visible (**Figure 52**, dashed red ROI). Although the presence of the shaded area along the NiCr edge is not a direct sign of the Ni layer discontinuity, it indicated the presence of a step. However, from this perspective it was not possible to assess whether the Ni layer was conformal to the PECVD SiO₂ step or whether it was interrupted.

A cross-section of the heater wafer allowed the comparison of the relative height of the different layers forming the heater (**Figure 53**).

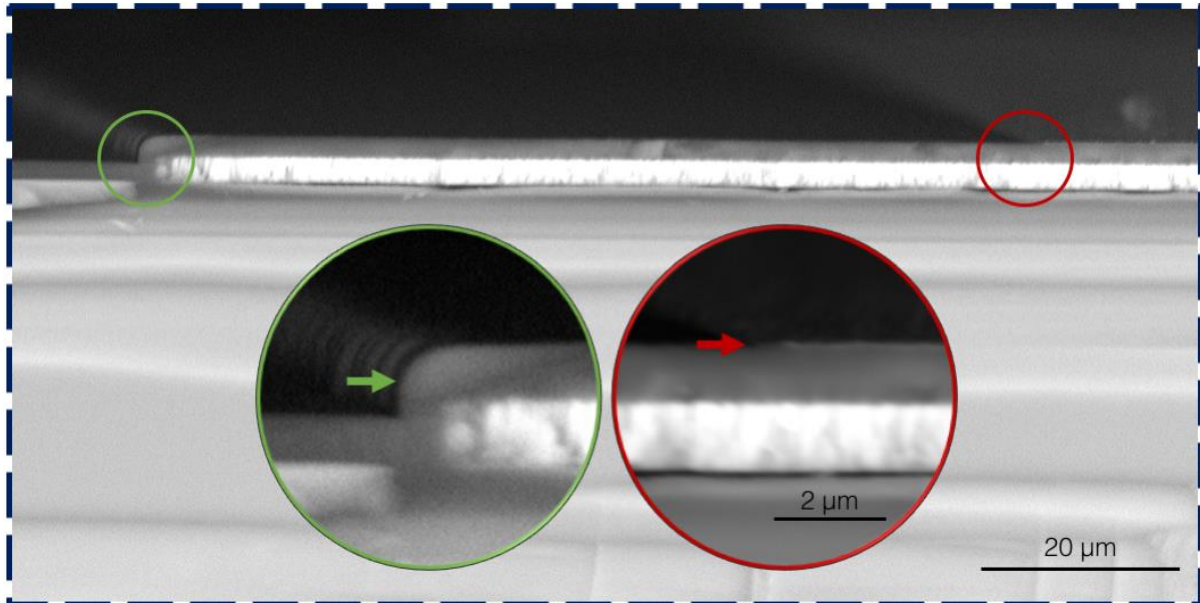


Figure 53 Cross-section view of the heater layers at 45° angle. Cut was performed on an equivalent region as indicated by the blue dashed line in the left panel of **Figure 52**. From this image, it is possible to compare the relative heights of the PECVD SiO₂ step (green arrow, ~1 μm) and the Ni layer (red arrow, ~50 nm).

In the green inset of the SEM image, the PECVD SiO₂ step is visible across the edge of the NiCr layer (green arrow). In the red inset of the SEM image, the Ni layer on top of the PECVD SiO₂ is also visible (red arrow). SiO₂ and Ni layers were measured to be ~1 μm and ~50 nm thick, respectively.

Although it was not possible to precisely break the wafer across the 100 μm wide Ni finger that crosses the SiO₂ step, it is possible to imagine that the 50 nm sputtered Ni layer could not have covered the 1 μm step (**Figure 54**).

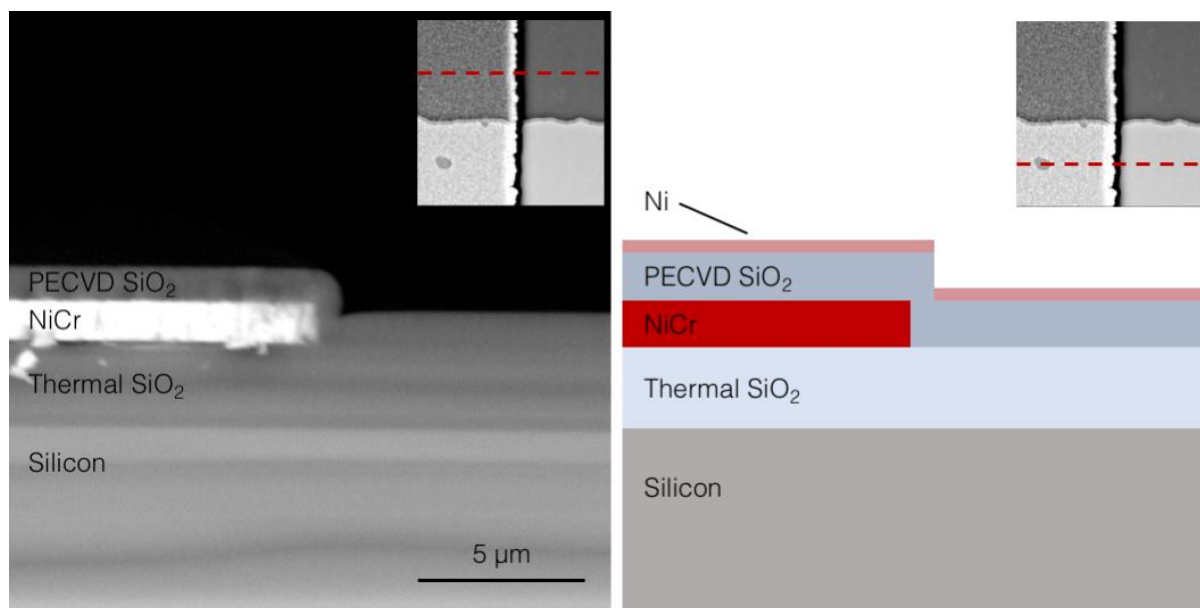


Figure 54 (Left) Cross-section view of the heater layers PECVD SiO_2 step over the NiCr. (Right) Schematic showing how the discontinuity of Ni layer would appear crossing the PECVD SiO_2 step (not to scale).

Plasma enhanced chemical vapor deposition (PECVD) is usually preferred over sputtering because the vapor phase of the material makes the layer more conformal to already existing features. Therefore, it is more suitable for step coverage purposes. The unaccomplished step coverage of the thin Ni layer might be explained by the large thickness of the NiCr. In fact, the thickness of NiCr was double the measured value during deposition. With a NiCr layer of 600 nm instead of 1200 nm, the 1 μm PECVD SiO_2 might have been able to smooth the step, sufficiently to prevent the discontinuity of the Ni layer deposited on top.

2. Visualization of temperature gradients within microfluidic channel volume

Using RhB dissolved in water it was possible to calibrate the resistive heater with enough precision to use the microfluidic device to cryofix living biological samples. However, the use of bulk solutions of RhB can only give an average measurement of the temperature within the microfluidic channel with no information on the possible presence of thermal gradients within the volume of the channel. Large temperature gradients could affect the health state of biological samples, inducing, for instance, the undesired expression of heat-shock proteins to compensate the thermal stress.

Using point-like temperature probes would allow temperature measurement at defined location within the volume of the channel. In this way, the detection of temperature gradients

within the channel volume would be enabled. As temperature-sensitive point-like probes, 1 μm rhodamine B-loaded melamine beads suspended in water were used.

To measure the temperature sensitivity of the beads, multiple cycles between 25°C and 35°C were run. The same cycles were plotted to compare relative intensities over time (**Figure 55**).

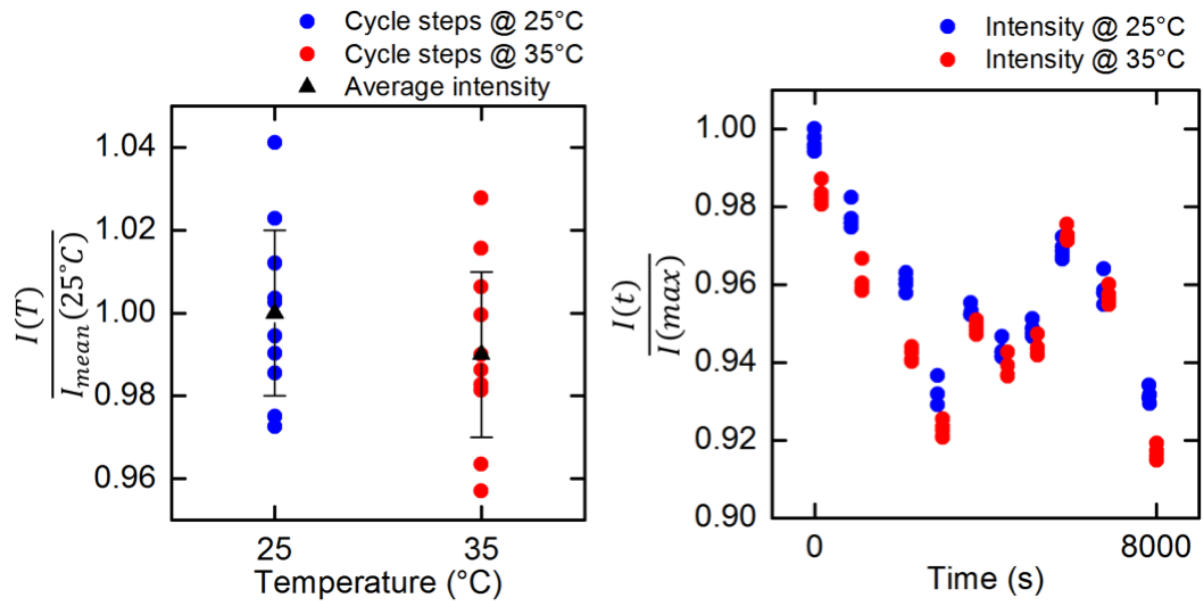


Figure 55 (Left) Intensity measurement of 1 μm RhB-loaded polymer beads over temperature cycles. Error bars represent the standard deviation calculated over ten measurements. Intensity only changed within the error bars, excluding the possibility to use these beads to detect thermal gradients in the microfluidic channel. (Right) Intensity measurement of the RhB-loaded polymer beads over the time of the temperature cycle experiment. The oscillation of intensity is believed to depend on the particles going out of focus over the long measurement time.

The fluorescence intensity of the beads only changed within the error bars as the temperature was varied. The insufficient change in intensity with the temperature prevented the use of these beads to detect thermal gradients within the microfluidic channel.

The oscillating trend observed throughout the temperature cycles was likely intrinsic of the measurement method utilized (**Figure 55**, right). Beads were suspended in water. At low Reynolds numbers, the sedimentation velocity (w) of a particle in a fluid is Eq.(11)

$$w = \frac{2(\rho_p - \rho_f)g r^2}{9\mu_f} \quad (11)$$

Where ρ_p and ρ_f are the density of the particle and the fluid, respectively; g is the gravitational acceleration, r is the radius of the particle and μ_f is the dynamic viscosity of the fluid.

For the 1 μm beads with density of 1.57 $\text{g}\cdot\text{cm}^{-3}$, the sedimentation velocity was found to be about 3 $\mu\text{m}\cdot\text{s}^{-1}$. At this velocity, the particles should have settled at the bottom of the capillary in maximum 2 minutes. However, the temperature cycles might have generated convection within the capillary that prevented the beads from settling.

To assess the presence of bleaching, beads were continuously exposed over time (**Figure 56**, left). The extent of the accuracy of the measurement was assessed by the plot of the residuals of the fitted bleaching curve (**Figure 56**, right).

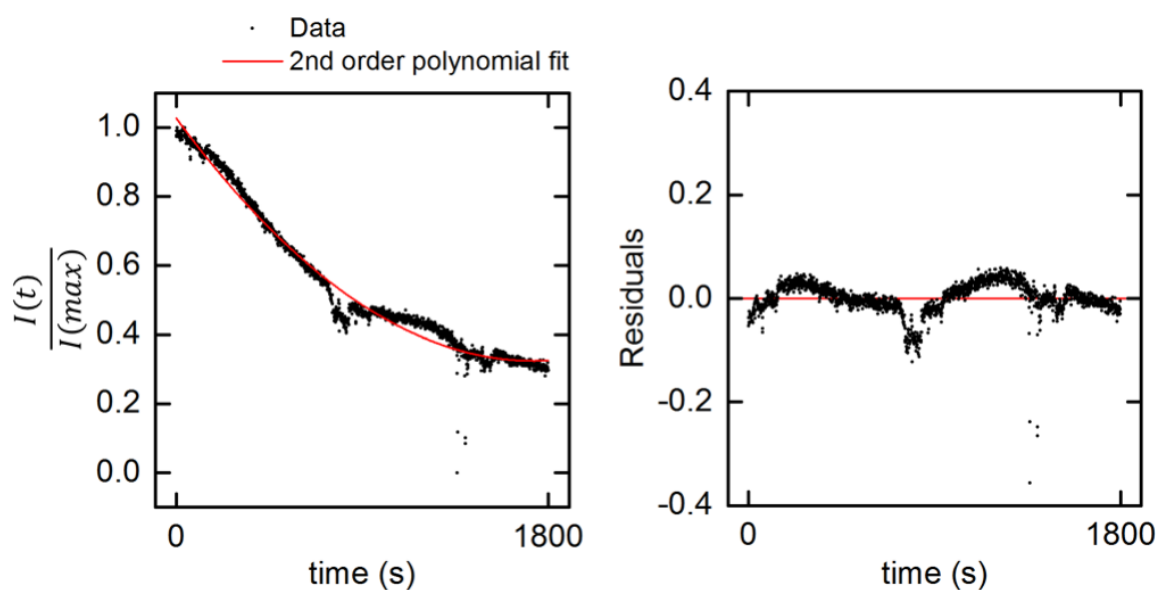


Figure 56 (Left) Bleaching measurement of the RhB-loaded polymer beads. (Right) Residuals of the fit for the bleaching of the RhB-loaded polymer beads. The standard deviation of the residuals was found to be equal to 3% of the measured intensity, consistent with the value of accuracy found for the temperature measurement of the bulk RhB solution.

Data in **Figure 56** was fit with a second order polynomial of the form

$$I = B_0 + B_1 t + B_2 t^2 \quad (12)$$

where I is the fluorescence intensity, t is the time and the factors B_n have the values reported in **Table 9**.

Table 9 Second order polynomial fit coefficients from **Eq. (12)** with respective standard errors.

B_0	1.0 ± 0.03
B_1	$-8 \cdot 10^{-4} \pm 6 \cdot 10^{-6}$
B_2	$2 \cdot 10^{-7} \pm 3 \cdot 10^{-9}$

The polynomial fit provided an R-squared value of 0.9788.

To estimate the minimum error achievable from the bead intensity measurement, the standard deviation of the residuals of the fitting curve was used (**Figure 56**, right panel). The standard deviation of the residuals was found to be equal to 0.03 for the normalized intensity, equivalent to the 3% of the measured intensity. This value is consistent with the previously found error of 2.4% for the measurement of the RhB water solution.

2.1. Effect of the solid matrix on the temperature coefficient of fluorescence of RhB-loaded melamine beads

The dependence on temperature of the of RhB fluorescence intensity was not consistent between the measurements in solution and in the polymer matrix. Over a 10°C temperature span, the change in intensity of the beads was about 1% whereas it was ten times greater when measured in solution.

Red shifts in both excitation and emission spectra of rhodamine B were already reported in the literature when the dye is placed in a non-polar solvent or in a polymer matrix [Casey and Quitevis, 1988; Soleilhac *et al.*, 2016]. Melamine is a highly cross-linked and unsaturated polymer. The smaller sensitivity of the dye might have been caused by the red shift of RhB in the beads. The excitation filter used for the particle measurements provided a 10-nm window centered at 546 nm. If the red shift moved the maximum of absorbance outside the excitation window, the effective excitation of RhB was dramatically less intense than the one in solution, causing a substantial decrease in emission intensity and therefore in temperature sensitivity.

Chapter 7

Conclusions and Outlook

In this thesis, the imaging of *C. elegans* specimens in light and electron microscopy with millisecond time resolution was shown. For the first time, a microfluidic system for cryofixation was able to be used for living organisms. The system controls the temperature of a microfluidic channel via a resistive heater while the channel is on top of a heat sink partially submerged in liquid nitrogen. When the heater is turned off, the content of the microfluidic channel freezes fast enough to prevent water crystallization. Specimens were successfully live-imaged and cryofixed within the field of view of the light microscope. Moreover, the applicability of the cryofixation system to correlative microscopy applications was demonstrated. Cryofixed samples were recovered from the device and transferred for imaging in immersion cryo-confocal microscopy. Comparing the images acquired in widefield and immersion cryo-confocal imaging, a 20-fold increase in contrast was measured.

In order to assess the preservation quality of the samples, *C. elegans* cryofixed using the microfluidic system were also processed for electron microscopy. Following recovery of the samples, *C. elegans* were chemically fixed using a standard freeze substitution protocol. Samples were then sectioned for imaging in transmission electron microscopy. Electron microscopy revealed that membranes and organelles of the nematode were free from ice damage. Nuclei showed chromatin segregation patterns, characteristic of poor freezing quality. However, with the method used for the sample process, it was not possible to assess whether the damage occurred during freezing or during freeze substitution.

To preserve the sample orientation throughout the light and electron microscopy workflow, a protocol for the sample processing was developed. The content of microfluidic channels for cryofixation was freed from the channel material for imaging in scanning electron microscopy. A collaboration to implement the protocol in a light microscopy/FIB-SEM workflow is currently under development.

1. Limitations of cryofixation in microfluidic systems

Among the fundamental limitations of cryofixation in microfluidic systems is the thermal conductivity of water. Thermal conductivity dictates the fastest rate at which heat can be extracted from a material, ultimately limiting the size of a sample that can be cryofixed at atmospheric pressure. In fact, this limitation also imposes the use of cryoprotectants for samples that exceed a few micrometers in thickness. However, sample size is not the only parameter that water thermal conductivity limits; a limit on the cooling rate also implies a limit on the time resolution that can be achieved by the device. Ultimately, requiring cooling rates of 10^4 – 10^6 °C·s⁻¹

to prevent ice damage on biological samples, the time resolution of the device is necessarily in the order of 1–100 μs [Burg, 2012; Mejia *et al.*, 2014].

A second fundamental limitation is the requirement to work with air objectives. Air objectives are limited in their numerical aperture ($\text{NA} \leq 1$). The low numerical aperture limits the achievable spatial resolution of the cryofixation event.

Among the technological limitations of the device version used in this thesis work, the most critical is the cooling rate, limited by the distance between the sample and the main heater. This distance is given by the thickness of the PDMS material that forms the bottom of the microfluidic channel. The thinnest channel bottom achievable with the fabrication approach used here was of $\sim 17 \mu\text{m}$ (**Figure 9**). COMSOL simulations showed that to reach cooling rates accepted to be necessary to achieve good cryofixation of biological samples ($10^4 \text{ }^\circ\text{C}\cdot\text{s}^{-1}$ or greater), a bottom thickness of $5 \mu\text{m}$ or smaller is required [Mejia *et al.*, 2014]. By adding cryoprotectants the requirements to achieve good preservation are more relaxed. Indeed, TEM images of cryofixed *C. elegans* showed good preservation of the sample everywhere except in the most fragile regions, the nuclei, despite the thicker bottom (**Figure 45**, **Figure 46**, **Figure 47**). Results achieved with the thicker bottom were comparable to the ones achieved by slam freezing [Allison, Daw and Rorvik, 1987]. Nonetheless, the improvement of the sample preservation quality was set as a priority in the development of the next version of the fluidics for the cryofixation device. In fact, many efforts in the past years were deployed in developing a new fabrication procedure that would allow fabrication of channel with bottom walls less than $5 \mu\text{m}$ thick [Fuest *et al.*, 2017]. By thinning the bottom layer of the microfluidic channel, the preservation quality of samples will increase, with the possibility to minimize cryoprotectant concentration and thus the risk of toxicity for the sample.

A second current technological limitation of the device is the irreversibility of the cryofixation. If the main heater is turned back on after a living sample was cryofixed, the thawed sample is dead. With the possibility to reverse the cryofixation of a biological sample, a long biological process could temporarily be arrested during its faster stages, images could be acquired without exposure time limitations, and later the process could be re-started to let the process continue – ideally unperturbed. A device of this kind would have the unique potential to answer questions on the reactions of a biological system to rapid temperature changes. In fact, it was shown that the temperature sensory systems of *C. elegans* have a reaction time on the order of seconds to minutes to detect a temperature change [Kimata *et al.*, 2012]. Therefore, a three orders of

magnitude faster temperature change could potentially be undetected by the nervous system due to the arrest of the diffusion-based mechanisms. On the other hand, more rapid changes (e.g. molecule conformations) could still take place, with the possibility to trigger secondary pathways.

At the current state, it is not clear whether the death of the thawed specimens occurs during cooling or warming of the samples. Depending on the stage at which the recovery becomes irreversible, different approaches can be attempted to overcome this limitation. Ice crystal damage upon thawing is expected if the main heater is the only heat source. With a slow warming up, the sample does not cross fast enough the temperature region where crystallization of water is thermodynamically inevitable ($-137^{\circ}\text{C} - 0^{\circ}\text{C}$), irreversibly damaging the sample. To speed up the thawing process, a supplementary heat source is necessary. The easiest way to add heat to the process is overshooting the power of the main heater in the moment it is turned back on. To have a more homogeneous heating of the channel volume, thermal energy could be transferred to the sample via irradiation in the infrared or microwave range.

An alternative approach to achieve reversible cryopreservation of biological samples could be to prevent any freezing. Instead, the temperature of the sample could be lowered enough to slow down biological processes but not so low that ice crystallization occurs. Under specific conditions, water can remain in a liquid state also far below its freezing point [Mishima and Stanley, 1998]. This supercooled state is a metastable state, meaning that crystallization is still thermodynamically favorable. However, a small energy barrier needs to be overcome before crystallization can start. If that energy is not provided by the environment, the supercooled state can persist indefinitely. The use of supercooling was shown to dramatically decrease the dynamics of molecules in the cell environment and can be used to reversibly arrest biological processes [Masip *et al.*, 2016]. Masip *et al.* decreased the temperature of the sample over multiple steps and at each step increased the concentration of DMSO (dimethyl sulfoxide) in the cell media. DMSO is a permeant cryoprotectant that is highly toxic at 37°C but its toxicity is strongly reduced at low temperature. In the experiments of Masip *et al.*, a complete cycle of cooling and warming lasted about one hour, due to the time required to replace the media at every cooling/warming step. In the future, the use of microfluidics may enable significantly faster perfusion and shorter temperature cycles. This will require rapid control of the power supplied to the device to reach precise intermediate temperatures between room temperature and liquid nitrogen temperature.

2. Limitations of cryoimmersion setup

Mechanical stability of the cryo-stage and temporary image loss are among the most important technological limitations of the current version of the cryoimmersion light microscopy setup (Figure 57).

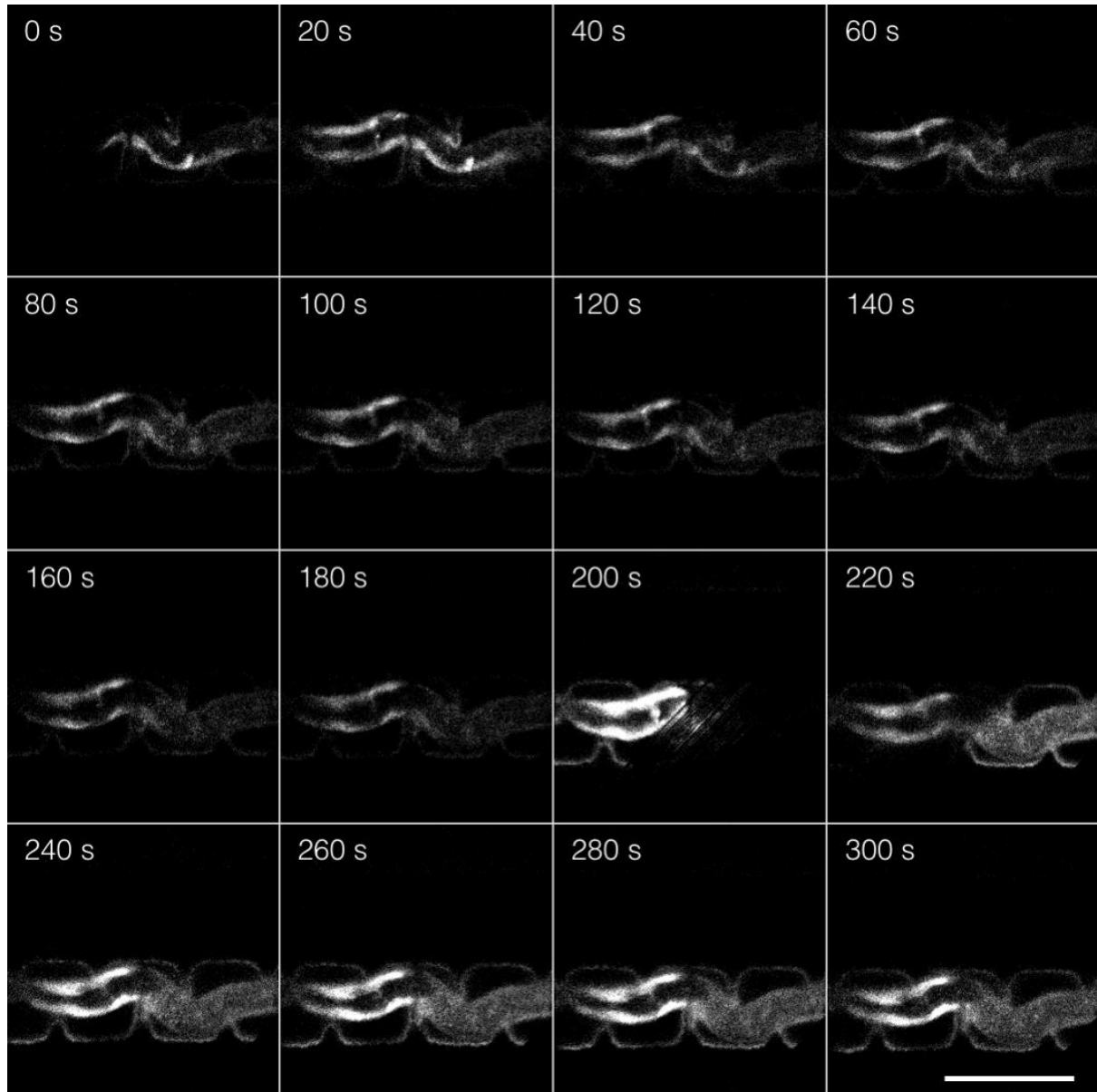


Figure 57 Lateral drift and image interruption during a long-time acquisition in cryoimmersion microscopy. Data acquired in collaboration with Margherita Bassu, PhD. Scale bar measures 50 μm .

From the collage, it is possible to see that over time the sample drifts towards the lower part of the FOV. Furthermore, at timestamps “0 s”, “200 s” and “220 s” the sample is only partially visible. Both issues are related to technological aspects of the device. Lateral drift is on the order of a few micrometers per minute (Figure 58).

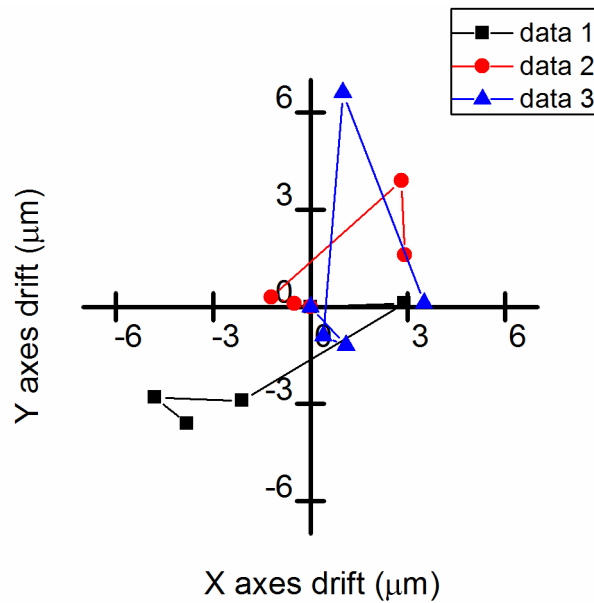


Figure 58 Tracing of the lateral drift. Time interval between points of the same data set is 1 minute. Data acquired in collaboration with Margherita Bassu, PhD.

The origin of the image interruption is not fully clarified yet. Most of the times, it is possible to recover the image by flushing new immersion fluid. It is plausible that the signal is interrupted by air bubbles, ice crystals, or particles trapped in the optical path between the objective and the sample.

Among the possible objects interfering with the light path, air bubbles are the most likely. Air bubbles might be introduced through the immersion fluid supply system or the internal nitrogen purging system of the objective itself. To avoid water condensation between lenses, the objective is continuously flushed with dry nitrogen gas that could be leaking out too close to the front lens. In case the air bubbles are coming from the immersion fluid supply, the syringe system could be modified to a pressure-driven supply system consisting of a vial that can be refilled during the experiment to prevent air leaking into the tubing.

To improve mechanical stability of the cryo-stage, a re-design of the stage cooling system is currently under development. The new cryo-stage will exploit a heavier mass and smoother geometry to be less susceptible to the vibrations transferred from the liquid nitrogen boiling.

Although image interruption was clearly a disadvantage during data acquisition, it was helpful to visualize the dark state recovery of GCaMP for the first time. In fact, from the timestamp “200 s” on of **Figure 57**, the muscles of the nematode are brighter than before the image interruption. This can be explained by the increase in population of GCaMP in their electronic ground state during the time light could not reach the camera nor the sample. Once the imaging

was restored, the more populated ground state was excited again emitting more photons than in the previous condition [Moerner and Orrit, 1999; Giske, 2007] (**Figure 59**).

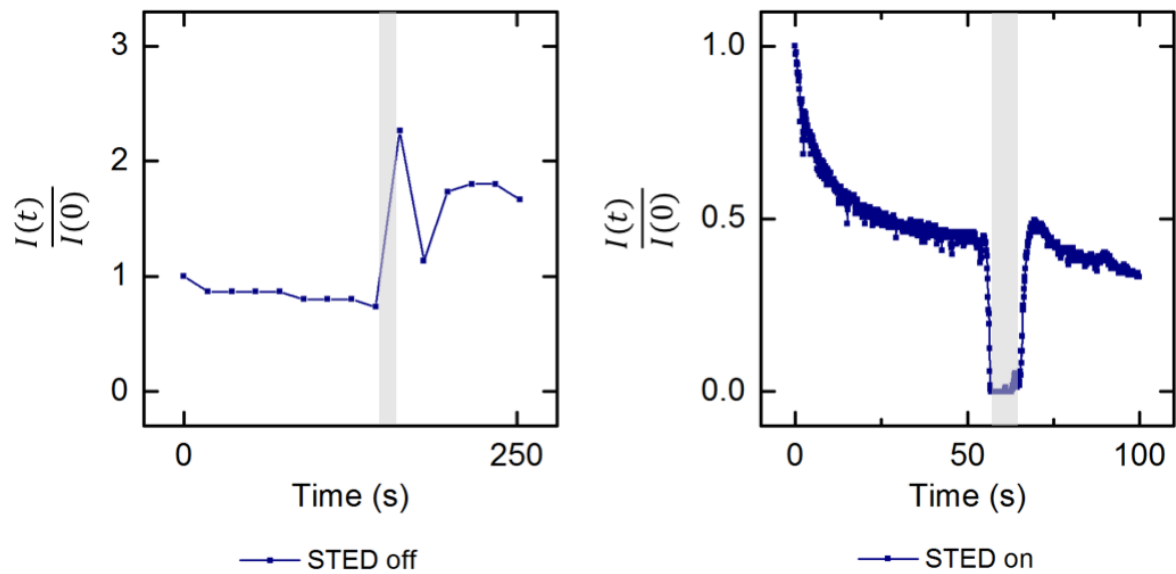


Figure 59 GCaMP intensity increase after imaging interruption due to setup instability (shaded area). Upon recovery of the signal, fluorescence intensity consistently increased in both confocal mode and when the STED beam was on. Data acquired in collaboration with Margherita Bassu, PhD.

Characterizing the kinetics of the GCaMP dark state recovery, it would be possible to know the minimum time required between each acquisition to always have the fluorophore emitting, for instance, above 90% of its maximum quantum yield.

Acknowledgements

In the first place, I want to thank Dr. Thomas Burg for giving me the possibility of joining his laboratory, first as Master student and later to pursue my studies on this project. His openness to discussions at any moment were of invaluable importance throughout these years.

I would like to thank Professor Sarah Köster and Professor Stefan Hell, for having accepted being part of my Thesis Committee. Their support and interest in the project, together with communicating their precious point of views have been extremely important to keep up the motivation in my work.

And thanks to Dr. Henrik Bringmann, Prof. Jörg Enderlein and Prof. Silvio Rizzoli, for having agreed in being part of my Extended Examination Board.

A special mention goes to my colleagues. I want to thank all current and past members of the Burg Laboratory whose time overlapped with mine: Margherita Bassu, Stanislav Bojko, Holger Bolze, Raffaele Faoro, Hélène Foussard, Marie Fuest, Rodrigo Ignacio Galilea Kleinsteuber, Rachel Lowe, Yara Mejia, Jan-Erik Messling, Mario Modena, Foelke Purr and Yu Wang.

For the help I have received while working at the Georg-August-University of Göttingen, I want to thank Dr. Ingo Gregor, Joachim Herbst, Thomas Lehmann, Dr. Joerg Malindretos and Dr. Weixing Li. For the precise feedbacks and proofreading of the manuscript, I want to express my sincere gratitude to Riccardo Belardinelli and Marie Fuest.

The current extent of this work would not have been possible without the top-notch technical support available at Max Planck Institute for Biophysical Chemistry. I deeply want to thank all Facilities that I have annoyed with my requests over these years and in particular the Facility for Synthetic Chemistry in the person of Dr. Vladimir Belov, the Facility for Transmission Electron Microscopy in the person of Dr. Dietmar Riedel and all the kind and skilled people of the Workshop for Precision Mechanics.

For the discussions about fluorescence at low temperature, I want to thank my friends and former university colleagues Dr. Greta Donati (University of Salerno) and Dr. Alessio Petrone (University of Washington).

It is now time to acknowledge my thankfulness to whomever was outside the lab. Although four years have gone, I have the perception this experience started only a few weeks ago. The vivid memories of more than four-years-worth of events rush into my mind and now it is time to acknowledge the many that made this time an unforgettable experience. It is hard for me to find the correct words to describe how lucky I have been in finding in Göttingen the right people to spend my spare time with. Meeting them changed for the better not just my PhD experience but my life in general. The list of people to mention is quite long, I will try to name them – more or less – “in order of appearance” into my life: Mario Modena, Alessandra Rolando, Annalisa Modena, Roberto Rizzato, Bianca Iacobellis, Giulio Rocco, Mirko Lukovic, Ilaria Testa, Michael Ratz, Elisa D’Ester, Raffaella Garofalo, Riccardo Belardinelli, Rebecca Belardinelli, Massimo Oldani, Barbara Cambiagli, Matteo Novara, Elena Pisapia, Gianpiero Cera, Tobias Hattendorff, Montse Torres, Müge and Sebastian Kasanmascheff, Tomas Orlando, Tahere Kalantary, Claudia Schmidt, Vedran Vasic, Emma Lomonte, Judith Strauß. Thank you all, I have enjoyed almost every moment of the time spent together.

In mixed order, because they strongly deserve to be part of this, I also want to thank: Angelo and Ciro Astarita for being there during those formative years, Vittorio Causa for his peerless contribution to my education, Frank Malone for all the booze and *friarielli* when I needed them the most. Thanks to Lorenzo Barolo, Salvatore Costanzo, Gabriella D’Escamard, Stefania Esposito, Rosario Oliva, Martina Terracciano, Marco Vastano and Gianluigi Verde for having started university when I did it, where I did it. And thanks to Valentina Abbate, Michele Carandente, Antonello Faiella, Salvatore Fatigati, Paolo Russo and Angela Tortora for sharing with me the same vision of, and attitude toward the world.

The final but most important acknowledgment goes to my family. My bridge over troubled water. They supported every life decision I made over these twenty-nine years. Thanks to them I could study in three different countries, learning languages, experiencing life as I could never have imagined otherwise. Their contribution, from my upbringing until now, has been crucial in all I have achieved so far. To them goes a thanking beyond any academic formality.

Il ringraziamento finale ma più importante va alla mia famiglia. Coloro i quali, in questi ventinove anni, hanno incoraggiato tutte le mie scelte. Grazie al loro supporto ho potuto studiare in tre Paesi diversi, imparare lingue straniere e fare esperienze che non avrei mai potuto immaginare altrimenti. Il loro contributo, dalla mia prima educazione fino all’età adulta, è stato di

primaria importanza a ciò che sono riuscito a conseguire fino ad ora. Quello per loro è un grazie che va al di là dei formalismi da fine tesi di dottorato.

Recurring Abbreviations

AFP	Antifreeze protein
APD	Avalanche photodiode
BOE	Buffered oxide etchant
CLEM	Correlative light-electron microscopy
CMOS	Complementary metal-oxide-semiconductor
DI water	Deionized water
DIC	Differential interference contrast
DMSO	Dimethyl sulfoxide
EM	Electron microscopy
EMCCD	Electron multiplying charge-coupled device
FIB	Focused ion beam
FOV	Field of view
Fps	Frames per second
FWHM	Full width half maximum
GFP	Green fluorescent protein
HPF	High pressure freezing/freezer
NA	Numerical aperture
PCB	Printed circuit boards
PDMS	Polydimethylsiloxane
PECVD	Plasma enhanced chemical vapor deposition
RhB	Rhodamine B
ROI	Region of interest
SEM	Scanning electron microscopy
STED	Stimulated emission depletion
TBAF	Tetrabutylammonium fluoride
TEM	Transmission electron microscopy
THF	Tetrahydrofuran
CEMOVIS	Cryo-EM of vitrified sections
<i>C. elegans</i>	<i>Caenorhabditis elegans</i>
LN ₂	Liquid nitrogen
GCaMP	Calcium sensitive GFP

Bibliography

- Akerboom, J. et al.** (2012) 'Optimization of a GCaMP Calcium Indicator for Neural Activity Imaging', *The Journal of Neuroscience*, 32(40), pp. 13819–13840.
- Al-Amoudi, A. et al.** (2004) 'Cryo-electron microscopy of vitreous sections', *The Embo Journal*, 23(18), pp. 3583–3588.
- Alberts, B. et al.** (2002) *Molecular Biology of the Cell*. Sixth edit. Garland Science, Taylor and Francis Group.
- Allison, D. P., Daw, C. S. and Rorvik, M. C.** (1987) 'The construction and operation of a simple inexpensive slam freezing device for electron microscopy', *Journal of Microscopy*, 147(1), pp. 103–108.
- Berezin, M. Y. and Achilefu, S.** (2010) 'Fluorescence lifetime measurements and biological imaging', *Chemical Reviews*, 110(5), pp. 2641–2684.
- Best, B. P.** (2015) 'Cryoprotectant Toxicity: Facts, Issues, and Questions', *Rejuvenation Research*, 18(5), pp. 422–436.
- Betzig, E. et al.** (2006) 'Imaging Intracellular Fluorescent Proteins at Nanometer Resolution', *Science*, 313(5793), pp. 1642–1645.
- de Boer, P., Hoogenboom, J. P. and Giepmans, B. N. G.** (2015) 'Correlated light and electron microscopy: ultrastructure lights up!', *Nature Methods*, 12(6), pp. 503–513.
- Boothby, T. C. et al.** (2017) 'Tardigrades Use Intrinsically Disordered Proteins to Survive Desiccation', *Molecular Cell*, 65(6), p. 975–984.e5.
- Brenner, S.** (1974) 'The genetics of *Caenorhabditis elegans*', *Genetics*, 77(1), pp. 71–94.
- Brown, E. et al.** (2009) 'Studying intracellular transport using high-pressure freezing and Correlative Light Electron Microscopy', *Seminars in Cell and Developmental Biology*, 20(8), pp. 910–919.
- Burg, T. P.** (2012) 'Ultra-rapid freezing device and Method'.
- Candelier, R. et al.** (2015) 'A microfluidic device to study neuronal and motor responses to acute chemical stimuli in zebrafish', *Scientific Reports*, 5, p. 12196.
- Casey, K. G. and Quitevis, E. L.** (1988) 'Effect of solvent polarity on nonradiative processes in xanthene dyes: Rhodamine B in normal alcohols', *The Journal of Physical Chemistry*, 92(23), pp. 6590–6594.
- Cavalier, A., Spohner, D. and Humbel, B. M.** (2009) *Handbook of cryo-preparation methods for electron microscopy*. CRC Press.
- Celik, Y. et al.** (2013) 'Microfluidic experiments reveal that antifreeze proteins bound to ice crystals suffice to prevent their growth - Supporting Information', *Proceedings of the National Academy of Sciences*, 110(4), pp. 1309–1314.
- Chang, Y.-W. et al.** (2014) 'Correlated cryogenic photoactivated localization microscopy and cryo-electron tomography.', *Nature methods*, 11(7), pp. 737–9.
- Chaudhury, A. R. et al.** (2017) 'On chip cryo-anesthesia of *Drosophila* larvae for high resolution in vivo imaging applications', *Lab on a Chip*. The Royal Society of Chemistry, 17(13), pp. 2303–2322.
- Chauhan, V. M. et al.** (2014) 'Thermo-optical characterization of fluorescent rhodamine B based temperature-sensitive nanosensors using a CMOS MEMS micro-hotplate', *Sensors and Actuators, B: Chemical*. Elsevier B.V., 192, pp. 126–133.
- Chiu, P. L., Kelly, D. F. and Walz, T.** (2011) 'The use of trehalose in the preparation of specimens for molecular electron microscopy', *Micron*, 42(8), pp. 762–772.
- Chronis, N., Zimmer, M. and Bargmann, C. I.** (2007) 'Microfluidics for in vivo imaging of neuronal and behavioral activity in *Caenorhabditis elegans*', *Nature Methods*. Nature Publishing Group, 4(9), pp. 727–731.

- Clokey, G. V. and Jacobson, L. A.** (1986) ‘The autofluorescent “lipofuscin granules” in the intestinal cells of *Caenorhabditis elegans* are secondary lysosomes’, *Mechanisms of Ageing and Development*, 35(1), pp. 79–94.
- Coburn, C. et al.** (2013) ‘Anthranilate Fluorescence Marks a Calcium-Propagated Necrotic Wave That Promotes Organismal Death in *C. elegans*’, *PLoS Biology*, 11(7), p. e1001613.
- Cole, R.** (2014) ‘Live-cell imaging: The cell’s perspective’, *Cell Adhesion and Migration*, 8(5), pp. 452–459.
- Debenedetti, P. G.** (1996) ‘Metastable liquids: concepts and principles’. Princeton University Press, p. 411.
- Dobro, M. J. et al.** (2010) ‘Plunge freezing for electron cryomicroscopy’, *Methods in Enzymology*, 481(C), pp. 63–82.
- Dubochet, J.** (2007) ‘The Physics of Rapid Cooling and Its Implications for Cryoimmobilization of Cells’, *Methods in Cell Biology*, 2007(79), pp. 7–21.
- Dubochet, J. and McDowell, A. W.** (1981) ‘Vitrification of Pure Water for Electron Microscopy’, *Journal of Microscopy*, 124(3), pp. 3–4.
- Dykstra, M. J.** (1992) *Biological electron microscopy: theory, techniques, and troubleshooting*. Plenum Press.
- Ettinger, A. and Wittmann, T.** (2014) ‘Fluorescence live cell imaging.’, *Methods in cell biology*, 123, pp. 77–94.
- Faoro, R. et al.** (2018) ‘Aberration-corrected cryoimmersion light microscopy’, *Proceedings of the National Academy of Sciences*, 115(6), pp. 1204–1209.
- Fuest, M. et al.** (2017) ‘Fabrication Advances for Microfluidic Cryofixation’, in *Mikrosystemtechnik Kongress*.
- Fuest, M. et al.** (2018) ‘Cryofixation during live-imaging enables millisecond time-correlated light and electron microscopy’, *Journal of Microscopy*.
- Fuller, B. J.** (2004) ‘Cryoprotectants: The essential antifreezes to protect life in the frozen state’, *Cryo-Letters*, 25(6), pp. 375–388.
- Giepmans, B. N. G. et al.** (2006) ‘The fluorescent toolbox for assessing protein location and function’, *Science*, 312(5771), pp. 217–224.
- Giske, A.** (2007) *CryoSTED microscopy A new spectroscopic approach for improving the resolution of STED microscopy using low temperature*. University of Heidelberg.
- Le Gros, M. A. et al.** (2009) ‘High-aperture cryogenic light microscopy’, *Journal of Microscopy*, 235(1), pp. 1–8.
- Gustafsson, M. G. L.** (2000) ‘Surpassing the lateral resolution limit by a factor of two using structured illumination microscopy’, *Journal of Microscopy*, 198(2), pp. 82–87.
- Hale, G. M. and Querry, M. R.** (1973) ‘Optical Constants of Water in the 200-nm to 200- μ m Wavelength Region’, *Applied Optics*. Optical Society of America, 12(3), p. 555.
- Hall, D. H., Hartweg, E. and Nguyen, K. C. Q.** (2012) ‘Modern Electron Microscopy Methods for *C. elegans*’, in *Methods in Cell Biology*, pp. 93–149.
- van Harrevelde, A. and Crowell, J.** (1964) ‘Electron microscopy after rapid freezing on a metal surface and substitution fixation’, *The Anatomical Record*, 149(3), pp. 381–385.
- Hell, S. W. and Wichmann, J.** (1994) ‘Stimulated-Emission-Depletion Fluorescence Microscopy’, *Optics Letters*, 19(11), pp. 780–782.
- Hillyer, M. B. and Gibb, B. C.** (2016) ‘Molecular Shape and the Hydrophobic Effect’, *Annual Review of Physical Chemistry*. NIH Public Access, 67(1), pp. 307–329.
- ImageJ.net** (2017) *ImageJ Webpage*. Available at: <https://imagej.net/Deconvolution> (Accessed: 22 April 2017).
- Kaufmann, R. et al.** (2014) ‘Super-resolution microscopy using standard fluorescent proteins in intact cells under cryo-conditions’, *Nano Letters*, 14(7), pp. 4171–4175.
- Kaufmann, R., Hagen, C. and Grünewald, K.** (2014) ‘Fluorescence cryo-microscopy: Current challenges and prospects’, *Current Opinion in Chemical Biology*, 20(1), pp. 86–91.

- Kellenberger, E. et al.** (1992) ‘Artefacts and morphological changes during chemical fixation’, *Journal of Microscopy*, 168(2), pp. 181–201.
- Kimata, T. et al.** (2012) ‘Thermotaxis of *C. elegans* as a model for temperature perception, neural information processing and neural plasticity’, *Worm*, 1(1), pp. 31–41.
- Kizilyaprak, C. et al.** (2014) ‘FIB-SEM tomography in biology’, *Methods in Molecular Biology*, 1117, pp. 541–558.
- Kleiman, M., Ryu, K. A. and Esser-Kahn, A. P.** (2016) ‘Determination of Factors Influencing the Wet Etching of Polydimethylsiloxane Using Tetra-n-butylammonium Fluoride’, *Macromolecular Chemistry and Physics*, 217(2), pp. 284–291.
- Kristoffersen, A. S. et al.** (2014) ‘Testing fluorescence lifetime standards using two-photon excitation and time-domain instrumentation: Rhodamine B, coumarin 6 and lucifer yellow’, *Journal of Fluorescence*. Springer, 24(4), pp. 1015–1024.
- Limmer, D. T. and Chandler, D.** (2014) ‘Theory of amorphous ices’, *Proceedings of the National Academy of Sciences*, 111(26).
- Masip, M. E. et al.** (2016) ‘Reversible cryo-arrest for imaging molecules in living cells at high spatial resolution’, *Nature Methods*, 13(8), pp. 665–672.
- McDonald, K. L.** (2009) ‘A review of high-pressure freezing preparation techniques for correlative light and electron microscopy of the same cells and tissues’, *Journal of Microscopy*, 235(3), pp. 273–281.
- Mejia, Y. X. et al.** (2014) ‘Microfluidic cryofixation for correlative microscopy’, *Lab Chip*, 14(17), pp. 3281–3284.
- Metzger, M. et al.** (2016) ‘Resolution enhancement for low-temperature scanning microscopy by cryo-immersion’, *Optics Express*, 24(12), p. 13023.
- Mishima, O. and Stanley, H. E.** (1998) ‘The relationship between liquid, supercooled and glassy water’, *Nature*, 396(6709), pp. 329–335.
- Möbius, W.** (2009) ‘Cryopreparation of biological specimens for immunoelectron microscopy’, *Annals of Anatomy*, 191(3), pp. 231–247.
- Moerner, W. E. and Orrit, M.** (1999) ‘Illuminating single molecules in condensed matter’, *Science*, 283(5408), pp. 1670–6.
- Müller, M., Meister, N. and Moor, H.** (1980) ‘Freezing In A Propane Jet And Its Application In Freeze-Fracturing’, *Mikroskopie*, 36(5–6), pp. 129–140.
- Nahmani, M. et al.** (2017) ‘High-numerical-aperture cryogenic light microscopy for increased precision of superresolution reconstructions’, *Proceedings of the National Academy of Sciences*, 114(15), pp. 3832–3836.
- Passmore, L. A. and Russo, C. J.** (2016) ‘Specimen Preparation for High-Resolution Cryo-EM’, in *Methods in Enzymology*, pp. 51–86.
- Plitzko, J. M., Rigort, A. and Leis, A.** (2009) ‘Correlative cryo-light microscopy and cryo-electron tomography: from cellular territories to molecular landscapes’, *Current Opinion in Biotechnology*, 20(1), pp. 83–89.
- Preibisch, S., Saalfeld, S. and Tomancak, P.** (2009) ‘Globally optimal stitching of tiled 3D microscopic image acquisitions’, *Bioinformatics*, 25(11), pp. 1463–1465.
- Ray F. Egerton** (2005) *Physical Principles of Electron Microscopy*. Springer Science+Business Media.
- Renaud, J. P. et al.** (2018) ‘Cryo-EM in drug discovery: Achievements, limitations and prospects’, *Nature Reviews Drug Discovery*. Nature Publishing Group, 17(7), pp. 471–492.
- Ross, D., Gaitan, M. and Locascio, L. E.** (2001) ‘Temperature Measurement in Microfluidic Systems Using a Temperature-Dependent Fluorescent Dye’, *Analytical Chemistry*, 73(17), pp. 4117–4123.
- Rumble, J.** (2018) *CRC Handbook of Chemistry and Physics*. 98th edn.
- Schermelleh, L., Heintzmann, R. and Leonhardt, H.** (2010) ‘A guide to super-resolution fluorescence microscopy’, *Journal of Cell Biology*, 190(2), pp. 165–175.
- Schertel, A. et al.** (2013) ‘Cryo FIB-SEM: Volume imaging of cellular ultrastructure in native

- frozen specimens', *Journal of Structural Biology*, 184(2), pp. 355–360.
- Schindelin, J. et al.** (2012) 'Fiji: An open-source platform for biological-image analysis', *Nature Methods*, 9(7), pp. 676–682.
- Schwarz, J., Lewandrowski, I. and Bringmann, H.** (2011) 'Reduced activity of a sensory neuron during a sleep-like state in *Caenorhabditis elegans*', *Current Biology*, 21(24), pp. R983–4.
- Schwarz, J., Spies, J.-P. and Bringmann, H.** (2012) 'Reduced muscle contraction and a relaxed posture during sleep-like Lethargus', *Worm*, 1(1), pp. 59–70.
- Shatilovich, A. V. et al.** (2018) 'Viable Nematodes from Late Pleistocene Permafrost of the Kolyma River Lowland', *Doklady Biological Sciences*, 480(1), pp. 100–102.
- Soleilhac, A. et al.** (2016) 'Temperature Response of Rhodamine B-Doped Latex Particles. From Solution to Single Particles', *Langmuir*, 32(16), pp. 4052–4058.
- Steinbrecht, R. A. and Zierold, K.** (1987) *Cryotechniques in Biological Electron Microscopy*. Edited by R. A. Steinbrecht and K. Zierold. Springer.
- Stephens, D. J. and Allan, V. J.** (2003) 'Light Microscopy Techniques for Live Cell Imaging', *Biological Imaging*, 82(2003), pp. 82–86.
- Thevenaz, P., Ruttimann, U. E. and Unser, M.** (1998) 'A pyramidal approach to subpixel registration based on intensity', *IEEE Transactions on Image Processing*, 7(1), pp. 27–41.
- Van Thor, J. J.** (2009) 'Photoreactions and dynamics of the green fluorescent protein', *Chemical Society Reviews*, 38(10), pp. 2935–2950.
- Tian, L. et al.** (2009) 'Imaging neural activity in worms, flies and mice with improved GCaMP calcium indicators', *Nature Methods*, 6(12), pp. 875–881.
- Van Venetië, R. et al.** (1980) 'Size determination of sonicated vesicles by freeze-fracture electron microscopy, using the spray-freezing method', *Journal of Microscopy*, 118(4), pp. 401–408.
- Venkatachalam, V. et al.** (2016) 'Pan-neuronal imaging in roaming *Caenorhabditis elegans*', *Proceedings of the National Academy of Sciences*, 113(8), pp. E1082–E1088.
- Verkade, P.** (2008) 'Moving EM: The Rapid Transfer System as a new tool for correlative light and electron microscopy and high throughput for high-pressure freezing', *Journal of Microscopy*, 230(2), pp. 317–328.
- Wang, Q. et al.** (2008) 'Structural Basis for Calcium Sensing by GCaMP2', *Structure*, 16(12), pp. 1817–1827.
- Warkentin, M., Sethna, J. P. and Thorne, R. E.** (2013) 'Critical Droplet Theory Explains the Glass Formability of Aqueous Solutions', *Physical Review Letters*, 110(1), p. 015703.
- Warren, S. G.** (1984) 'Optical constants of ice from the ultraviolet to the microwave', *Applied Optics*, 23(8), p. 1206.
- Watanabe, S., Liu, Q., et al.** (2013) 'Ultrafast endocytosis at *Caenorhabditis elegans* neuromuscular junctions', *eLife*, 2013(2), pp. 1–24.
- Watanabe, S., Rost, B. R., et al.** (2013) 'Ultrafast endocytosis at mouse hippocampal synapses.', *Nature*, 504(7479), pp. 242–7.
- Whitesides, G. M.** (2006) 'The origins and the future of microfluidics', *Nature*, 442(7101), pp. 368–373.
- Wikimedia Commons** (2013) *Electron interaction with matter*. Available at: https://commons.wikimedia.org/wiki/File:Electron_Interaction_with_Matter.svg (Accessed: 17 August 2018).
- Willig, K. I. et al.** (2006) 'Nanoscale resolution in GFP-based microscopy', *Nature Methods*, 3(9), pp. 721–723.
- Wittenburg, N. and Baumeister, R.** (1999) 'Thermal avoidance in *Caenorhabditis elegans*: An approach to the study of nociception', *Proceedings of the National Academy of Sciences*, 96(18), pp. 10477–10482.
- Wolff, G. et al.** (2016) 'Towards correlative super-resolution fluorescence and electron cryo-microscopy', *Biology of the Cell*, 108(9), pp. 245–258.
- Xi, E. et al.** (2017) 'Hydrophobicity of proteins and nanostructured solutes is governed by

topographical and chemical context', *Proceedings of the National Academy of Sciences*, 114(51), p. 201700092.

Yeh, Y. and Feeney, R. E. (1996) 'Antifreeze Proteins: Structures and Mechanisms of Function.', *Chemical reviews*, 96(2), pp. 601–618.

Yeung, E. C. and Huang, Q. B. (2015) 'Chemical and Physical Fixation of Cells and Tissues: An Overview', in *Plant Microtechniques and Protocols*, pp. 1–572.

Appendix

Appendix I: Brief summary of experimental parameters

Table 10 Experimental parameters used in each experiment

	Sample	Cryo-protectant	Detector	Objective	Light source	Exp. Time	Filter set
Traps	WT <i>C. elegans</i>	/	EMCCD	20x 0.4 NA	White LED	5 ms	/
RhB intensity vs. Temp.	RhB 1% in DI water	/	CMOS	10x 0.2 NA	405 nm LED	500 ms	Zeiss 75 HE
Temperature gradients	1 μ m RhB beads	/	CMOS	20x 0.4 NA	White LED	500 ms	RhB filter
<i>In situ</i> cryofixation	WT <i>C. elegans</i>	10% sucrose	CMOS	10x 0.2 NA	Mercury lamp	34 ms	/
	GCaMP <i>C. elegans</i>	10% trehalose	CMOS	20x 0.4 NA	Mercury lamp	100 ms	GFP filter
Fast/slow freezing image quality comparison	GCaMP <i>C. elegans</i>	10% trehalose	CMOS	20x 0.4 NA	Mercury lamp	300 ms	GFP filter
	WT <i>C. elegans</i>	10% trehalose	CMOS	20x 0.4 NA	Mercury lamp	300 ms	/
100 fps cryofixation	WT <i>C. elegans</i>	10% sucrose	CMOS	10x 0.2 NA	Halogen lamp	10 ms	DIC
Workflow	WT <i>C. elegans</i>	10% glycerol	CMOS (DSLR)	10x 0.2 NA	White LED	/	/
Cryo-check	GCaMP <i>C. elegans</i>	10% trehalose	CMOS (smartphone)	10x 0.2 NA	Mercury lamp	/	Zeiss 38 HE
Cryo-immersion	GCaMP <i>C. elegans</i>	10% trehalose	APD	63x 1.15 NA	Laser	10-50 μ s/px	STED. 1-2

Table 11 Filter sets used in this work

Filter set	Excitation Filter (nm)	Dichroic mirror (nm)	Emission Filter (nm)
GFP	480/40	>510	>510
RhB	546/10	>575	>580
STEDYCON 1	445/10 (laser)	/	502-572 + 608-627
STEDYCON 2	640	/	650-700 nm
Zeiss 75 HE	410/39 + 537/25	439 + 555	482/59 + 610/96
Zeiss 38 HE	470/40	495	525/50

Giovanni Marco Nocera – Curriculum Vitae

Ph. D. Candidate

29 years old

Italian nationality

PERSONAL SUMMARY

- Chemist with a multi-disciplinary background in material and life sciences
- Comprehensive understanding of bottom-up and top-down manufacturing approaches
- Experienced in design and development of fabrication and measurement procedures for scaled-down systems
- Hands-on experience in cleanroom fabrication techniques
- Good decision maker, curious and passionate on the job

EDUCATION

- **Ph. D. Candidate in Physics**
Max Planck Institute for Biophysical Chemistry (Göttingen, Germany)
October 2014 – October 2018
- **M.S. in Material chemistry and physical-chemistry**
Université Pierre et Marie Curie, Paris (France)
September 2012 – September 2014
- **B.S. in Chemistry**
Università degli Studi di Napoli “Federico II”, Naples (Italy)
September 2007 – October 2011

FURTHER PROFESSIONAL EXPERIENCE

- 2014-2018, **Ph. D. Project** (4 years)
Max Planck Institute for Biophysical Chemistry in Göttingen, Germany
- 2014, **2nd Year Master’s Internship** (8 months)
Max Planck Institute for Biophysical Chemistry in Göttingen, Germany
- 2013, **1st Year Master’s Internship** (4 months)
École Normale Supérieure of Paris, Chemistry Department
- 2012, **Environmental Sampling Technician** (5 months)
Laboratoire Yktinef (Paris)
- 2011, **Bachelor’s Thesis Internship** (4 months)
Università degli Studi di Napoli “Federico II”, Chemistry Department

LANGUAGE SKILLS

Italian Native speaker
French Fluent

Neapolitan Native speaker

English Fluent
German Beginner

PEER REVIEWED PUBLICATIONS & CONFERENCE PRESENTATIONS

1. M. Fuest*, **G.M. Nocera***, M.M. Modena, D. Riedel, T.P. Burg. *Cryofixation during live-imaging enables millisecond time-correlated light and electron microscopy*, **Journal of Microscopy**, 2018
2. M. Fuest, **G.M. Nocera**, M. M. Modena, T.P. Burg. *Fabrication Advances for Microfluidic Cryofixation*. Mikrosystem Technik Kongress 2017, Munich, Germany
3. M. Fuest, **G.M. Nocera**, M.M. Modena, D. Riedel, T.P. Burg. *Advances in microfluidic cryofixation for correlative light and electron microscopy*, **Invited talk**, Microscopy Conference 2017, Lausanne, Switzerland
4. **G.M. Nocera**, M. Fuest, Y. Meija, M.M. Modena, T.P. Burg. *Method development of an in situ rapid freezing device for light and electron cryo-microscopy of C. elegans*, **Poster session**, Microfluidics 2016, Heidelberg, Germany
5. **G.M. Nocera**, K. Ben M'Barek, D.G. Bazzoli, G. Fraux, M. Bontems-Van Heijenoort, J. Chokki, S. Georgeault, Y. Chen, J. Fattaccioli. *Fluorescent microparticles fabrication through chemical coating of O/W emulsion droplets with a thin metallic film*, **RSC Advances**, 2014, 4 (23), 11564 – 11568